The Dissertation Committee for Guru Bahadur Singh Khalsa
certifies that this is the approved version of the following dissertation:

Theory of d_0 perovskites and their heterostructures

Committee:

Allan H. MacDonald, Supervisor

Alex Demkov

Gregory A. Fiete

Jianshi Zhou

Keji Lai

Theory of d_0 perovskites and their heterostructures

by

Guru Bahadur Singh Khalsa, B.S.

DISSERTATION

Presented to the Faculty of the Graduate School of

The University of Texas at Austin

in Partial Fulfillment

of the Requirements

for the Degree of

DOCTOR OF PHILOSOPHY

THE UNIVERSITY OF TEXAS AT AUSTIN

August 2013

For my family.

Acknowledgments

First and foremost, I would like to express gratitude to my advisor Allan MacDonald, whose patience and support has been unwavering. His constant encouragement and enjoyment for learning has greatly contributed to success in my graduate studies. I would like to thank Dr. David Dunlap of the University of New Mexico - without whom I would have never had an interest in physics. Also, Byounghak Lee of Texas State University who guided me through the world of first principles calculations.

I would also like to thank my experimental collaborators: Susanne Stemmer, S. James Allen, Bharat Jalan, Young Jun Chang, and Eli Rotenberg, who have all contributed significantly to my understanding of experimental physics and material science. In that regard, I would also like to thank John Singleton and Insun Jo who were always available with advice on understanding experimental details.

My gratitude also goes to my group members: Rafi Bistritzer, Ion Garate, Jeil Jung, Maria Moura, Tami Pereg-Barnea, Wei-Cheng Lee, Dagim Tilahun, Fan Zhang, Yafis Barlas, Inti Sodemann, Rohit Hegde, Ming Xie, Hua Chen, Chao Lei. Their many talents have always helped and inspired me. A special thanks to Becky Drake and Annie Harding without whom administrative requirements would have surely been less fun and too cumbersome.

I would also like to thank Kathleen McDonald who has always brought fun and balance into my life. Finally, I wish to thank my family for the support and guidance they have shown me in all of my many pursuits.

Guru Bahadur Singh Khalsa

The University of Texas at Austin

August 2013

Theory of d_0 perovskites and their heterostructures

Publication No. _____

Guru Bahadur Singh Khalsa, Ph.D.
The University of Texas at Austin, 2013

Supervisor: Allan H. MacDonald

The recent discovery of a two-dimensional electron (2DEG) gas at interfaces between nonpolar $SrTiO_3$ (STO) with other polar perovskites has lead to an enormous amount of research. Among this 2DEGs most interesting properties are two-dimensional superconductivity and ferromagnetism, sometimes concurrent. This study provides a starting point in understanding the reconstruction of bulk perovskite t_{2g} bands near a surface or polar interface. First a symmetry constrained $\vec{k} \cdot \vec{p}$ model is developed for an arbitrary pseudocubic bulk perovskite. This $\vec{k} \cdot \vec{p}$ model is applied to studies of bulk STO under external strain and to the Shubnikov - de Haas effect in lightly doped STO to high magnetic fields. Then a simplified electronic structure model is developed for surfaces and interfaces. This model includes non-linear and non-local screening effects by a single polar lattice mode. Generalization of the lattice screening model is discussed. Bonding within a single perovskite layer is then investigated further to understand Rashba interactions and their connection with microscopic material parameters. Next the optical conductivity of quantum confined t_{2g}

bands is investigated. Finally some possible future work based on the ideas developed in this thesis are explained.

Table of Contents

List of Tables

List of Figures

Chapter 1

Introduction

1.1 Introduction

The perovskite crystal structure supports most of the periodic table and hosts a variety of appealing material characteristics in the bulk, including ferroelectricity, magnetism, and superconductivity[1]. High quality perovskite oxides can be grown epitaxially, using molecular beam epitaxy or pulsed laser deposition to achieve artificially tailored heterostructures[2, 3]. Moreover, it has been shown that epitaxial growth of the perovskite lattice can be achieved on silicon - a necessary condition for integration with current technologies[4, 5]. These considerations have motivated strong interest in perovskite surfaces and interfaces[6]. Correspondingly, the scientific community has dedicated countless hours to the study of perovskites.

While the materials study of perovskites would truly begin with Goldschmidt's pioneering study[7] in the beginning of the 20th century, the discovery of the first perovskite is attributed to Gustov Rose in 1839. While surveying the Ural mountains, Rose found a previously undiscovered mineral - later determined to be $CaTiO_3$. He named this mineral "Perovskite" after the head of the mineralogical society at the time Count Lev Perovski. Crystals that share the ABX_3 chemical formula and Perovskite bulk structure (Fig. 1.1a) are called perovskites. In the perovskite lattice the A and

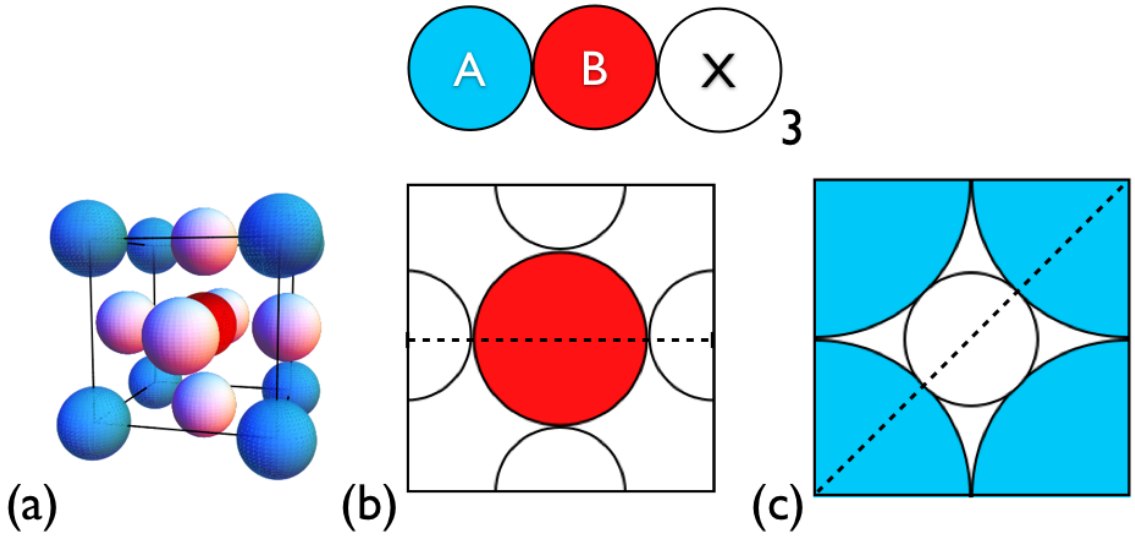

Figure 1.1: Pseudocubic unit cell of the perovskite lattice.

B atoms are cations and the X atom is typically oxygen (this case is the focus of this thesis). The bulk perovskite crystal structure was first identified in an early X-ray diffraction experiment by V. M. Goldschmidt in 1926[7]. In this study Goldschmidt surveyed materials and found that a simple rule for the stability of the perovskite lattice could be established based on a closed packing argument. By imagining spheres with the ionic radius of the corresponding atom and assuming that the closed packed cubic structure is the most stable, he related the A, B, and O atoms radii with the cubic lattice constant. From Fig. 1.1 (b,c) we can see that the lattice constant a is related to the ionic radii though, $a = \sqrt{2}(r_A + r_O)$ and $a = 2(r_B + r_O)$. The ratio of these two,

$$t = \frac{r_A + t_O}{\sqrt{2}(r_B + r_O)} \tag{1.1}$$

is now termed the "Goldschmidt tolerance factor" or simply the "tolerance factor". Goldschmidt found that for a tolerance factor near 1 the cubic structure is stable[7]. The tolerance factor is still used in the perovskite literature to describe physical properties. If the tolerance factor is greater than 1, the B atom has space and can distort from the center of the cell leading to a ferroelectric transition. If the tolerance factor is less than 1, the A atom has space to move, typically resulting in rotations of the octahedral oxygen environment[8, 9]. The tolerance factor has proved to be a useful rule of thumb in understanding the relation between the underlying perovskite structure and bulk physical properties and has been mostly unchanged since Goldschmidt's original study. (A more sophisticated technique where the bond-length is used in a semi-empirical form has also been used with good results[10].)

In the United States the need for new capacitor technology during World War 2, spurred further interest in perovskites. The most notable and first recognized perovskite ferroelectric, $BaTiO_3$ ($t = 1.07$) was discovered during this time and used to replace existing capacitor technology based on mica[11]. Like $BaTiO_3$, perhaps the most well studied perovskite, $SrTiO_3$, was discovered in the lab. The National Lead Co. in the United States - dedicated mainly to making paint - patented an "Optically Glass-Like Material" that was made from large single crystal $SrTiO_3$ processed from solution. This material has been the focus of an enormous amount of research (Fig. 1.2). Fig. 1.2 shows the number of publications and patents sought since 1965 with the keyword "SrTiO3"[12, 13]. In 1965, where the graph begins, it was found that lightly doped $SrTiO_3$ not only became conducting, but became superconducting at low temperatures[14]. In the early 1990s, shortly after the discovery of high temperature

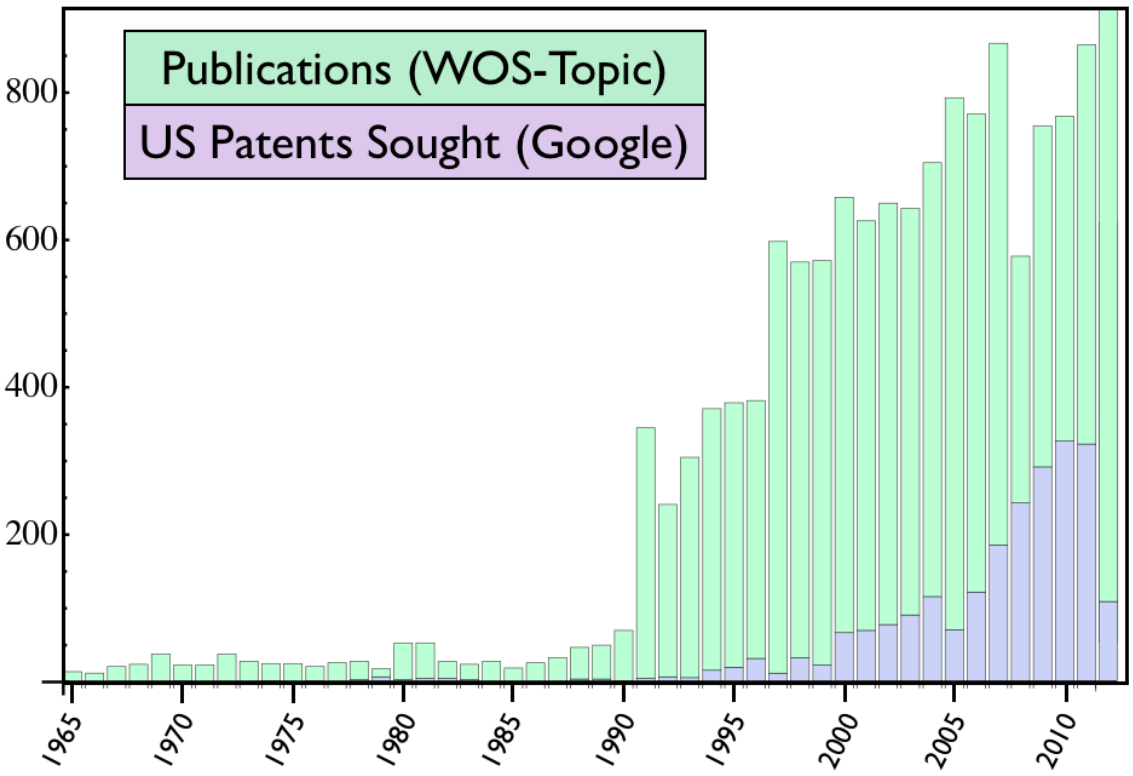

Figure 1.2: Publications (green) and U.S. patents sought (purple) vs. year with the keyword "$SrTiO_3$". In 2012 there were 1018 publications. A similar graph including all perovskites would be too cumbersome.

superconductivity in the closely related cuprate ceramics[15], $SrTiO_3$ began to be used as a substrate for epitaxial growth. Since then there has been a steady increase in the scientific interest in $SrTiO_3$. Surprisingly, $SrTiO_3$ was not discovered in the natural world until 1982 and remains extremely rare[16].

The most recent catalyst for perovskite research was the discovery of a two-dimensional electron gas (2DEG) at the interface of two insulating perovskites, $SrTiO_3$ and $LaAlO_3$ by Ohtomo and Hwang in 2004[17]. This finding of a high-mobility 2DEG

was initially thought to be closely tied to the polar nature of the band insulator, $LaAlO_3$. It has since been found in a variety of $SrTiO_3$ based systems. For example, a 2DEG residing in the $SrTiO_3$ can be formed also at its interface with a Mott insulator[3, 18, 19], in δ - doped configurations[20–23], in vacuum cleaved samples[24, 25], and even by electrostatic gating [26–28]. $KTaO_3$, a strong spin-orbit coupling cousin to $SrTiO_3$ has also been the focus of similar experimental attention[24, 29]. Both materials show high mobility 2DEGs and 2D superconductivity[26, 29, 30] while the heterostructures of $SrTiO_3$ have the addition experimental feature of ferromagnetism[31–35] - sometimes concurrently with superconductivity[31, 32, 34, 35].

The focus of this thesis is the quantitative modeling of these confined electronic states. It will be shown that features of the confined electronic structure are at odds with wisdom gained from conventional semiconductor heterostructures. In particular, the confinement electric field is screened predominantly by polar lattice distortions[36] which can be sensitive to the details of the interface on short length scales. These lattice distortions qualitatively change the confinement potential[36, 37] and at the same time, lead to Rashba interactions[38]. It is hoped that this work provides a starting point for predictive, quantitative models of confined electronic states at perovskite surfaces/heterointerfaces - an area of research that is expected to continue to gain momentum in the coming years.

1.1.1 $SrTiO_3$

Because it is the d^0 system most studied in recent experimental and theoretical work (See Fig. 1.2), all chapters are connected to $SrTiO_3$ in some way. The lessons

learned can easily be generalized to other d^0 systems which are explicitly discussed where most relevant. Below we provide a brief general discussion of bulk $SrTiO_3$ properties. A more focussed discussion of relevant properties are included in the individual chapters.

Bulk $SrTiO_3$ is a non-polar pseudocubic band insulator with an indirect energy gap of 3.2 eV separating its oxygen p-orbital dominated valance band, from its Ti t_{2g}-orbital dominated conduction band. By chemical substitution of the Ti (for Nb) or the Sr atoms (for La) or by introducing oxygen vacancies it is possible to electron dope the system with a high level of precision. The Ti atom d-orbitals are split by the octahedral oxygen environment pushing the Ti e_g bands up in energy by $\sim$ 2 eV[39–41] relative to the t_{2g} bands.

The conduction band of bulk $SrTiO_3$ has been the subject of experimental and theoretical attention for about 50 years[39, 42–46]. While early models featured a conduction band edge similar to Si with valleys near the X-point, subsequent experiments[47] and modeling placed the conduction band minimum at Γ, the zone center. Uwe et al. [48, 49] used the Shubnikov-de Haas effect and Raman scattering to determine the spin-orbit interaction strength and sign, the band edge splitting caused by the low temperature tetragonal distortion, and details of the Fermi surface. Uwe et al. found that the bulk t_{2g} bands are split at the Γ point, in the first place by spin-orbit interactions which push one time-reversed pair of t_{2g} bands up by $\sim$ 18 meV relative to the other two pairs. The two lower energy bands are further split below 105-110 K by an antiferrodistortive structural transition to a tetragonal phase. Below the critical temperature neighboring TiO_6 octahedras continuously rotate in

opposite directions by an angle of up to a few degrees. Recent studies have called into question the strength of the SO splitting[50] and both the strength and sign of the tetragonal distortion[51]. Addressing this issue is the focus of Chapters 2 and 4.

$SrTiO_3$ is also well known for its large low temperature dielectric response[52]. For weak electric fields along the (001) crystal axis its dielectric constant can be as large as ~ 26000 with similar values along (110) and (111)[52]. This is due primarily to a soft polar phonon mode, common to many perovskites[53, 54]. In $SrTiO_3$ this mode is associated with opposite displacements of the Ti atom and the octahedral oxygen environment - although the Sr atom has some displacement as well. As the electric field is increased the displacement of the soft polar mode is quickly suppressed by the anharmonic crystal potential seen by the Sr and Ti atoms[52].

1.2 Organization of Thesis

This section outlines the organization of the work contained within this thesis.

Chapter 2 develops a symmetry constrained $\vec{k} \cdot \vec{p}$ model of d_0 bulk perovskites. This model is applied to experimental measures of bulk bandstructure. In particular, angle resolved photoemission (ARPES) and the Shubnikov - de Haas effect (SdH) are explored. A matrix element effect in ARPES is connected to experimental geometry and orbital band character. This chapter is based on work performed in collaboration with Rafi Bistritzer and published in Ref. [50].

Chapter 3 describes a study that uses the matrix elements developed in Chapter 2 to measure changes in the bulk electronic structure due to strain. The idea for

this work came from a lunch meeting I had with Young Jun Chang at the APS March Meeting in 2011. The experiment was conducted by Young Jun Chang, Eli Rotenberg, and collaborators at Lawrence Berkeley National Lab Advanced Light Source Beam Line 7.0 later that year and represents the first experimental measure of the conduction band deformation potentials that we are aware of. Chapter 3 is based on Ref. [55].

Chapter 4 describes a SdH study of lightly doped bulk $SrTiO_3$ conducted by Jim Allen, Bharat Jalan, Susanne Stemmer, and collaborators with densities previously unobtainable by epitaxial growth. In this chapter, the $\vec{k} \cdot \vec{p}$ model of Chapter 2 is recast in terms of Luttinger parameters and fit to SdH oscillation frequency and temperature dependence to parameterize the low energy conduction band structure. This chapter is based on Ref. [56]. My role in this collaboration was in the interpretation of the low and high magnetic field results - the high field analysis has not been included in this thesis but will be published seperately.

Chapter 5 is based on the paper *"Theory of the $SrTiO_3$ surface state two-dimensional electron gas"* [36]. It extends the $\vec{k} \cdot \vec{p}$ model of Chapter 2 to a tight-binding model of the electronic structure but is primarily concerned with the novel lattice mediated dielectric response in perovskites and the relation of this effect to the confinement potential and 2D electronic states.

Chapter 6 takes a closer look at the effect of a confining electric field on bonding within the ABO_3 perovskite lattice to describe, on a general platform, Rashba interactions in t_{2g} perovskites. Chapter 6 is based on Ref. [38].

Chapter 7 investigates the optical conductivity of the t_{2g} surface state. This work was conducted in collaboration with Ming Xi at the University of Texas.

Chapter 8 summarizes the work within the thesis and suggests possible areas for future research into confined d^0 perovskite systems.

Chapter 2

Electronic structure of doped d^0 perovskite semiconductors

In this chapter we address the low-energy effective Hamiltonian of electron doped d^0 perovskite semiconductors in cubic and tetragonal phases using the $\boldsymbol{k} \cdot \boldsymbol{p}$ method. This Hamiltonian depends on the spin-orbit interaction strength, on the temperature-dependent tetragonal distortion, and on a set of effective-mass parameters whose number is determined by the symmetry of the crystal. We explain how these parameters can be extracted from angle resolved photo-emission, Raman spectroscopy, and magneto-transport measurements and estimate their values in $SrTiO_3$.

2.1 Introduction

Within the perovskite family, the d^0 materials have received particular attention, often because of their large band gaps. $SrTiO_3$, for example, is perhaps the most common substrate for the epitaxial growth of oxide materials. Recently there has been growing interest in the transport properties of lightly electron doped d^0 perovskites [57]. In $KTaO_3$, for example, strong spin-orbit (SO) coupling facilitates electrical manipulation of spin in a field effect transistor geometry [58]. The two-dimensional electron systems which form at interfaces between d^0 materials[17] show

intriguing magnetic phases[59] and peculiar magneto-transport features [60, 61]. Advanced epitaxial growth techniques enable δ-doping of oxides[22] and the fabrication of oxide heterostructures [62]. These relatively recent rapid advances could, it is hoped, eventually lead to useful oxide based nano-electronic devices [63].

The low-energy band structure of an oxide provides a starting point for understanding not only its bulk transport characteristics but also its electronic properties near δ-doped layers and near interfaces/surfaces. First principles electronic structure theory methods[39, 64–66] are usually efficient for determining the gross structure of a band. However these methods are not sufficiently accurate to nail down the fine features that determine the electronic properties of the states at the bottom of the conduction band that are important in weakly doped bulk materials, and in low-carrier-density two-dimensional electron systems. In particular, it appears that at present bulk band structures in d^0 perovskites are not known accurately enough to predict the two-dimensional bands produced by δ-doping[22] or localization at heterojunctions.

The $\boldsymbol{k} \cdot \boldsymbol{p}$ method[67, 68] offers an alternative and a potentially more accurate route for characterizing band structure near the conduction band minimum. The method provides an effective Hamiltonian that depends on a set of phenomenological parameters which can be small in number when band extrema occur at high-symmetry points in momentum space. The utility of this method hinges on the ability to extract accurate parameter values from experiments. In the case of perovskites the most valuable experimental probes appear at present to be angle resolved photo-emission (ARPES), Raman spectroscopy, and magneto-transport measurements.

Many of the most studied oxides have conduction-band minima located at the center of the Brillioun zone. We therefore apply the $\boldsymbol{k} \cdot \boldsymbol{p}$ method to obtain an effective low energy Hamiltonian near the Γ point. At high temperatures, perovskites typically have cubic symmetry. As the temperature is decreased the symmetry is usually lowered, most commonly to either orthorhombic or tetragonal. The distortion can be driven by the motion of atoms along one of the cubic axes (*e.g.* in $BaTiO_3$) or by a rotation of the oxygen octahedras (*e.g.* in $SrTiO_3$). Structural phase transitions can also be induced by applied stress [69].

In this chapter we focus on the cubic and tetragonal phases. In Section 2.2 we briefly describe the $\boldsymbol{k} \cdot \boldsymbol{p}$ method and then use it to derive the low energy effective theory of a d^0 perovskite in the vicinity of the Γ point. In Section 2.3 we elaborate on experimental methods for obtaining the parameters of the $\boldsymbol{k} \cdot \boldsymbol{p}$ Hamiltonian. Using the experimental data accumulated over the past few decades we then study the effective Hamiltonian of the conduction bands of $SrTiO_3$ in Section 2.4. We summarize in Section 2.5.

2.2 Low energy theory

For many perovskites of current interest such as $SrTiO_3$ the conduction band minima is at the Brillouin-zone center Γ-point. For momenta near the Γ-point the crystal field splits the ten d-bands into four high energy e_g bands, and six lower energy t_{2g} bands. Because the crystal field induced gap is typically a few eV's, it is sufficient to consider the t_{2g} bands when constructing a low energy theory of weakly-doped d^0 materials. In the cubic phase the t_{2g} bands are degenerate at the Γ-point

if spin-orbit interactions are neglected, but are weakly-split by typical tetragonal or orthorhombic distortions and by spin-orbit interactions. Unless the Fermi energy is large compared to these splittings, spin-orbit and distortion related band parameters must be accurately known in order to achieve a reasonable description of electronic properties.

2.2.1 Effective Hamiltonian

The unperturbed Hamiltonian in the $\boldsymbol{k}\cdot\boldsymbol{p}$ perturbation theory[67, 68] is

$$H_0 = \frac{p^2}{2m} + V(\boldsymbol{r}) + \frac{\hbar}{4m^2c^2}\left(\nabla V \times \boldsymbol{p}\right)\cdot\sigma. \tag{2.1}$$

H_0 consists of three terms: the kinetic energy term, the lattice potential term $V(\boldsymbol{r})$, and the spin-orbit term (σ is the Pauli matrix vector). The $\boldsymbol{k}\cdot\boldsymbol{p}$ Hamiltonian, which acts on the periodic part of the Bloch state, includes a second term which accounts for the dependence of band wavefunctions on Bloch wavevector $\boldsymbol{k}$:

$$H_{\boldsymbol{k}\cdot\boldsymbol{p}} = \frac{\boldsymbol{k}}{m}\cdot\left(\boldsymbol{p} + \frac{1}{4m^2c^2}\boldsymbol{\sigma}\times\nabla V\right) \equiv \frac{\boldsymbol{k}}{m}\cdot\boldsymbol{P}. \tag{2.2}$$

The $\boldsymbol{k}\cdot\boldsymbol{p}$ method exploits the high symmetry at the Γ point to classify the $\boldsymbol{k}=0$ wave functions by irreducible representations (irreps) of the appropriate point group symmetry. It then uses perturbation theory

$$h_{ij} = \delta_{ij}k^2 + \sum_{\alpha}\frac{\langle\psi_i|H_{\boldsymbol{k}\cdot\boldsymbol{p}}|\phi_\alpha\rangle\langle\phi_\alpha|H_{\boldsymbol{k}\cdot\boldsymbol{p}}|\psi_j\rangle}{E_i(0)-E_\alpha(0)} \tag{2.3}$$

to evaluate t_{2g} projected Hamiltonian corrections to second order in the Bloch wavevector $\boldsymbol{k}$. In this chapter, we use units in which $\hbar = 2m = 1$ where m is the bare mass

of the electron. The six t_{2g} band energies $\epsilon(\boldsymbol{k})$ then follow from the secular equation

$$\det[h_{\rm SO} + h_{\rm L} + h(\boldsymbol{k}) - \epsilon(\boldsymbol{k})I] = 0. \tag{2.4}$$

In Eq.(2.3) $\{|\psi_j\rangle\}$ label a basis set for the t_{2g} bands and ϕ_α is summed over bands outside the t_{2g} manifold. The first order term was omitted in Eq.(2.3) since it vanishes in a perovskite structure with inversion symmetry. The matrices $h_{\rm L}$ and $h_{\rm SO}$ account phenomenologically for tetragonal distortion and SO interactions at the Γ point and are discussed more explicitly below.

The wave functions at the zone center have no covalent character and can be spanned by the t_{2g} basis

$$\{X_\uparrow, Y_\uparrow, Z_\uparrow, X_\downarrow, Y_\downarrow, Z_\downarrow\}. \tag{2.5}$$

Here X, Y and Z correspond respectively to the $|yz\rangle, |xz\rangle$ and $|xy\rangle$ t_{2g} orbitals. Below we obtain the Hamiltonian matrix in this basis.

The lattice term $h_{\rm L}$ is non zero in the tetragonal phase. If we choose a convenient zero of energy and set the $\hat{\boldsymbol{z}}$ axis along the tetragonal axis then $h_{\rm L}$ has a single non-zero matrix element:

$$\langle Z\alpha|V|Z\alpha\rangle = \Delta_{\rm T}, \tag{2.6}$$

where α accounts for the spin. The SO term in the Hamiltonian is

$$(h_{\rm SO})_{i\alpha,k\beta} = \langle\xi_i\alpha|\Lambda\cdot\sigma|\xi_k\beta\rangle = \langle\xi_i|\Lambda_j|\xi_k\rangle\cdot\langle\alpha|\sigma_j|\beta\rangle, \tag{2.7}$$

where $\Lambda \propto \nabla V \times \boldsymbol{p}$ and ξ_i is one of the orbital basis functions. Because Λ transforms as a pseudovector, $\langle\xi_i|\Lambda_j|\xi_k\rangle \propto \epsilon_{ijk}$ where ϵ_{ijk} is the third rank antisymmetric tensor.

For example, $\langle X|\Lambda_z|X\rangle$ and $\langle X|\Lambda_z|Z\rangle$ vanish under reflection about the x-z plane. Furthermore, since the matrix elements (2.7) must be imaginary

$$\langle \xi_i|\Lambda_j|\xi_k\rangle = -i\frac{\Delta_{\rm SO}}{3}\epsilon_{ijk}. \tag{2.8}$$

Strictly speaking, SO coupling is described by two parameters in the tetragonal phase. However we neglect this small correction since it is of order of $\Delta_{\rm T}$ over the band gap compared to the spin-orbit coupling term we retain.

The $\boldsymbol{k}$-dependent part of the Hamiltonian h is obtained using Eq.(2.3). We show in the Appendix A that

$$h = \begin{pmatrix} h_\uparrow & 0 \\ 0 & h_\downarrow \end{pmatrix} \tag{2.9}$$

with

$$h_\alpha = \begin{pmatrix} \mathcal{L}_5 k_x^2 + \mathcal{M}_5^{\parallel} k_y^2 + \mathcal{M}_5^{\perp} k_z^2 & \mathcal{N}_5 k_x k_y & \mathcal{N}_{45}^{\star} k_x k_z \\ \mathcal{N}_5 k_x k_y & \mathcal{L}_5 k_y^2 + \mathcal{M}_5^{\parallel} k_x^2 + \mathcal{M}_5^{\perp} k_z^2 & \mathcal{N}_{45}^{\star} k_y k_z \\ \mathcal{N}_{45} k_x k_z & \mathcal{N}_{45} k_y k_z & \mathcal{M}_4(k_x^2 + k_y^2) + \mathcal{L}_4 k_z^2 \end{pmatrix} |\alpha\rangle. \tag{2.10}$$

In the tetragonal phase the h matrix depends on eight real parameters (only $\mathcal{N}_{45}$ may be complex). In the cubic phase parameter values become independent of their subscript labels (*e.g.* $\mathcal{L}_4 = \mathcal{L}_5 \to L$) and h then depends on only three parameters. The energy dispersion relations follow from Eqs.(2.4,2.6—2.10). Because the Hamiltonian is time-reversal invariant and has inversion symmetry it gives rise to three doubly-degenerate bands.

In the next section we discuss zone-center wave functions and energies. The wavefunctions play a crucial role in matrix-element considerations which powerfully expand the ability of ARPES experiments to determine the parameters of the $\boldsymbol{k}\cdot\boldsymbol{p}$-Hamiltonian. The zone-center energies can be compared with t_{2g} band-splitting values obtained by Raman spectroscopy.

2.2.2 Zone center energies and wave-functions

The Hamiltonian at the zone center is $h_{\rm L} + h_{\rm SO}$. The energies are therefore

$$\begin{aligned} \epsilon_6 &= 0 \\ \epsilon_7^{(a)} &= \frac{\Delta_{\rm SO}}{2} + \frac{\Delta_{\rm T}}{2} - \frac{Q}{3} \\ \epsilon_7^{(b)} &= \frac{\Delta_{\rm SO}}{2} + \frac{\Delta_{\rm T}}{2} + \frac{Q}{3}, \end{aligned} \tag{2.11}$$

where

$$Q = \frac{3}{2}\sqrt{\Delta_{\rm SO}^2 - \frac{2}{3}\Delta_{\rm SO}\Delta_{\rm T} + \Delta_{\rm T}^2}. \tag{2.12}$$

(Energy has been shifted so that ϵ_6 will vanish.) In the cubic phase the t_{2g} bands transform as Γ_{25}^+ in the absence of spin-orbit coupling. SO interactions split the bands to $\Gamma_7^+ + \Gamma_8^+$. When there is a tetragonal transition, the four-fold degenerate Γ_8 states further split to $\Gamma_7 + \Gamma_6$. The notation in Eqs.(2.11) correspond to these latter irreps.

The (unnormalized) wave functions corresponding to the energies (2.11) are

$$\begin{aligned} \psi_1^6 &= X_\downarrow - iY_\downarrow \\ \psi_2^6 &= X_\uparrow + iY_\uparrow \\ \psi_1^{7a} &= (Q+D)X_\uparrow - i(Q+D)Y_\uparrow + 2\Delta_{\rm SO}Z_\downarrow \\ \psi_2^{7a} &= \Delta_{\rm SO}X_\downarrow + i\Delta_{\rm SO}Y_\downarrow - (Q-D)Z_\uparrow \\ \psi_1^{7b} &= (Q-D)X_\uparrow - i(Q-D)Y_\uparrow - 2\Delta_{\rm SO}Z_\downarrow \\ \psi_2^{7b} &= \Delta_{\rm SO}X_\downarrow + i\Delta_{\rm SO}Y_\downarrow + (Q+D)Z_\uparrow \end{aligned} \tag{2.13}$$

where

$$D = 3\Delta_{\rm T}/2 - \Delta_{\rm SO}/2. \tag{2.14}$$

It is interesting to follow the evolution of the bands as the ratio between $\Delta_{\rm T}$ and $\Delta_{\rm SO}$ is varied from zero to infinity. The two limits are given in Table 2.1. In the cubic phase the states $\{\psi^6, \psi^{7a}\}$ are degenerate and are spilt off from the $\{\psi^{7b}\}$ states by an energy of $\Delta_{\rm SO}$. In the tetragonal phase when $|\Delta_{\rm SO}| > |\Delta_{\rm T}|$ the states group to the three doubly degenerate pairs ψ^6, ψ^{7a} and ψ^{7b}. As the temperature is lowered the four ψ^7 states mix. If eventually $|\Delta_{\rm SO}| \ll |\Delta_{\rm T}|$ then the ψ_1^{7a} and ψ_1^{7b} states combine to give the $Z_\downarrow$ state which is purely tetragonal in character. This effect will be important

$\Delta_{\mathrm{T}} = 0$	$\Delta_{\mathrm{SO}} = 0$
$(X_\downarrow - iY_\downarrow), \Gamma_6(\Gamma_8)$	$(X_\downarrow - iY_\downarrow), \Gamma_6(\Gamma_5)$
$(X_\uparrow + iY_\uparrow), \Gamma_6(\Gamma_8)$	$(X_\uparrow + iY_\uparrow), \Gamma_6(\Gamma_5)$
$[X_\uparrow - iY_\uparrow + 2Z_\downarrow], \Gamma_7(\Gamma_8)$	$Z_\downarrow, \Gamma_7(\Gamma_4)$
$[X_\downarrow + iY_\downarrow - 2Z_\uparrow], \Gamma_7(\Gamma_8)$	$-Z_\uparrow, \Gamma_7(\Gamma_4)$
$[-X_\uparrow + iY_\uparrow + Z_\downarrow], \Gamma_7$	$-(X_\uparrow - iY_\uparrow), \Gamma_7(\Gamma_5)$
$[X_\downarrow + iY_\downarrow + Z_\uparrow], \Gamma_7$	$(X_\downarrow + iY_\downarrow), \Gamma_7(\Gamma_5)$

Table 2.1: Zone center wave functions in the cubic phase with SO interactions (left column) and in the tetragonal phase in the absence of SO interactions (right column).

when the states become confined at a heterointerface or in an external gate electric field. This is covered in detail in Chapter 5.

In the following section we discuss energy dispersion relations along symmetry lines and planes, which can be directly related to ARPES measurements and enable some qualitative insights into the relationships between Hamiltonian parameters and the field-orientation dependence of magnetoresistance-oscillation frequencies.

2.2.3 Energy dispersion relations for high-symmetry lines and planes

In general Eq.(2.4) must be diagonalized numerically. However, simple energy dispersion relations exist along high symmetry directions and in high-symmetry planes.

When the tetragonal distortion is large and SO interactions can be neglected,

the t_{2g} bands split into $\Gamma_4 + \Gamma_5$ bands. In this limit (to order $k^4/\Delta_{\rm T}$)

$$\begin{aligned} \epsilon_4(\boldsymbol{k}) &= \Delta_{\rm T} + \mathcal{M}_4 k_\parallel^2 + \mathcal{L}_4 k_z^2 \\ \epsilon_{5\pm}(\boldsymbol{k}) &= \mathcal{B}_+ k_\parallel^2 + \mathcal{M}_5^\perp k_z^2 \\ &\pm \sqrt{\mathcal{B}_- k_\parallel^4 - 4\left[\mathcal{B}_-^2 - \mathcal{N}_5^2\right] k_x^2 k_y^2} \end{aligned} \tag{2.15}$$

where $k_\parallel^2 = k_x^2 + k_y^2$ and $\mathcal{B}_\pm = (\mathcal{L}_5 \pm \mathcal{M}_5^\parallel)/2$. To leading order in $\Delta_{\rm SO}$, the Γ_4 energies remain unchanged whereas the $\Gamma_{5\pm}$ energies vary linearly in opposite directions. The energies (2.15) are valid for any value of $\Delta_{\rm T}$ (but still neglecting $\Delta_{\rm SO}$).

The $\boldsymbol{k}\cdot\boldsymbol{p}$ Hamiltonian for the t_{2g} bands in the cubic phase is identical to that of the valence band p-states of zinc-blende type semiconductors [67, 68]. In the presence of moderate SO interactions the dispersion relations along the three equivalent principle axes are

$$\begin{aligned} \epsilon_7(k) &= Mk^2 \\ \epsilon_{8\pm}(k) &= \mathcal{B}_+ k^2 + \frac{\Delta_{\rm SO}}{2} \\ &\pm \sqrt{\mathcal{B}_-^2 k^4 + \left(\frac{\Delta_{\rm SO}}{2}\right)^2 - \frac{\Delta_{\rm SO}}{3}\mathcal{B}_- k^2}. \end{aligned} \tag{2.16}$$

For strong SO interactions the ψ^7 and ψ^8 states can be approximately decoupled to order $k^4/\Delta_{\rm SO}$. The energy dispersions are then

$$\begin{aligned} \epsilon_7(k) &= \Delta_{\rm SO} + Ak^2 \\ \epsilon_8(\boldsymbol{k}) &= Ak^2 \pm \sqrt{B^2k^4 + C^2(k_x^2k_y^2 + k_x^2k_z^2 + k_y^2k_z^2)} \end{aligned} \tag{2.17}$$

where $A = 1 + (L+2M)/3$, $B = (L-M)/3$, and $C^2 = \left[N^2 - (L-M)^2\right]/3$. Expressions (2.17) were obtained by Dresselhaus et al.[[67]]. It is also possible to exactly diagonalize the Hamiltonian in the limit of infinite Δ_{SO}. We delay this calculation until Chapter 4.

ARPES measurements are frequently set to measure the energy dispersion in the $k_x - k_y$ plane. For $k_z = 0$ the dependence of band energies on momenta is similar in the dominant tetragonal-splitting and dominant spin-orbit coupling limits(compare Eqs.(2.15) and (2.17)). One way to determine which of the two interactions is dominant is to probe the dispersion relation along $\hat{\boldsymbol{z}}$. A second way is to monitor the

evolution of the bands as a function of temperature. Additional methods are explained in section 2.3 below.

The parameters of the effective Hamiltonian in the tetragonal phase are temperature dependent. As T is lowered the tetragonal distortion increases and the energy bands change accordingly. For some crystals, such as $SrTiO_3$, the deformation is well described by a simple order parameter[69]. It is then possible to express the temperature dependence of the different Hamiltonian parameters via a single temperature dependent order parameter.

2.3 Experimental methods for determining Hamiltonian parameters

The utility of the $\boldsymbol{k}\cdot\boldsymbol{p}$ method depends on the ability to extract accurate values for the Hamiltonian parameters from experiments. ARPES, magneto-transport, and Raman spectroscopy measurements are three of the most useful experimental probes for band parameters. In this section we focus on the ways in which these techniques can be exploited for d^0 perovskites with an emphasis on experimental signatures of the tetragonal distortion.

2.3.1 Raman spectroscopy

Raman spectroscopy is routinely used to measure the spectra of solids[68]. For a low doped d^0 perovskite Raman spectra can determine the band splitting at the zone center. As explained in section 2.2.3 distinguishing between Δ_{T} and Δ_{SO} using ARPES measurements may prove difficult. The band gaps depend both on SO interactions and on the tetragonal distortion. Spectroscopically monitoring the energy gaps as a function of temperature and comparing with Eqs.(2.11) provides in principle sufficient information to determine Δ_{SO} and Δ_{T}.

2.3.2 ARPES

Angle Resolved Photoemission Spectroscopy (ARPES) has now been developed into a widely applicable experimental tool for the measurement of bulk and surface electronic states[70, 71]. In a typical measurement incident monochromatic radiation excites electrons in occupied crystal states and unbinds them from the crystal. In the *sudden approximation* electrons are promoted directly from a crystal state

to a vacuum plane wave state. In this approximation the intensity of the ARPES signal associated with in-plane electron momentum $\boldsymbol{k}_\parallel$ and energy ω is

$$I\left(\boldsymbol{k}_\parallel, \omega\right) \propto \sum_n |M_{\boldsymbol{p}, n\boldsymbol{k}_\parallel}|^2 \mathcal{A}_n\left(\boldsymbol{k}_\parallel, \omega\right) f(\omega). \tag{2.18}$$

Here the z-axis is set perpendicular to the sample's surface and we assume that the photon energy is calibrated to probe the $k_z = 0$ plane. (The $k_z = 0$ plane can be emphasized experimentally by varying photon energies until the measured binding energy at $k_x, k_y = 0$ reaches an extremum. In principle, this procedure can also be used to distinguish surface states (that have no k_z dispersion) from bulk states.) $\mathcal{A}_n$ is the electron spectral function of band n, f is the Fermi distribution function, and

$$M_{\boldsymbol{p}, n\boldsymbol{k}_\parallel} \simeq \langle \boldsymbol{p}|\boldsymbol{A}\cdot\hat{\boldsymbol{p}}|\Psi_{n\boldsymbol{k}_\parallel}\rangle = \boldsymbol{A}\cdot\boldsymbol{p}\langle \boldsymbol{p}|\Psi_{n\boldsymbol{k}_\parallel}\rangle \tag{2.19}$$

gives the probability amplitude for an electron in an initial state $\Psi_{n\boldsymbol{k}_\parallel}$ to transition to a plane wave state $\boldsymbol{p}$ via a photon field $\boldsymbol{A}$. The photo-emitted electrons are selectively collected according to their emission angle and energy. Therefore in a given measurement the outgoing momentum $\boldsymbol{p}$ in Eq.(2.18) is fixed by the position of the detector and by the energy of the incoming photon. The component of the momentum parallel to the surface must equal the momentum of the initial state to within a surface reciprocal lattice vector.

In principle with sufficient ARPES data the occupied energy bands can be accurately mapped. The $\boldsymbol{k}\cdot\boldsymbol{p}$ Hamiltonian parameters can then be determined using the dispersion relations in section 2.2.3. In practice, however, experimental limits on energy and momentum resolution combined with the relatively large number of Hamiltonian parameters and the possibility of surface states that obscure bulk bands, often complicate comparisons between theory and experiment.

As we now explain, additional band structure information can sometimes be drawn from systematics in the dependence of the ARPES matrix elements on the surface reciprocal lattice vector added to the transverse momentum. Matrix elements contributions from particular t_{2g} orbitals frequently vanish at particular reciprocal lattice vectors either because of symmetry considerations or because of photon polarizations. By noticing the reciprocal lattice vectors at which the signal from a particular band is absent or very weak, it may be possible to identify the t_{2g} components which contribute dominantly to that band. This orbital information strongly constrains the band model.

Using the sudden approximation

$$\begin{aligned}\langle \boldsymbol{p}|\Psi_{n\boldsymbol{k}_\parallel}\rangle &= \sum_{\boldsymbol{G}_\parallel} \delta_{\boldsymbol{k}_\parallel+\boldsymbol{G}_\parallel,\boldsymbol{p}_\parallel} \sum_j a_j^{(n)}(\boldsymbol{k}_\parallel) \\ &\times \int \boldsymbol{dr}dz e^{-i[(\boldsymbol{G}_\parallel \boldsymbol{r}+p_z z)} \xi_j(\boldsymbol{r},z). \end{aligned} \tag{2.20}$$

Here $\boldsymbol{G}_\parallel$ is the surface-plane projection of a reciprocal lattice vector, and ξ_j are the t_{2g} basis functions given by Eq.(2.5) for the conduction band initial wavefunction: $\Psi_{n\boldsymbol{k}_\parallel} = \exp\left(i\boldsymbol{k}_\parallel \boldsymbol{r}\right) \sum_j a_j^{(n)} \xi_j$. The δ-function in Eq.(2.20) reflects the conservation of the in-plane crystal momentum in the photon assisted scattering process of the electron.

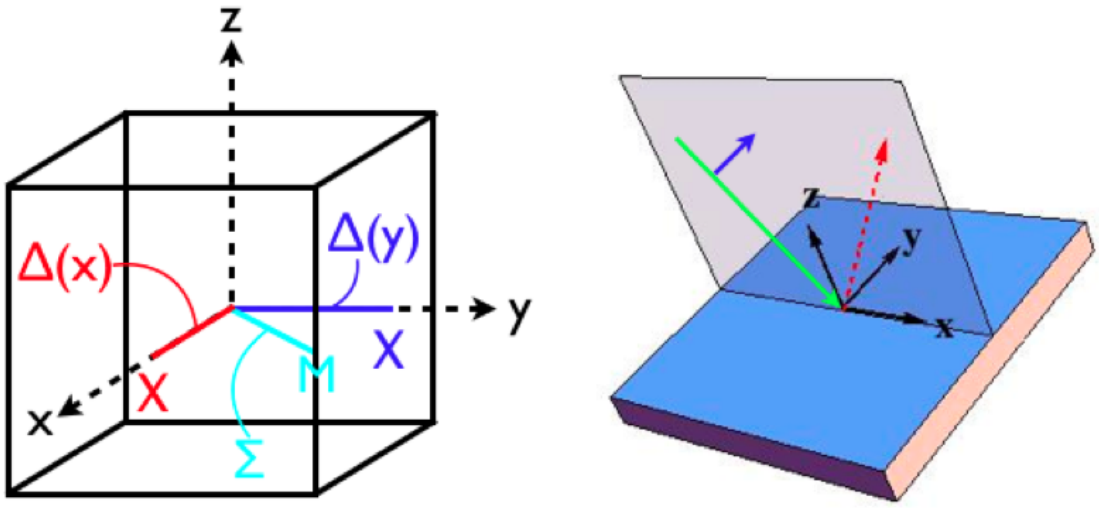

Figure 2.1: Left: High symmetry points and lines in the Brillouin Zone (BZ) of a simple cubic lattice. Right: Experimental geometry used in simulations of ARPES data in the [10] BZ. The photon source (green), with polarization in the xz-plane (blue), excites an electron to a high energy state that is emitted towards the detector (red dashed). Although the experimental geometry is unchanged by a reflection through the xz-plane, the yz and xy orbitals are odd under this operation. This leads to measurement of only the zx band in this measurement.

We illustrate the usefulness of the matrix element effect by considering M for $\boldsymbol{G} = \boldsymbol{0}$ ([00] BZ) and for $\boldsymbol{G}$ along the x-axis ([10] BZ). In the first case M always

vanishes since all ξ_j's are odd with respect to reflection by either the z-x or the z-y plane. There is therefore no ARPES signal in the [00] BZ for t_{2g} conduction band states. For the [10] BZ

$$M^{[01]} \propto \int \boldsymbol{dr} dz e^{-i(G_x x + p_z z)} Y(\boldsymbol{r}, z). \tag{2.21}$$

Contributions from other t_{2g} components of Ψ_i vanish because of their reflection symmetry in the x-z mirror plane (see Fig.2.1). Therefore only wave functions containing a Y orbital will be detected in this case. Recent experiments[51, 72] on bulk $SrTiO_3$ find a single (doubly degenerate) band for $k_z = 0$ in the [01] BZ in the cubic as well as in the tetragonal phase (see section 2.4). The Hamiltonian described by Eqs.(2.6—2.10) then indicates that the $\mathcal{N}$'s and $\Delta_{\rm SO}$ must be sufficiently small so that any hybridization between the t_{2g}-orbitals is negligible. The smallness of $\mathcal{N}$ can be justified convincingly from the perspective of tight-binding. This is addressed in Chapters 5 and 6

To illustrate the influence of the Hamiltonian parameters on the ARPES signal we numerically generate such a signal using Eq.(2.18). The resolution of a signal is determined by the width of the spectral function in Eq.(2.18). In accord with experiments[72] we set the energy resolution to 10meV throughout this work. The result for the [10] BZ is depicted in Fig.2.2 for the case of $\Delta_{\rm SO} = 0$ and $N = 0$. Only the xz-band is observed demonstrating the lack of hybridization between different t_{2g} bands.

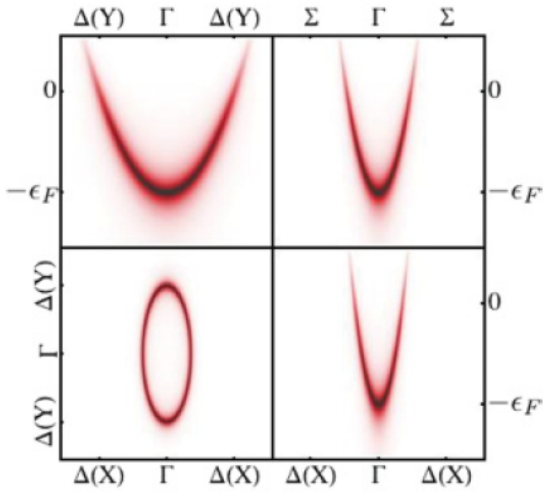

Figure 2.2: Simulated ARPES signal in the [10] BZ across the $k_z = 0$ plane for a temperature of $120K$, $L/M = 1/8$, $\Delta_{\text{SO}} = 0$, and $N = 0$. Only a single elliptical FS cross-section is seen (bottom left). Energy distribution curves (EDCs) have been included along several high symmetry directions - in this case showing only a single band associated with the xz basis state.

As evident from the Hamiltonian (2.3) and illustrated in Fig.2.3 the t_{2g} d-orbitals are hybridized by N. The influence of N is most pronounced along the main diagonals. For example in the [110] direction N induces a momentum dependent gap of $2Nk^2$.

Spin-orbit interactions will also mix the t_{2g} d-orbitals. However, in contrast to the $N \neq 0$ scenario they have no preferential direction. In $5d$ systems for which the SO splitting may be larger than the Fermi energy, the ARPES spectrum along the Σ direction is similar to the spectrum in the $N \neq 0$, $\Delta_{\text{SO}} = 0$ case. However, unlike the $N \neq 0$ case the photoemission spectrum is also altered along the $\hat{\boldsymbol{x}}$ and $\hat{\boldsymbol{y}}$ directions. This is evident along k_x in the simulated ARPES data of Fig.2.3, where the induced hybridization of the basis functions cause the previously dark band to become visible.

In $3d$ and $4d$ systems, where the Fermi energy and SO energy may be comparable, a detailed analysis of the EDCs may be necessary. For the sake of illustration, we consider several cases that elucidate some of the possible complications. The SO and tetragonal energies Δ_{SO} and Δ_{T} determine the band splitting at the Γ point (see Eq.(2.11)). In the cubic phase the value of Δ_{SO} can be extracted directly from an

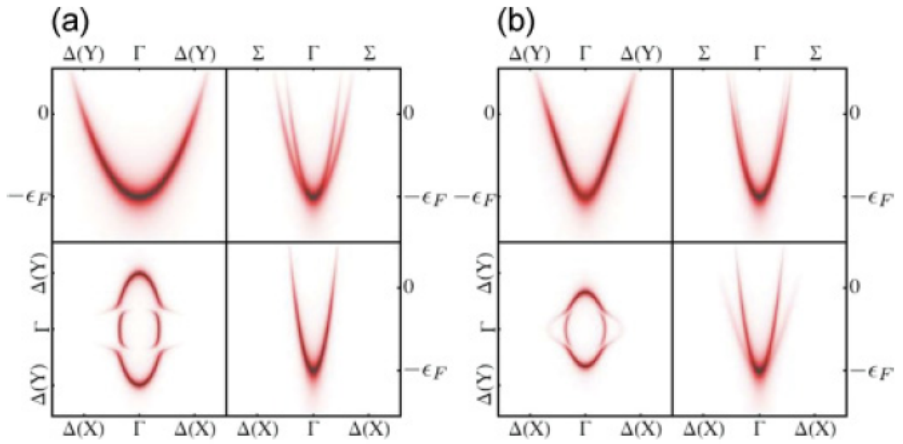

Figure 2.3: Simulated ARPES signal for a temperature of $120K$, $L/M = 1/8$, and $\Delta_{\mathrm{T}} = 0$. (a) For $N/M = 3$ and $\Delta_{\mathrm{SO}} = 0$ the hybridization is most pronounced along Σ but unseen in the EDCs along $\Delta(X)$, and $\Delta(Y)$. (b) For $N/M = 0$ and $\Delta_{\mathrm{SO}} = 3\epsilon_F$ one band has moved above the Fermi energy. The hybridization between the basis states is seen in the EDCs along all directions. This experimental feature can be attributed to the lack of a preferential direction of the SO interaction.

ARPES measurement in the [10] surface BZ (see Fig. 2.4a). This simple picture is complicated in the tetragonal phase. The case where $\Delta_{\mathrm{SO}} > \epsilon_{\mathrm{F}}$ and $\Delta_{\mathrm{T}} < \epsilon_{\mathrm{F}}$ is readily distinguished from the opposite limit by analysis of the dispersion along k_x. As evident from Figs. 2.4b and 2.4c only in the case where $\Delta_{\mathrm{SO}} > \epsilon_F$, is the dark weakly dispersive band visible away from the Γ point. When both Δ_{SO} and Δ_{T} are less than the Fermi energy, the energy distribution curves (EDCs) at the Γ point can be used to distinguish between the two cases. This can be seen in Fig. 2.5.

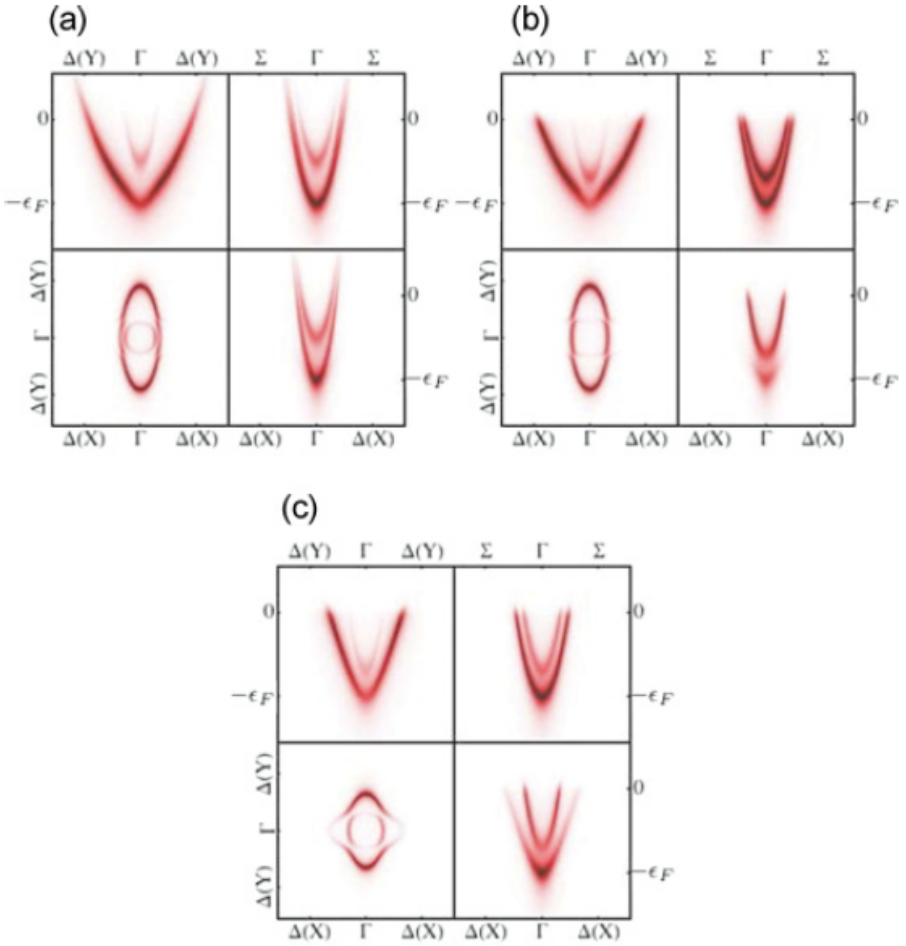

Figure 2.4: Simulated ARPES measurement for the [10] BZ for different values of $\Delta_{\rm SO}$ and $\Delta_{\rm T}$. $L/M = 1/8$, and $N = 0$ in all figures. (a) $T = 120K$, $\Delta_{\rm SO} = 0.5\epsilon_{\rm F}$, $\Delta_{\rm T} = 0$. As evident from all EDCs the SO splitting hybridizes the basis states. If the temperature is lowered, inducing a structural phase transition that is large, one band moves above the Fermi energy. This relatively weak hybridization is seen in the Fermi surface (FS) of (b) where $T = 20K$, $\Delta_{\rm SO} = 0.5\epsilon_{\rm F}$, $\Delta_{\rm T} = 3\epsilon_{\rm F}$. In contrast, for $T = 20K$, $\Delta_{\rm SO} = 3\epsilon_{\rm F}$, $\Delta_{\rm T} = 0.5\epsilon_{\rm F}$ the strong hybridization of the basis states leads to a more symmetric FS (c). This feature is also seen by comparing the EDCs of (b) and (c).

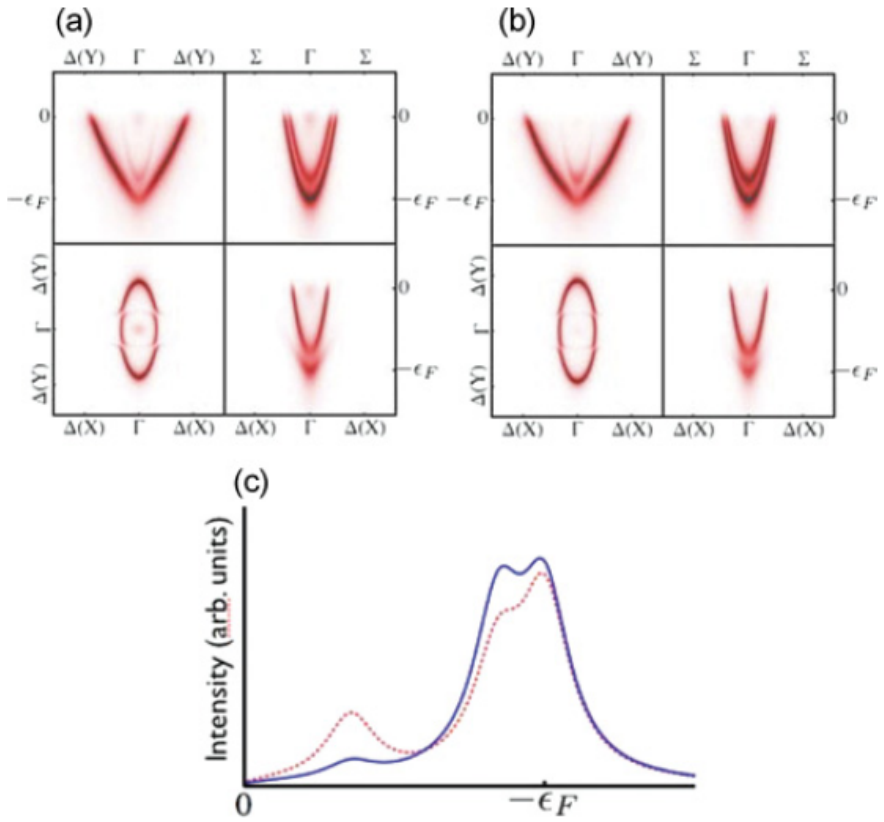

Figure 2.5: When $\Delta_{\rm SO}$ and $\Delta_{\rm T}$ are both small, although all three bands can be seen directly in a measurement of the [10] BZ it can be unclear how to extract these parameters. This is seen by comparing (a) where $\Delta_{\rm SO} = .5\epsilon_{\rm F}$. $\Delta_{\rm T} = 0.3\epsilon_{\rm F}$ with (b) where $\Delta_{\rm SO} = 0.3\epsilon_{\rm F}$. $\Delta_{\rm T} = 0.5\epsilon_{\rm F}$. A careful analysis of the EDC at the Γ point can distinguish between the two scenarios. This is shown in (c) where the Γ point EDC is shown for (a) in dashed-red and for (b) in blue.

2.3.3 Magnetic Oscillations

Magnetic oscillations in various physical properties such as the conductivity (Shubnikov - de Haas effect) and the magnetic susceptibility (de Haas - van Alfen effect) provide invaluable information on the band structure of solids[73–76]. The frequency of the oscillations F is related to the extremal cross-sectional area A_k of the Fermi surface in a plane perpendicular to the magnetic field through the Onsager

relation $F = \phi_0 A_k / 4\pi^2$. Here $\phi_0 = hc/e$ is the magnetic flux quantum. Measuring F as a function of charge density, magnetic field orientation, and temperature also makes it possible in principle to determine all the phenomenological Hamiltonian parameters.

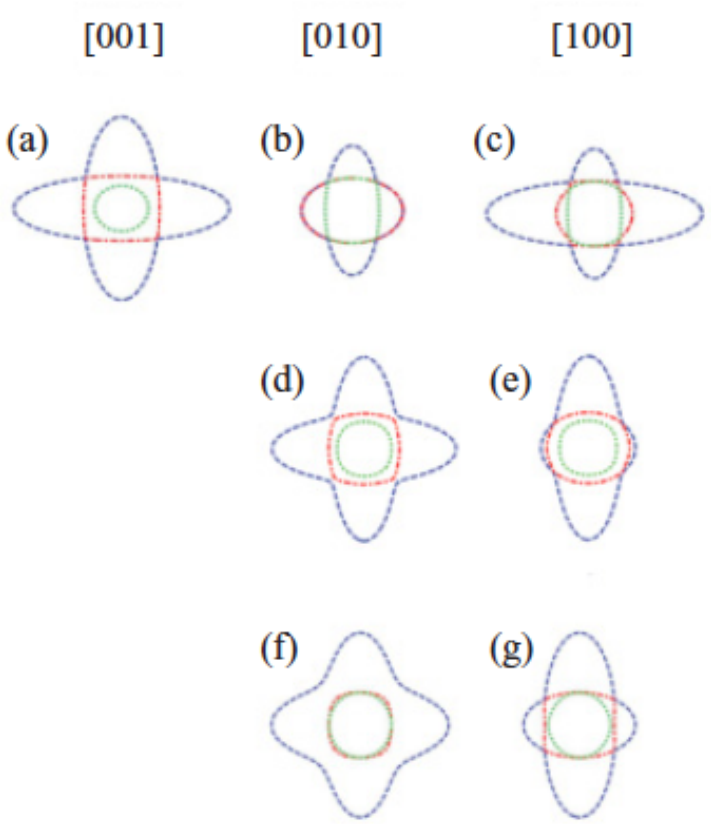

Figure 2.6: Extremal cross sectional areas for magnetic field oriented along [001] (left) [010] (center) and [100] (right). The extremal orbits have been organized by size from largest to smallest and shown as dashed-blue, dot-dashed-red, and dotted-green, respectively. Top row (a-c) corresponds to $\Delta_{\mathrm{T}} = 0.5\epsilon_{\mathrm{F}}$, middle row (d,e) corresponds to $\Delta_{\mathrm{SO}} = 0.5\epsilon_{\mathrm{F}}$, and bottom row corresponds to $N = 0.5M$.

In the naive picture of three ellipsoidal decoupled d-bands the cross sectional areas are simply given by ellipses. However this oversimplified scenario breaks down for any realistic system due to the hybridization of the d-orbitals by N, and by the

SO interactions. Avoided crossings of the overlapping energy bands then result in more complicated energy surfaces.

To illustrate the variety of possible shapes of electron pockets we consider a simple case with a small but finite band mixing (e.g. $N \gtrsim 0$).

The cross sectional areas for three high symmetry directions of the magnetic field are depicted in the top row of Fig.2.6 for the tetragonal phase. As $\Delta_{\rm T}$ increases the most energetic band is gradually depleted and the electronic charge is redistributed amongst the other two Fermi pockets. Eventually for $\Delta_{\rm T}/\epsilon_{\rm F} > 1 - \min(L/M, M/L)$ there is no band crossing between the xy-band and the other two bands.

Avoided crossings in the cubic phase result in non-elliptical cross-sections as well. The extremal cross-sectional areas along high symmetry directions are depicted in Fig.2.6 for $\Delta_{\rm SO}/\epsilon_{\rm F} = 0.5$ (center row) and for $N/M = 0.5$ (bottom row).

Our discussion ignores the possibility of multiple domains in the distorted state, and neglects magnetic breakdown. The latter is likely present in magnetic oscillation measurements on these materials because of the close approaches between extremal cross-sections [77] belonging to different bands.

2.4 $SrTiO_3$

Although STO has been studied for many years, there are only a few experimental results that can shed light on the structure of its conduction bands. We therefore resort to a 5-parameter model in which the Hamiltonian is parameterized by $\Delta_{\rm SO}, \Delta_{\rm T}, M, N$, and L, *i.e.* h is approximated by its cubic phase form.

The experiments that do exist appear to partially contradict one another. Based on Raman spectroscopy and Shubnikov de-Hass measurements Uwe *et al.*[48, 49] concluded that $\Delta_{\rm SO} \approx 18$meV and $\Delta_{\rm T} \approx 1.5$meV. On the contrary, Chang *et al.*[51] using ARPES do not observe a SO induced gap at the zone center and conclude that $\Delta_{\rm T} \approx -25$meV.

Supporting evidence for the smallness of $\Delta_{\rm SO}$ is provided by the matrix element effect. Experiments[51] observe only, what should be according to our matrix element analysis, the X orbital in the [10] BZ and the Y orbital in the [01] BZ. As explained in section 2.3.2, the lack of hybridization between t_{2g} orbitals implies that both $\Delta_{\rm SO}$ and N are very small. Additional proof that $N \ll M, L$ is provided by the ARPES EDCs which reveal no special features of the energy along Σ. In addition, these curves yield

values for the effective masses from which it follows that

$$M \approx 0.84 \ , \ L \approx 0.14. \tag{2.22}$$

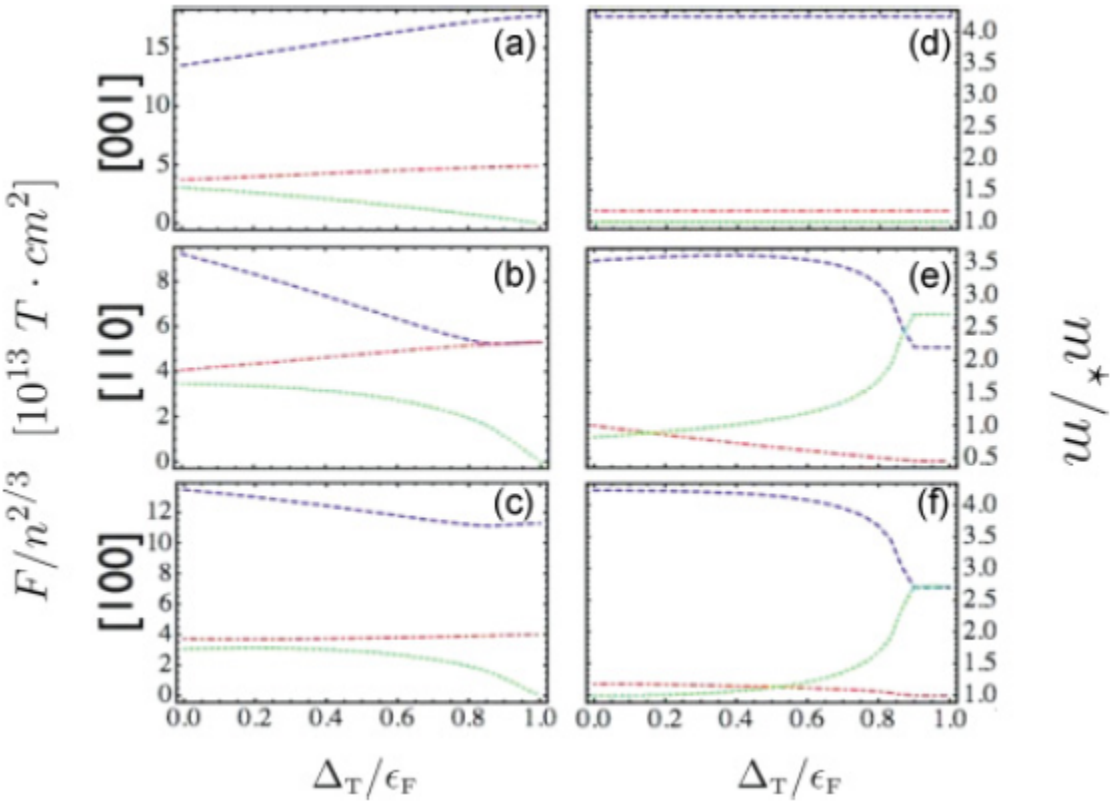

Figure 2.7: Dependence of magnetic oscillation frequency and cyclotron mass on $\Delta_{\rm T}$. Here we set $L/M = 1/8$, $N = 0$, and $\Delta_{\rm SO} = 0$. (a,b,c): Scaled SdH frequency for magnetic fields along [001], [110], and [100] as a function of Δ_t. (d,e,f): Cyclotron mass as a function of $\Delta_{\rm T}$.

Raman spectroscopy measurements[49] find energy gaps of approximately 2meV and 18 meV between conduction bands at the Γ point suggesting that $\Delta_{\rm T}$ and $\Delta_{\rm SO}$ have very different magnitudes. The larger of the two scales can be identified as tetragonal or spin-orbit from the dependence of magnetic oscillation frequency F and cyclotron mass $m^\star$ on density and field orientation. Fig.2.7 depicts the dependence of F and $m^\star$ on density and on $\Delta_{\rm T}$. The dependence can be expressed through a single

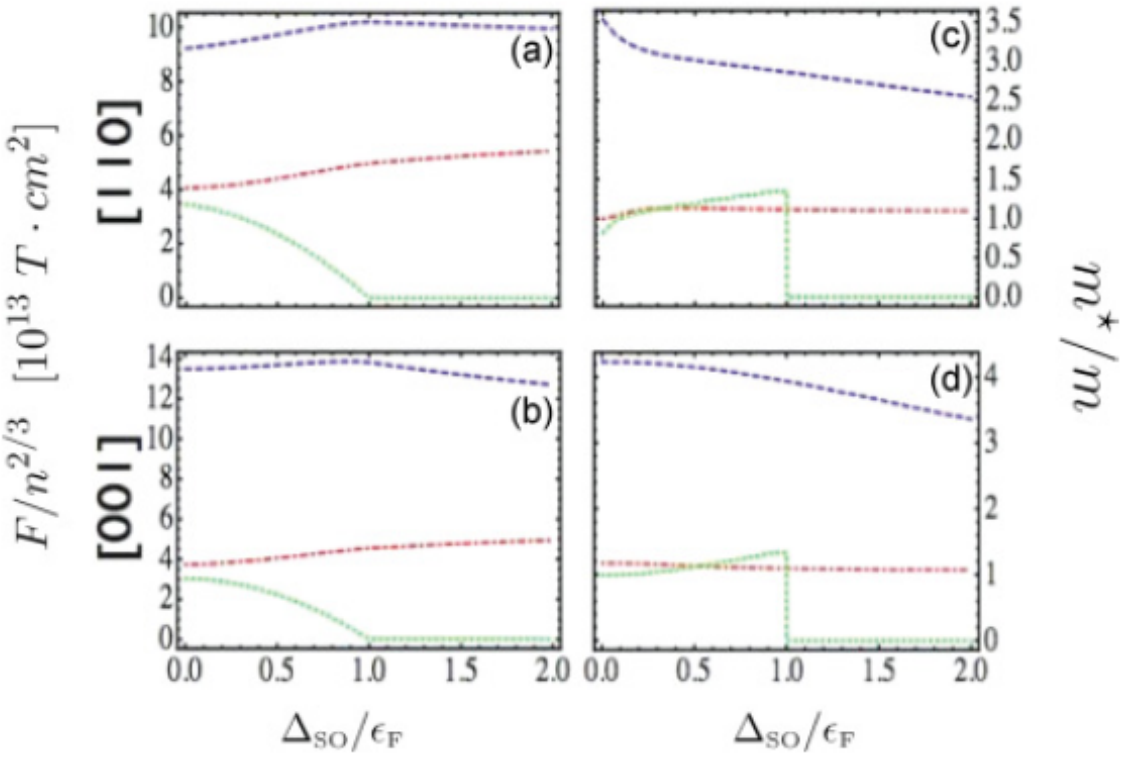

Figure 2.8: Dependence of magnetic oscillation frequency and cyclotron mass on Δ_{SO}. Here $L/M = 1/8$, $N = 0$ and $\Delta_{\text{T}} = 0$. (a,b): Scaled SdH frequency for magnetic fields along [001], [110], and [100] as a function of Δ_{SO}. (c,d): Cyclotron mass as a function of Δ_{SO}.

parameter $\Delta_{\text{T}}/\epsilon_{\text{F}}$ if F is scaled with $n^{2/3}$ where n is the electronic density. Similar graphs are given in Fig.2.8 for a scenario in which $\Delta_{\text{T}} \ll \Delta_{\text{SO}}$. The different trends of F and $m^\star$ as a function of density clearly distinguishes between the $\Delta_{\text{T}} \gg \Delta_{\text{SO}}$ scenario and its opposite counterpart.

2.5 Summary

d^0 Perovskites have played a centeral role in various areas of solid state physics and are now emerging as important building blocks for oxide-based heterostructures. In this chapter, we have used the $\boldsymbol{k}\cdot\boldsymbol{p}$ theory to construct the general low energy theory

for the conduction bands of these materials both in the cubic and in the tetragonal phases. We then employed the theory to estimate the Hamiltonian parameters for STO. A more detailed analysis of the parameters is the focus of Chapter 4 where a SdH study of a series of lightly doped STO samples in magnetic fields up to 40 Tesla is analyzed. But first, in Chapter 3 the matrix element effect described in Section 2.3.2 is used measure the deformation potentials of doped STO.

Chapter 3

Uniaxial strain induced band splitting in semiconducting SrTiO3

In this chapter, the matrix element effect of Section 2.3.2 is used to experimentally measure the deformation potential in the t_{2g} conduction band of doped $SrTiO_3$ using photoemission. Experimental observation of orbital splitting between the Ti $3d_{yz}$ and $3d_{xy}$ bands, which are degenerate when unperturbed is seen in the presence of uniaxial strain. Using the $\mathbf{k}\cdot\mathbf{p}$ method, we qualitatively explain the direction and the size of the observed energy splitting. The gained understanding of band splitting explains the strain-induced mobility enhancement[78] of electron-doped $SrTiO3_3$ in terms of degeneracy breaking within the t_{2g} manifold.

3.1 Introduction

Strain can play a vital role in controlling the physical properties of crystals. Changes in the band structure, such as band splitting and warping, can be triggered by small variations in the lattice parameters. Sizable strain-induced modifications of the electronic structure have been observed in various materials ranging from metals[79, 80] and semiconductors [81, 82], to oxides [83–85]. Semiconductors with degeneracies at band edges, such as those that occur at the top of the valence band in silicon and

germanium, are especially sensitive to strain. For this reason both uniaxial and biaxial strain engineering have been successfully applied to improve current semiconductor electronics technology while maintaining the traditional device fabrication process[82].

The oxide semiconductor $SrTiO_3$ and its heterostructures have attracted much attention for the energy-harvesting applications, such as solar water splitting[86] and its use in thermoelectric devices [87], the efficiency of which can be improved by tuning the band gap or electron mobilities, and for the next-generation electronic device applications [88], in which superconductivity [30], magnetism [89], and interface orbital reconstruction[90] may become important. Control of these properties can be driven by our understanding of the band structure changes upon induced strain [78, 91, 92]. Recent experiments suggest that the mobility of $SrTiO_3$ can be enhanced by a factor of three under uniaxial compressive strain [78], demonstrating the potential of strain-engineering in oxide semiconductors. Moreover, theoretical calculations on $SrTiO_3$ have shown that anisotropic strains can reduce the band gap, which is a key driver to improving efficiency of solar energy harvest, by breaking degeneracies at the band edges[91]. In spite of a considerable effort, at present a comprehensive picture of the strain-triggered electronic structure changes is missing even in this widely studied material.

Here we study the effect of mechanically induced uniaxial strain on the degenerate conduction band structure of the electron-doped $SrTiO_3$. We observe the degeneracy breaking in the strained region, where a finite energy splitting appears, compared to the degenerate band structure in the unstrained region. We interpret the observed effects in terms of a $\mathbf{k}\cdot\mathbf{p}$ model and estimate the strength of the associated

deformation potential.

3.2 Experimental

We apply uniaxial strain to $SrTiO_3$ single crystals (5×5×0.1 mm) in a three-point bending geometry. Figure 3.1(a) shows a schematic of the bent crystal, pushed up at the center with a thin piece of tantalum foil and clamped at both sides. The resulting curvature of the crystal shows two distinct regions, *i.e.*, the central curved region with tensile strain (S) and the side regions with nearly no strain (NS1,2). We estimate the amount of the tensile strain as $\sim 0.26\%$ from the lateral width ($\sim$ 1 mm) of the S region and the tilt angle (2°) between the two side regions [78]. The crystal is annealed in ultra high vacuum to introduce an electron concentration of $\sim 10^{20}$ cm^{-3}, as reported previously [51].

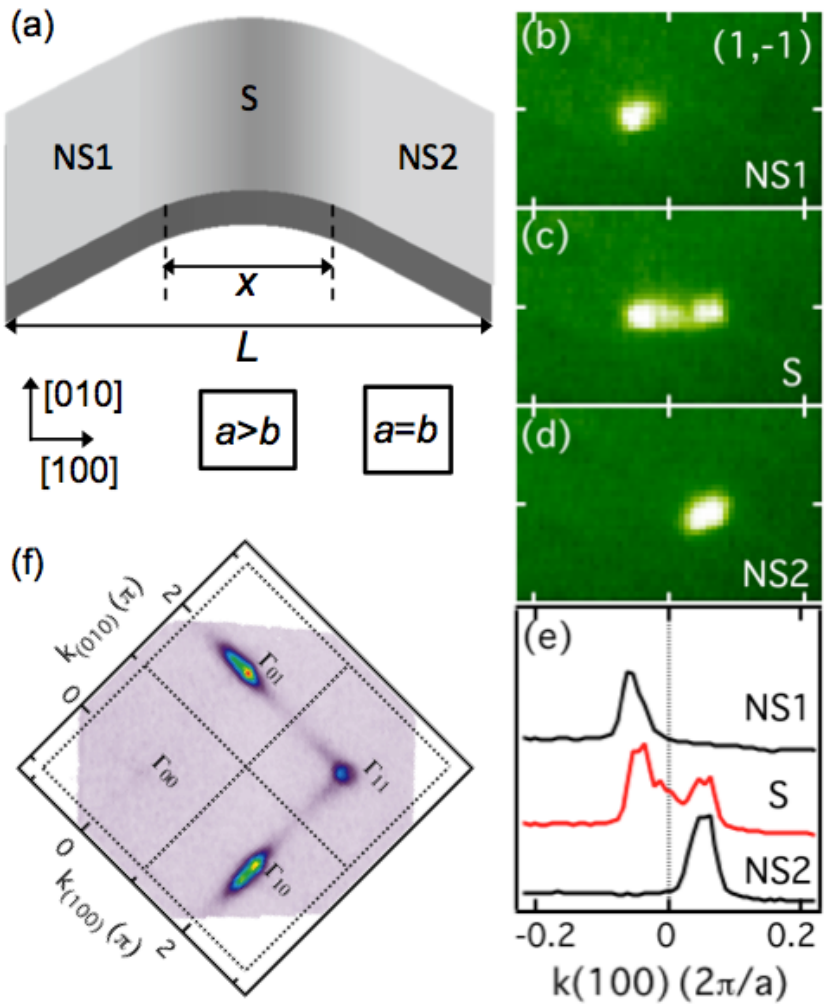

Figure 3.1: (a) A thin $SrTiO_3$ (001) single crystal is bent at the center (S) where the crystal is maximally curved, while both sides remain without a significant curvature (non-strained: NS). a and b represent the in-plane lattice constants. (b)-(d) (1,-1) LEED spot images taken at different locations in the same sample. The curved crystal surface changes the spot position and elongated the spot at the center where the LEED electron beam is larger than the S region. (e) Line profiles of the (1,-1) LEED spots in b-d along the horizontal axis. (f) Fermi surface cut of the electron-doped $SrTiO_3$ when rotated by 45° relative to the electron spectrometer's horizontal entrance slit. ($SrTiO_3$ lattice constant $a = 3.905$ Å and $\pi/a = 0.805$ Å^{-1})

The strained $SrTiO_3$ crystal shows a sharp low-energy electron diffraction (LEED) pattern. Figure 3.1 (b-d) show the (1,-1) spots taken at the three different regions with the same sample alignment. While LEED shows a sharp spot at the NS regions, in the S region it gives an elongated spot. This is due to the large electron beam diameter ($>$ 1 mm) of the LEED electron gun, which exceeds the 1 mm-long curved region. Therefore, the line profile along the horizontal axis indicates that the elongated spot consists of a combination of the sharp spots taken in the side regions, as shown in Fig. 3.1(e).

The ARPES measurements were performed at the Electronic Structure Factory endstation at beamline 7.0.1 of the Advanced Light Source, equipped with a hemispherical Scienta R4000 electron analyzer. We conducted measurements at a sample temperature at 130 K using a photon energy of $\sim$ 100 eV and an overall energy resolution of 25 meV. The small spot size of the photon beam (50 μm) prevents any overlapping of the signal from the S and NS regions.

3.3 Results and analysis

Figure 3.1 (f) shows the Fermi surface cut of electron-doped $SrTiO_3$ measured over a wide momentum range. Since the light polarization is even with respect to the scattering plane, our measurement geometry allows us to access only the even initial states. The ensuing matrix element effects are very strong in $SrTiO_3$ (001), and have been explained in detail elsewhere[50] (Section 2.3.2). Electron-doped bulk $SrTiO_3$ has three degenerate conduction bands, i.e. Ti d_{xy}, d_{yz}, and d_{xz} states, corresponding to three perpendicular ellipsoidal Fermi surfaces [51]. The three degenerate Ti $3d$

t_{2g} states exchange their spectral weight among different Brillouin zones (BZs). For example, whereas no bands are visible in the [00] BZ, all are present in the [11] BZ, while the d_{yz} and d_{xz} bands are measured separately in the BZ [01] and [10], respectively. Since they do not show overlapping features from different states, the [01] and [10] BZs are the preferable choice for our measurement in order to get the clearest photoemission images of the respective electronic states.

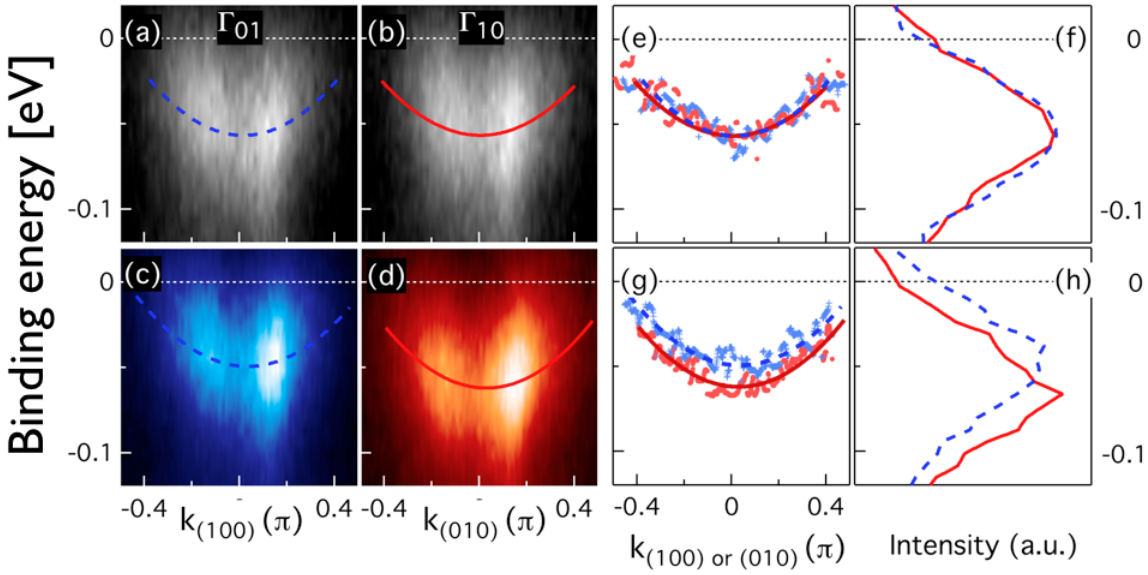

Figure 3.2: The energy-distribution curves of $SrTiO_3$ for ((a)-(d)) strained and [(e)-(h)] non-strained region near the Fermi level. The band structure cuts are taken for ((a) and (e)) BZ [01] and ((b) and (f)) BZ [10] along $k(100)$ and $k(010)$ axes in Fig. 3.1 (b), respectively. (c,g) Dispersions of peak positions in the energy-distribution curves with parabolic fitting lines. (d,h) Energy-distribution curves taken at $k(100)$(or $k(010)) = 0$.

Figure 3.2 compares the band dispersion in the S and NS regions. The ARPES maps are taken near the Γ_{01} and Γ_{10} points along $k(100)$ or $k(010)$ directions, *i.e.*,

along the major axis of the ellipsoidal constant energy contour. In the NS regions, the d_{yz} (Fig. 3.2 (a)) and d_{xz} (Fig. 3.2(b)) states disperse with the characteristic electron-like parabola with minimum at a binding energy of $\sim$ 55 meV. On the other hand, in the S region (Fig. 3.2 (c,d)), we observe clear changes of binding energies of the two orbital bands shifting in opposite directions.

This is shown more quantitatively in the energy distribution curve (EDC) analysis. The peak position of the EDCs, shown in symbols in Fig. 3.2 (e,g), are fitted by parabolic functions, shown as dashed and solid curves in Fig. 3.2 (a-e,g). The dispersion curves in Fig. 3.2 (e) can be perfectly superimposed since the d_{xz} and d_{yz} states are degenerate, reproducing our previous result in unstrained $SrTiO_3$[51]. Conversely, in Fig. 3.2 (g), the d_{yz} dispersion is lifted by 8 meV while the d_{xz} state is lowered by 5 meV. The difference becomes even more evident in the comparison of EDCs at Γ points, as shown in Fig. 3.2 (h). As a whole, the strained region shows a band splitting of 13 meV.

We have carefully tried to identified the changes caused by the external strain alone. The sample temperature was chosen to be at 130 K so that the $SrTiO_3$ single crystal remains cubic unless the external strain is applied. The effect of two possible systematic errors has been minimized by orienting the crystal as shown in Fig. 3.1 (f) relative to the electron spectrometer. First, second order non-linearity of the detected angular dispersion which appear in the angle dispersion plane (horizontal direction in Fig. 3.1(f)), and second, aberrations induced by changes in geometry as a function of sample polar angle relative to the photon-electron scattering plane. We precisely choose the band structure cuts along each Γ-X direction of the two BZs from wide

momentum space scans. Finally, we compared the measurements taken in the two different regions (S and NS) in the same sample to rule out the influence of local variations in sample quality. All these aspects minimize the systematic errors and ensure that the energy shifts in the S region is a genuine effect of uniaxial strain.

For a deeper understanding, we apply the $\mathbf{k}\cdot\mathbf{p}$ theory to model changes of the conduction band structure in $SrTiO_3$. This method is widely used to describe the band edges of strained semiconductors [81]. Its application to d^0 perovskites has been described by Bistritzer et al.[50]. Here we focus on the changes to the conduction band structure in $SrTiO_3$ due to an externally applied strain and assume that the spin-orbit splitting is below the experimental resolution.

Application of an external strain deforms the ionic potential and thus changes the crystal symmetry of the unit cell. Including this influence in the $\mathbf{k}\cdot\mathbf{p}$ theory results in a perturbation Hamiltonian of the form:

$$H' = \sum_{i,j} \left(-\frac{p_i p_j}{m_0} + \delta V_{ij} \right) \epsilon_{ij} \tag{3.1}$$

where p_i, m_0, δV_{ij}, and ϵ_{ij} are the ith component of the momentum, bare electron mass, change in the ionic potential, and components of the strain tensor, respectively [81, 93]. Here we have assumed inversion symmetry in the unstrained crystal structure. This perturbation Hamiltonian is then evaluated for the t_{2g} bands. The strain-induced change in the Hamiltonian has the form,

$$H'_{t_{2g}} = \begin{pmatrix} l\epsilon_{11} + m\left(\epsilon_{22} + \epsilon_{33}\right) & n\epsilon_{12} & n\epsilon_{13} \\ n\epsilon_{21} & l\epsilon_{22} + m\left(\epsilon_{33} + \epsilon_{11}\right) & n\epsilon_{23} \\ n\epsilon_{31} & n\epsilon_{32} & l\epsilon_{33} + m\left(\epsilon_{11} + \epsilon_{22}\right) \end{pmatrix}$$

written in the $\{ d_{yz} , d_{xz} , d_{xy} \}$ basis. Here l, m, and n are the deformation potentials which can be extracted from our experimental data. For a uniaxial tensile strain along the x-axis, $\epsilon_{11} = \epsilon$ and $\epsilon_{22} = \epsilon_{33} = -\nu\epsilon$ where ν is the Poisson ratio. All other strain components are zero. (An analysis of biaxial strain is also included in Appendix **??**.) The perturbation Hamiltonian then simplifies to,

$$\begin{pmatrix} (l - 2m\nu)\epsilon & 0 & 0 \\ 0 & (m(1-\nu) - l\nu)\epsilon & 0 \\ 0 & 0 & (m(1-\nu) - l\nu)\epsilon \end{pmatrix} \tag{3.2}$$

We find a Γ point splitting of $(l-m)(1+\nu)\epsilon$ between the d_{yz} band and the remaining t_{2g} bands. Because the relative change in the lattice constant along the x-axis is known from the geometry, comparing the splitting at the Γ point gives a direct measure of the deformation potentials relevant to the uniaxial strain ($\epsilon = 0.0026$). We find $l - m \approx 4.03$ eV, where we have used the Poisson ratio at 130K, $\nu = 0.242$ calculated from the results of Ref. [94]. We also note that the estimated deformation potential is similar in scale to that of conventional semiconductors ($1 - 10$ eV) [81].

Figure 3.3 shows the $\mathbf{k}\cdot\mathbf{p}$ fit to the ARPES band structure with and without uniaxial strain. In the cubic phase there are three bands that are degenerate at the Γ point (dashed lines), in the absence of spin-orbit splitting. However, when an elongation of the [100] axis is applied this degeneracy is partially lifted (solid lines).

While the d_{yz} band shifts up (Fig. 3.3(d)), the d_{xz} and d_{xy} band shift down (Fig. 3.3(e)). The $\mathbf{k}\cdot\mathbf{p}$ model thus accounts well for the energy shifts seen in ARPES experiments.

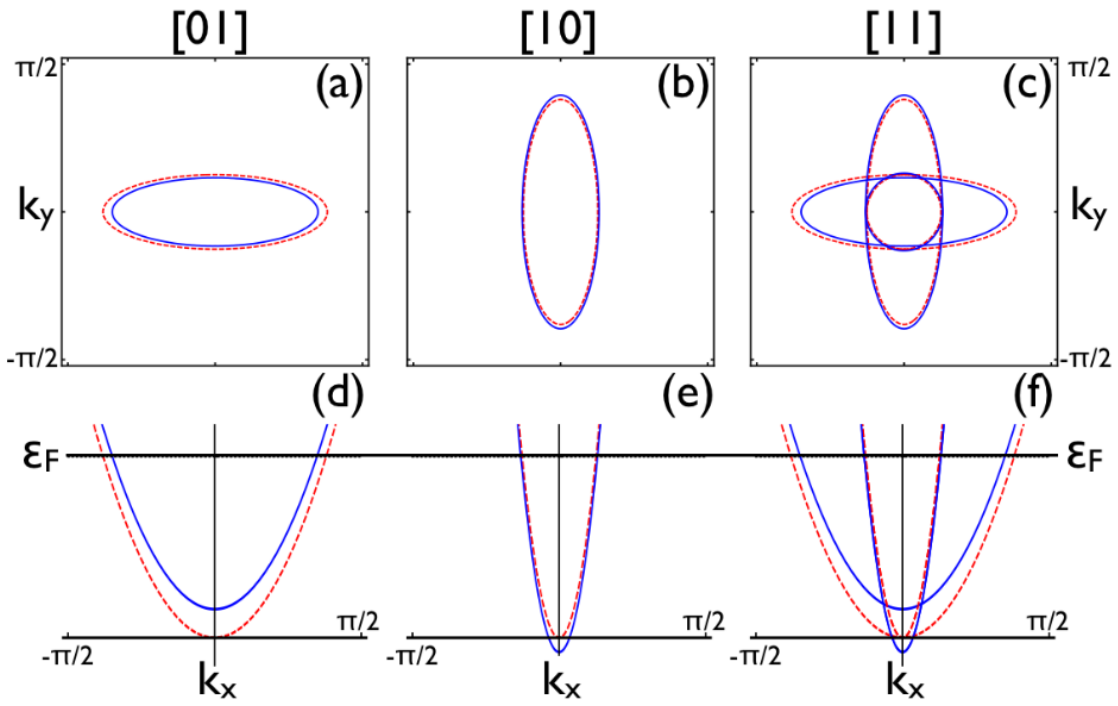

Figure 3.3: Calculated band structure of the $SrTiO_3$ with (solid lines) and without strain (dashed). (a-c) Fermi surface cuts for (a) BZ [01], (b) [10], and (c) [11]. (d-e) Band structure cuts along the horizontal axes in different BZs. The energy shifts due to strain are 8.7 meV for d_{yz} band (a,d) and -4.3 meV for the d_{xz} and d_{xy} bands (b,c,e,f). A constant energy shift due to particle conservation has been ignored in this figure.

3.4 Discussion

In strained silicon, bulk degenerate valence bands are split by a compression or a dilation. The repopulation of electrons into non-degenerate bands and the suppression of inter-valley phonon scattering enhance the electron carrier mobility [82]. The enhanced mobility of the electron-doped $SrTiO_3$ films under compression can be understood in similar terms. Strain breaks the three-fold t_{2g} band degeneracy, and repopulation then reduces the average effective mass and suppresses interband scattering [41, 82, 95]. We also note that the alignment of polar domains upon uniaxial stress, which are otherwise randomly oriented and scatter charge carriers at the domain walls, can also alter the electron mobility [85, 96].

We conclude that strain-induced electronic structure changes, combined with improvements in sample quality, can further increase the efficiency and functionalities of $SrTiO_3$ and other oxide applications [57]. With the deformation potential derived in the present study, we experimentally infer the band edge lowering of 13 meV for 0.26% uniaxial strain. By extensively testing theoretical predictions of the deformation potentials [41], it will be possible to provide accurate predictions of band structure changes for artificially designed strain state in heterostructure devices.

Our findings also highlight the advantage of ARPES, which is able to directly probe electronic states in momentum-space. As shown in Fig. 3.3(f), the three different bands overlap with a small energy splitting, which makes the detection of such small changes difficult. It is the possibility of measuring the three bands separately in different Brillouin-zones which permits the small energy shifts to be measured. Since $SrTiO_3$ represents a prototype perovskite oxide and serves as a widely

used substrate for other oxides, this approach can be further extended to different types (uniaxial and biaxial) of misfit strains in oxide heterostructures utilizing *in situ* preparation of oxide films [41, 91, 97, 98], similar to biaxial-strained silicon formed on $Si_{1-x}Ge_x$ substrates. Given the elaborate and successful development of strain engineering in semiconductor heterojunctions, it seems clear that this is a strong motivation for further studies of strain effects in oxide systems.

In summary, we report clear change of the electronic spectral function in the electron-doped $SrTiO_3$ due to the uniaxial strain using angle-resolved photoemission spectroscopy. When the crystal is stressed, we observe the energy splitting of the Ti $3d$ t_{3g} energy bands, otherwise degenerate. Consistent with the experimental finding, we qualitatively understand the splitting using the $\mathbf{k}\cdot\mathbf{p}$ theory. Our result suggests that the mobility enhancement due to uniaxial strain is mainly a result of the degeneracy breaking of the t_{2g} manifold. This completely changes the bandstructure for densities on the scale of samples studied in Ref. [78].

Chapter 4

Shubnikov-de Haas effect in low electron density SrTiO3: Conduction band edge of SrTiO3

In this chapter the Shubnikov-de Haas effect is used to explore the conduction band edge of high mobility $SrTiO_3$ films doped with La. The results largely confirm the earlier measurements by Uwe et al. [48]. The band edge dispersion differs significantly from the predictions of ab initio electronic structure theory.

4.1 Introduction

As previously discussed, strontium titanate is a perovskite oxide that is prominently featured in the emerging arena of oxide electronics [6, 88, 99]. Heterostructures formed between $SrTiO_3$ and other oxides exhibit an interfacial, two dimensional electron gas (2DEG) that can be controlled by applied electric fields[100], and for which relatively high 2D densities on the order of 3×10^{14} cm^{-2} can be achieved [18]. Furthermore, superconductivity[26, 30], ordered magnetic ground states[31–34] and the Kondo effect[28] are observed. In most cases, transport occurs on the $SrTiO_3$-side of the interface. A quantitative description of the conduction band states in bulk $SrTiO_3$ is essential[50] to model and theoretically understand the properties of confined 2DEGs.

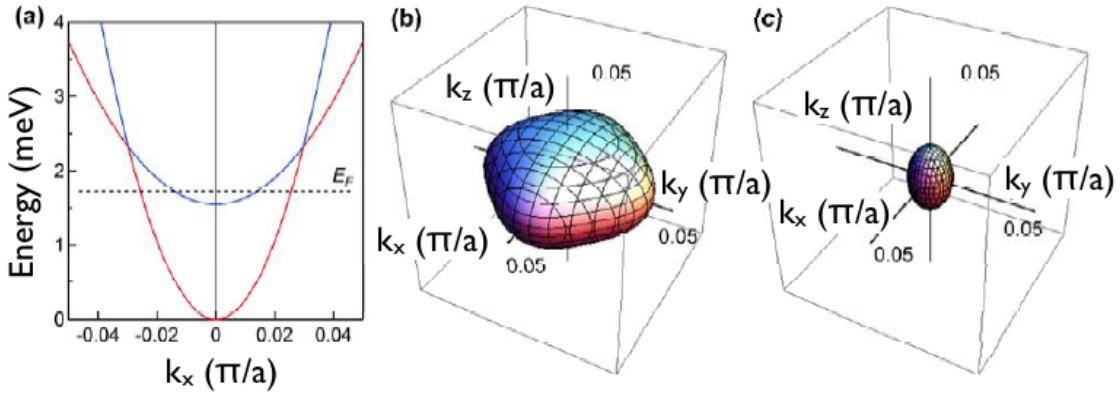

Figure 4.1: Dispersion at the conduction band edge using parameters from Uwe et al. in a model that includes relatively strong spin-orbit interaction. Fermi surfaces correspond to an electron density of 7.5×10^{17} cm^{-3}, and k is expressed in units of π/a where a is the length of the cubic $SrTiO_3$ unit cell. k_z is directed along the tetragonal c-axis.

The low energy conduction bands can be characterized by three t_{2g} Luttinger parameters, the spin-orbit interaction, and tetragonal distortion energies. More recently Uwe et al.'s results were questioned by ARPES experiments [51]. There has been no consensus on the relative strength of spin-orbit and tetragonal strain parameters responsible for band-splitting at the band edge. Accurate knowledge of the bulk bands is essential if progress is to be made toward understanding of 2DEGs in $SrTiO_3$.

Here we use the earlier results from Uwe et al. [48, 49] as a guide for Shubnikov de-Haas oscillation experiments in high mobility, lightly La-doped SrTiO3 films. Using the parameters determined by Uwe et al. [48, 49], Fig. 4.1 shows the dispersion along [001], and the Fermi surfaces and energy for an electron density of 7.5×10^{17} cm^{-3}. The model dispersion and Fermi surfaces shown here include the effect of a rel-

atively large spin-orbit interaction discussed further in our data analysis that follows. At the lowest doping concentration a single closed Fermi surface is expected, while higher concentrations cause the occupation of a higher band, which is split-off at low temperature by the tetragonal distortion of the unit cell. Its Fermi surface provides a tight constraint on the strain-induced splitting. At this concentration two bands are expected to be occupied. Our Shubnikov-de Haas experiments are carried out on samples that range from doping (or electron concentrations) that are sufficiently low that only one Fermi surface is filled, to higher concentrations in which two Fermi surfaces are filled, as depicted in Fig. 4.1. At the outset we note that although the results reported here differ quantitatively from Uwe et al.[48, 49], they substantially support their interpretation, despite the fact that their experiments were carried out at substantially higher doping concentrations, requiring them to extract extremal Fermi surface cross sections that were interconnected by magnetic breakdown.

The results reported here measure the Luttinger parameters[101] for the t_{2g} conduction band minimum. We are able to successfully interpret our experiments by assuming that the spin-orbit energy (measured by Uwe et al. to be ~ 17 meV [49]) is much larger than the Fermi energy at the electron density of the samples investigated here. The measured Luttinger parameters differ substantially from recent band structure models opening the possibility that the *ab initio* calculations are not accurate, or the band edge mass is substantially enhanced by electron phonon coupling[72], or a combination of both.

Sample number	Internal Sample reference number	Layer Thickness (nm)	1.8 K Hall electron density (cm^{-3})	1.8 K Hall mobility ($cm^2\ V^{-1}\ s^{-1}$)	SdH electron density (cm^{-3})
1	STO-216	1280	3.6×10^{17}	37,000	4.2×10^{17}
2	STO-181	800	12×10^{17}	32,000	18.2×10^{17}

Table 4.1: Samples investigated in this study.

4.2 Experimental

$SrTiO_3$ films doped with La were grown on (001) $SrTiO_3$ substrates by molecular beam epitaxy (MBE), as described elsewhere [57, 102]. These films exhibit the high mobility needed to observe the Shubnikov-de Haas effect and to explore the conduction band edge. Low temperature (1.8 K) Hall carrier density (calculated as $n = 1/(teR_H)$, where t is the film thickness, R_H the Hall coefficient, and e the elementary charge) and mobilities varied from 3.6×10^{17} cm^{-3} (mobility 37,000 cm^2 V^{-1} s^{-1}) to 12×10^{17} cm^{-3} (mobility $33,000$ $cm^2V^{-1}s^{-1}$). The thickness of the epitaxial layers varied from 800 nm to 1200 nm. While a total of five epitaxial layers were investigated, a complete set of data was taken and analyzed for the two samples referred to in the following as samples 1 and 2, see Table 4.1. Swept field magnetotransport experiments were carried out at the National High Magnetic Field Lab at temperatures down to 0.4 K and magnetic fields (B) to 31 T as a function of angle between the magnetic field and sample normal.

4.3 Results and Discussion

Results for sample 1 with the magnetic field aligned along [111] are shown in Fig. 4.2. The oscillatory features (relative resistance maxima) are indexed and

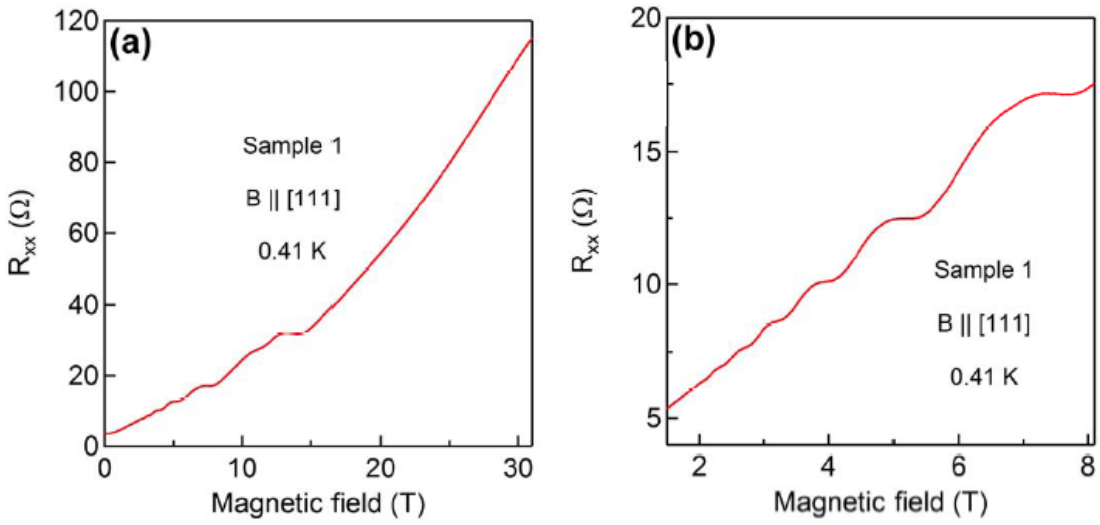

Figure 4.2: Shubnikov-de Haas oscillations with the magnetic field aligned along [111] for sample 1. (a) The quantum oscillations are exhausted at the quantum limit, $\sim$ 15 Tesla. (b) Features persist down to 2 Tesla.

plotted as a function of 1/B in Fig. 4.3; they display a straight line corresponding to an extremal Fermi surface cross section of $\sim$ 17.5 T. The extremal area, S_F, is related to the slope by $S_F = \frac{\partial n}{\partial(1/B)} 4\pi^2 \frac{e}{h}$. Figure 4.2 shows that the quantum limit is reached around this field and the oscillations begin to show a doubling of the resistance maxima as spin split Fermi surfaces are resolved.

Quantum oscillations for sample 2 with the magnetic field aligned along [001], the surface normal, are shown in Fig. 4.4. At low fields a weak, low frequency oscillation is detected and assigned to the Fermi surface for electrons in the band split-off from the conduction band minimum by the tetragonal strain. As in sample 1, at the highest fields the resistance maxima split, due to the spin split Fermi surfaces. Indices for the relative resistance maxima for the two sets of oscillations are plotted

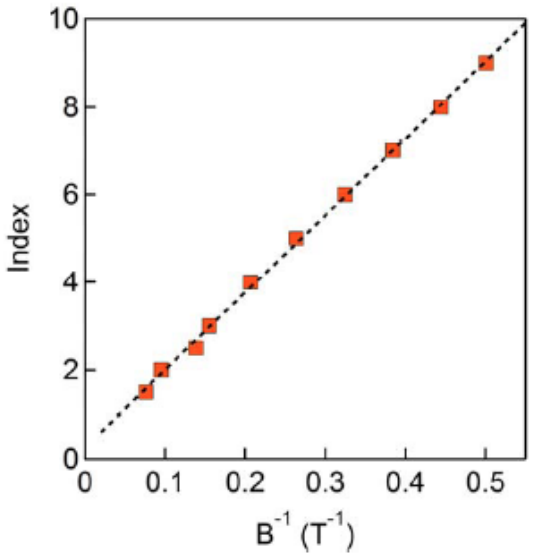

Figure 4.3: Sample 1. The relative maxima in Fig. 4.2, plotted vs. 1/B. Near the quantum limit a splitting appears. The slope of the line corresponds to an extremal area of 17.5 Tesla.

as a function of 1/B in Fig. 4.5. The corresponding extremal areas for the two Fermi surfaces for sample 2 along [001] are 55.2 and 9.55 T, respectively.

At 105 K, $SrTiO_3$ undergoes a phase transformation from cubic to a tetragonal phase. The tetragonal [001] direction (c-axis) can then select three different directions - normal to the sample surface or in two orthogonal directions in the plane of the film, corresponding to three orientation variants or domains. In this case the experimental results for any given orientation of the magnetic field could display several different periods of oscillation each corresponding to a particular domain. Each sample was measured along the three principal directions, [110], [111] and [001] defined such that [001] is the surface normal. Figure 4.6 shows the measured extremal area for the larger Fermi surface in sample 2 for these orientations. Also shown are the extremal

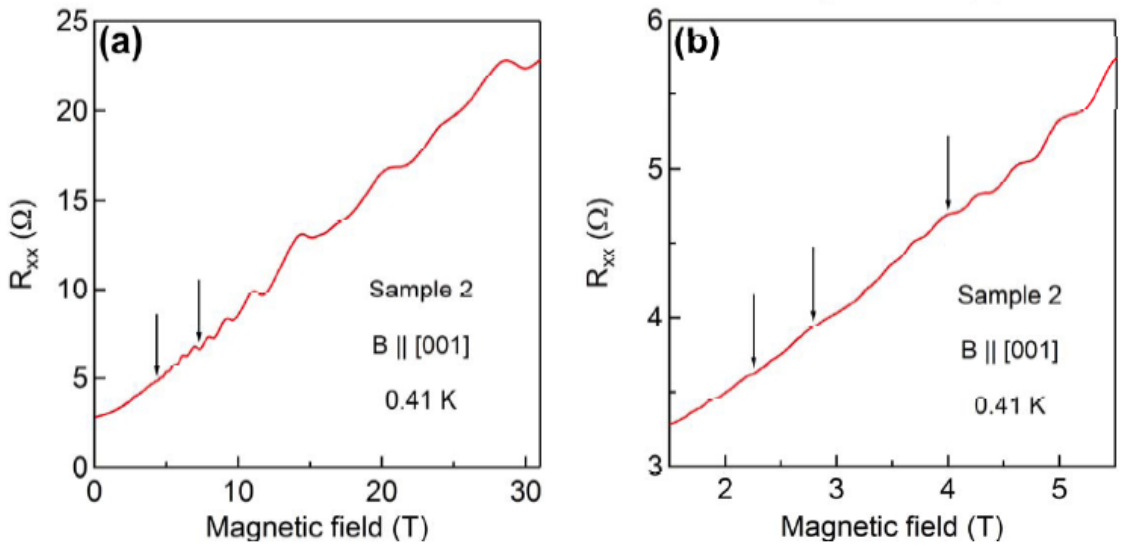

Figure 4.4: Sample 2. Shubnikov-de Haas oscillations with the magnetic field aligned along [001]. (a) Spin splitting is apparent at the highest field. At low fields a weak, low frequency oscillation is observed (arrows) and assigned to the strain induced split-off band.

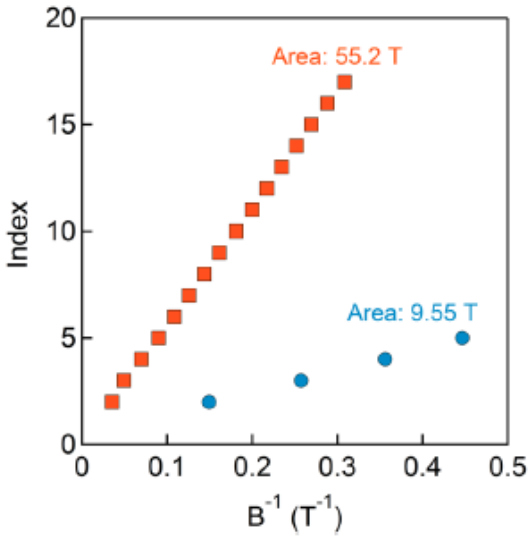

Figure 4.5: Sample 2. Indexed relative maxima for two sets of quantum oscillations in Fig. 4.4, corresponding to extremal cross sections of 55.2 and 9.55 Tesla.

areas calculated using Uwe et al.'s parameters and assuming that the tetragonal axis is normal to the surface (90° or [001]) in the figure. There is a numerical discrepancy, but the angle dependence is similar. More importantly, if we calculate the orientation dependence for a domain with the tetragonal axis in the plane, a $< 010 >$ direction, we find a qualitative difference in the angular dependence. From this we conclude that we are observing quantum oscillations only from domains with the tetragonal c-axis normal to the surface, or, alternatively, that the sample is a single domain, with tetragonal c-axis normal to the sample surface.

Shubnikov-de Haas oscillations were measured for these two samples, each in the three aforementioned orientations. This information is sufficient to determine Fermi surface shapes and consequently the low energy band parameters, subject to an

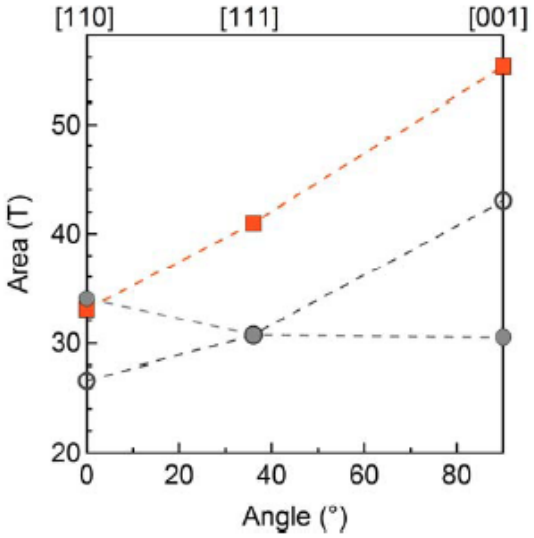

Figure 4.6: Sample 2. Angle dependence of measured extremal area, solid squares. A comparison with parameters from Uwe et al.[48] is also shown (open and closed circles, respectively). Open circles assume that the tetragonal c-axis is normal to the surface, closed circles assume the tetragonal c-axis is in the plane of the sample.

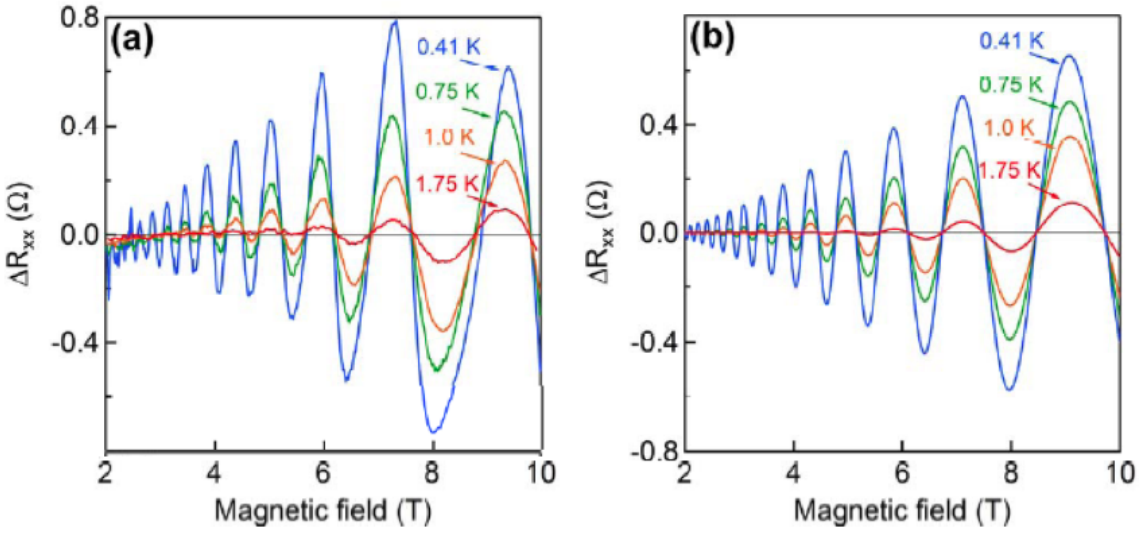

Figure 4.7: Temperature dependence of the Shubnikov-de Haas oscillations for sample 2. (a) Measured with the magnetic field along the [110] direction. (b) Model calculation with an effective mass of $1.41m_e$.

energy scale factor. To determine the energy scale factor, the temperature dependence of a set of quantum oscillations was measured and an effective mass (m^*) extracted for that extremal cross section. This is sufficient to establish an energy scale by relating the measured mass to the rate of change of the extremal cross section with energy, $\frac{\partial S_F}{\partial E} = m^* \frac{2\pi}{\hbar^2}$. Figure 4.7 shows the temperature dependence of the Shubnikov-de Haas oscillations for sample 2 with the magnetic field oriented along [110]. Also shown is a model calculation[103] that fits the measurements with an effective mass of $1.41m_e$, for this particular extremal orbit.

4.4 Analysis

The experimental data are fit to Fermi surfaces that are described by a band edge effective mass Hamiltonian subject to a large spin-orbit interaction. The key assumption is that the spin-orbit interaction is much larger than the Fermi energies at the doping levels in the samples used here and much larger than the splitting induced by the tetragonal distortion. Then we follow the model of Khalsa and MacDonald [36]. The band edge effective mass Hamiltonian in the t_{2g} basis, $\{|yz,\sigma\rangle, |zx,\sigma\rangle, |xy,\sigma\rangle\}$, is expressed as:

$$H_{\sigma,\vec{k}} = \begin{pmatrix} \epsilon_{yz} & \eta_{xy} & \eta_{zx} \\ \eta_{xy} & \epsilon_{zx} & \eta_{yz} \\ \eta_{zx} & \eta_{yz} & \epsilon_{xy} \end{pmatrix} \tag{4.1}$$

where,

$$\begin{aligned} \epsilon_{yz} &= \tfrac{1}{2}(\gamma_1 - 4\gamma_2)k_x^2 + \tfrac{1}{2}(\gamma_1 + 2\gamma_2)(k_y^2 + k_z^2) + be \\ \epsilon_{zx} &= \tfrac{1}{2}(\gamma_1 - 4\gamma_2)k_y^2 + \tfrac{1}{2}(\gamma_1 + 2\gamma_2)(k_z^2 + k_x^2) + be \\ \epsilon_{xy} &= \tfrac{1}{2}(\gamma_1 - 4\gamma_2)k_z^2 + \tfrac{1}{2}(\gamma_1 + 2\gamma_2)(k_x^2 + k_y^2) - 2be \\ \eta_{i,j} &= 3\gamma_3 k_i k_j \end{aligned} \tag{4.2}$$

Where σ is spin and $k^2 = k_x^2 + k_y^2 + k_z^2$. γ_1, γ_2, and γ_3 are closely analogous to the Luttinger[101] parameters commonly used to describe the valence band structure in elemental semiconductors. The effect of the tetragonal strain[93] is parameterized by be, following Uwe et al.'s notation where e is the tetragonal strain and b the deformation potential. In relation to Δ_T from Chapter 2, $\Delta_T = 3be$. In Eq. 4.1 k is dimensionless and equal to 1 at the zone boundary X point, π/a . The diagonal

components of (4.1) can be related to an anisotropic effective mass for each of the three t_{2g} states. If we define a heavy effective mass, m_h, and relatively lighter transverse effective mass m_t as follows $m_h = \frac{\hbar^2}{m_e}(\frac{\pi}{a})^2\frac{1}{\gamma_1-4\gamma_2}$ and $m_t = \frac{\hbar^2}{m_e}(\frac{\pi}{a})^2\frac{1}{\gamma_1+2\gamma_2}$, then the anisotropic mass for each of the three t_{2g} states can be expressed as follows. For $|yz,\sigma\rangle$ we have $m_x^{yz} = m_h$ and $m_y^{yz} = m_z^{yz} = m_t$, for $|zx,\sigma\rangle$ we have $m_y^{zx} = m_h$ and $m_z^{zx} = m_y^{zx} = m_t$, and $|xy,\sigma\rangle$ we have $m_z^{xy} = m_h$ and $m_x^{xy} = m_y^{xy} = m_t$. $\hbar$ and m_e are Planck's constant and the free electron mass.

We take the spin-orbit interaction, Δ_{SO}, to be significantly larger than the components of $H_{\sigma,\vec{k}}$. That is to say band edge in this analysis implies states with energy much smaller than Δ_{SO}. The total Hamiltonian, including spin-orbit coupling, is:

$$H_{total} = \begin{pmatrix} H_{\uparrow,\vec{k}} & 0 \\ 0 & H_{\downarrow,\vec{k}} \end{pmatrix} + \frac{\Delta_{SO}}{3}\begin{pmatrix} 1 & i & 0 & 0 & 0 & -1 \\ -i & 1 & 0 & 0 & 0 & i \\ 0 & 0 & 1 & 1 & -i & 0 \\ 0 & 0 & 1 & 1 & -i & 0 \\ 0 & 0 & i & i & 1 & 0 \\ -1 & -i & 0 & 0 & 0 & 1 \end{pmatrix} \tag{4.3}$$

To characterize the lowest lying excitations, we transform the total Hamiltonian (4.3) by forcing the diagonalization of the spin-orbit part. In this limit, the total Hamiltonian H describes the dispersion of the spin-orbit split off state and the lower band edge states. If we ignore the off-diagonal terms which couple the lower band edge states and the spin-orbit split off part separated by Δ_{SO}, we recover the dispersion of the two fold degenerate, spin-orbit split-off states, $E_{SO} = \Delta_{SO} + \frac{1}{2}\gamma_1 k^2$, and

a Hamiltonian that describes the dispersion of the remaining lowest four conduction band states, which participate in the quantum oscillations:

$$\frac{1}{2}\gamma_1 k^2 + \begin{pmatrix} \alpha_1 & \beta_1 & \beta_2 & 0 \\ \beta_1^* & \alpha_2 & 0 & \beta_2 \\ \beta_2^* & 0 & \alpha_2 & -\beta_1 \\ 0 & \beta_2^* & -\beta_1^* & \alpha_1 \end{pmatrix} \tag{4.4}$$

with

$$\begin{aligned} \alpha_1 &= \tfrac{1}{2}\gamma_2(k_x^2 + k_y^2 - 2k_z^2) - be \\ \alpha_2 &= -\tfrac{1}{2}\gamma_2(k_x^2 + k_y^2 - 2k_z^2) + be \\ \beta_1 &= \tfrac{\sqrt{3}}{2}\gamma_2(k_x^2 - k_x^2) + i\gamma_3 k_x k_y \\ \beta_2 &= \sqrt{3}\gamma_3 k_z(k_x + ik_y) \end{aligned} \tag{4.5}$$

The eigenvalues of (4.4) describe two bands, each two fold degenerate, given by the following:

$$E_\pm = \frac{1}{2}\gamma_1 k^2 \pm [\gamma_2 k^4 - 3(\gamma_2^2 - \gamma_3^2)(k_x^2 k_y^2 + k_y^2 k_z^2 + k_z^2 k_x^2) + \gamma_2 be(2k_z^2 - k_x^2 - k_y^2) + (be)^2]^{1/2} \tag{4.6}$$

This is identical to the expression used by Uwe et al.[48] but expressed in terms of the Luttinger parameters. We note that if we restrict our measurements to energies much less than the spin-orbit splitting, the results are not influenced by the strength of the spin-orbit interaction and we determine the parameters for $H_{\sigma,\vec{k}}$ in Eq. (4.1).

Parameter	Experiment (this study) (4-band) (eV)	Experiment (this study) (6-band) (eV)	Experiment (Uwe et al. [48, 49]) (eV)	Bandstructure calculation (Janotti et al.[41]) (eV)
γ_1	4.0($\pm$0.04)	3.34	3.5	8.81
γ_2	0.98($\pm$0.02)	0.66	0.88	1.92
$\gamma_1 + 2\gamma_2$	6.0	4.67	5.26	12.65
$\gamma_1 - 4\gamma_2$	0($\pm$0.1)	0.69	0.0	1.15
γ_3	0.0($\pm$0.02)	0.0	0.13	0.78
$2be$	-2.2×10^{-3}	-3.2×10^{-3}	-1.5×10^{-3}	-2.268×10^{-3}
M ($1/m_0$)	1/0.83	1/1.06		
L ($1/m_0$)	$\sim$1/62	1/7.16		

Table 4.2: Conduction band parameters determined in this study and comparison with the literature.

As is the case for the valence band of elemental and compound semiconductors, the complex dispersion relation will lead to a complex spin-Landau spectrum especially at high magnetic fields. Indeed, at the highest fields the quantum oscillations begin to resolve spin dependent Fermi surfaces. The extremal areas measured at the prescribed angles for the two samples were simultaneously fit, using a non-linear algorithm, to the dispersion relation (4.6) by adjusting the following dimensionless parameters: γ_2/γ_1, γ_3/γ_1, $E_{F,1}/\gamma_1$, $E_{F,2}/\gamma_1$, and $be/\gamma 1$. These parameters, as ratios, determine the size and shape of the measured Fermi surfaces but not the energy scale; the size and shape of the various extremal areas are independent of γ_1. By adjusting γ_1, we can fit the mass determined by the temperature dependence of the Shubnikov-de Haas oscillations. The fitting parameters are then expressed in appropriate energy units.

Table 4.2 shows the parameters that were determined from these fits. Satisfac-

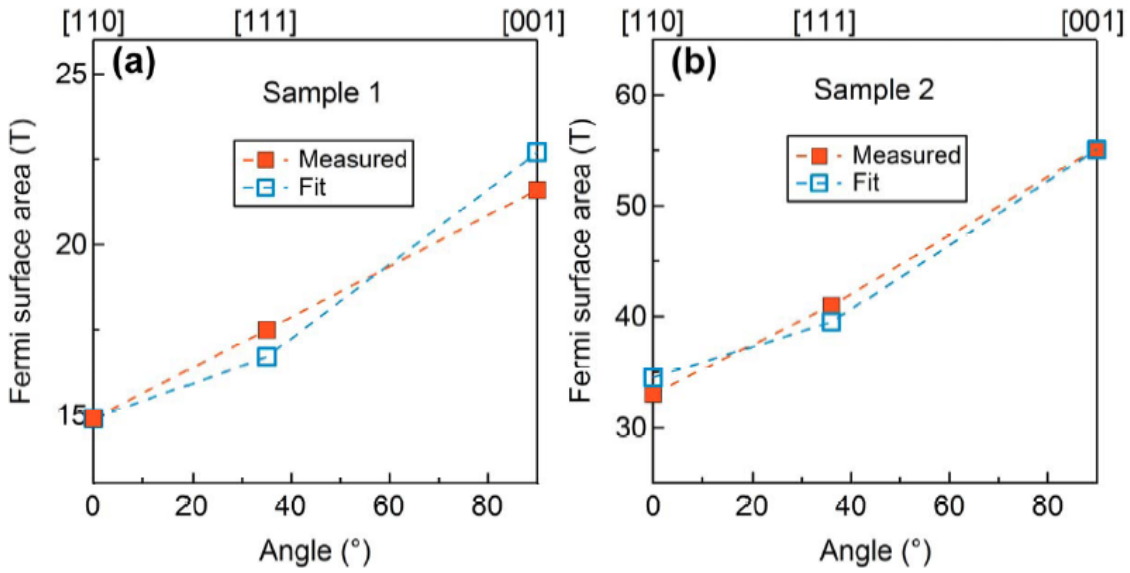

Figure 4.8: Fermi surface area versus angle, measured (solid) and fit (open), using the parameters in the text.

tory agreement between the measured and calculated angular dependence using the parameters in Table 4.2, is shown in Fig. 4.8. Not shown in Fig. 4.8 is the agreement achieved by the fit for the narrow waist of the Fermi surface that originates from strain split off band; the measured 9.55 Tesla compares well with a fit value of 9.47 Tesla. A more complete low energy model that includes the spin-orbit split off band causes a small change in the Luttinger parameters (See Table 4.2 (6-band)).

Apart from this differences, the results essentially agree with the earlier results of Uwe et al.[48] The discrepancies may reflect the fact that the earlier work by them was carried out at higher electron densities and was extracted by disentangling orbits that suffered magnetic breakdown. The discrepancy between the Shubnikov-de Haas and Hall densities in the two samples used in this analysis may be due to the moderate

complexity of the Fermi surface in this density range.

Various band structure calculations predict Luttinger parameters that are substantially larger than those measured by Shubnikov-de Haas oscillations shown in Table 4.2 [41, 64]. In particular we compare with a recent ab initio band structure calculation by Janotti et al.[41] and conclude that the SdH mass is ~ 2 times heavier than predicted. We can ascribe this discrepancy to strong electron phonon coupling[104] only if we accept at face value the ab initio band structure calculations. A phonon enhancement of $\sim 2-3$ was implied in recent infrared measurements of the extended Drude response [105].

We also note that the parameters imply a vanishingly small dispersion, $\gamma_1 - 4\gamma_2 \propto 0$, and as a result, a very large heavy mass, m_h . As pointed out by Janotti et al. [41], the spin orbit coupling admixes the three t_{2g} states and the dispersion at the band edge (See Fig. 4.1.) does not show the extreme anisotropy displayed in equation (4.1) and measured here. However, models of electric subbands in $SrTiO_3$ with extremely high electron densities involve large $\vec{k}$ vectors due to relatively large in plane Fermi energies and tight quantum confinement. Then, models of these quantum confined states are best developed with the extreme anisotropy of equation (4.1), introducing the spin orbit interaction after electric surface quantization.

4.5 Summary

Low temperature Shubnikov-de Haas effect measured on high mobility but low density La doped $SrTiO_3$ samples was used to determine the tetragonally induced band edge spitting and low energy Luttinger band edge parameters. The work

substantially agrees with Uwe et al.[48] The band edge Luttinger parameters differ substantially from those predicted by *ab initio* calculations and require an examination of the calculated band structure and/or mass enhancement by electron phonon coupling. Similar experiments in higher carrier density samples could potentially provide an independent measurement of the spin-orbit interaction strength.

Chapter 5

Theory of the $SrTiO_3$ Surface State Two-Dimensional Electron Gas

In this chapter we present a theory of the quasi-two-dimensional electron gas (2DEG) systems that appear near the surface of $SrTiO_3$ (and $KTaO_3$) when a large external electric field attracts carriers to the surface. This model is informed by the results of the previous chapters significantly - in particular Chapters 2 and 4. The most notable necessary addition to understanding confinement effects in d^0 perovskites appears to be the novel large lattice mediated dielectric response. To this end, we find that nonlinear and nonlocal screening by the strongly polarizable $SrTiO_3$ lattice plays an essential role in determining 2DEG properties. The electronic structure always includes weakly bound bulk-like bands that extend over many $SrTiO_3$ layers. At 2D carrier densities exceeding $\sim 10^{14} cm^{-2}$, tightly bound bands emerge that are confined within a few layers of the surface.

5.1 Introduction

Two-dimensional electron gases can be formed in $SrTiO_3$ crystals[17, 62, 88, 106] by gating [26–28], by forming an interface with a polar perovskite [17, 60, 62, 88, 90, 100, 107, 108], or by placing a δ-doped[20–23] layer inside a bulk crystal. Al-

though 2D electronic systems at $LaAlO_3/SrTiO_3$ interfaces have received particular attention [60, 90, 100, 107, 108], there has also been important progress with other material systems [3, 18, 19, 24, 25, 109, 110]. $SrTiO_3$ two-dimensional electron gases (2DEGs) appear to be strongly correlated when their thermodynamics is probed capacitively[111] and exhibit both superconductivity[30] and magnetism [59], sometimes simultaneously [31, 32, 34, 35]. There is at present only a very primitive understanding of the measured properties of these potentially interesting 2DEG systems. This chapter is motivated by the view that progress can be accelerated by the development of concrete microscopic models that are simplified relative to full *ab-initio* electronic structure calculations [37, 112–120], allowing electric properties to be estimated easily and compared with experiment.

In this chapter a model of $SrTiO_3$ 2DEGs that is partly phenomenological and simplified, but still sufficiently realistic to be predictive is presented. We focus on electrostatically gated surface 2DEGs, although our approach applies without much change to the case of interface-confined systems. The same model is readily adapted to describe δ-doped 2DEGs inside the STO bulk, STO 2DEGs that are modulated by a back gate, and 2DEGs in other d^0 systems, for example $KTaO_3$. The model assumes that the itinerant electronic degrees of freedom are derived from the $SrTiO_3$ t_{2g} bands. We use a nearest neighbor tight-binding model to describe hopping between TiO_2 planes and either tight-binding or $\vec{k}\cdot\vec{p}$ models to describe wavefunction variation within TiO_2 planes. The strength of inter-plane hopping parameters, and the values of the heavy and light masses within planes are estimated on the basis of recent ARPES[51, 72] and bulk magnetic oscillation[56] experimental results. Some aspects

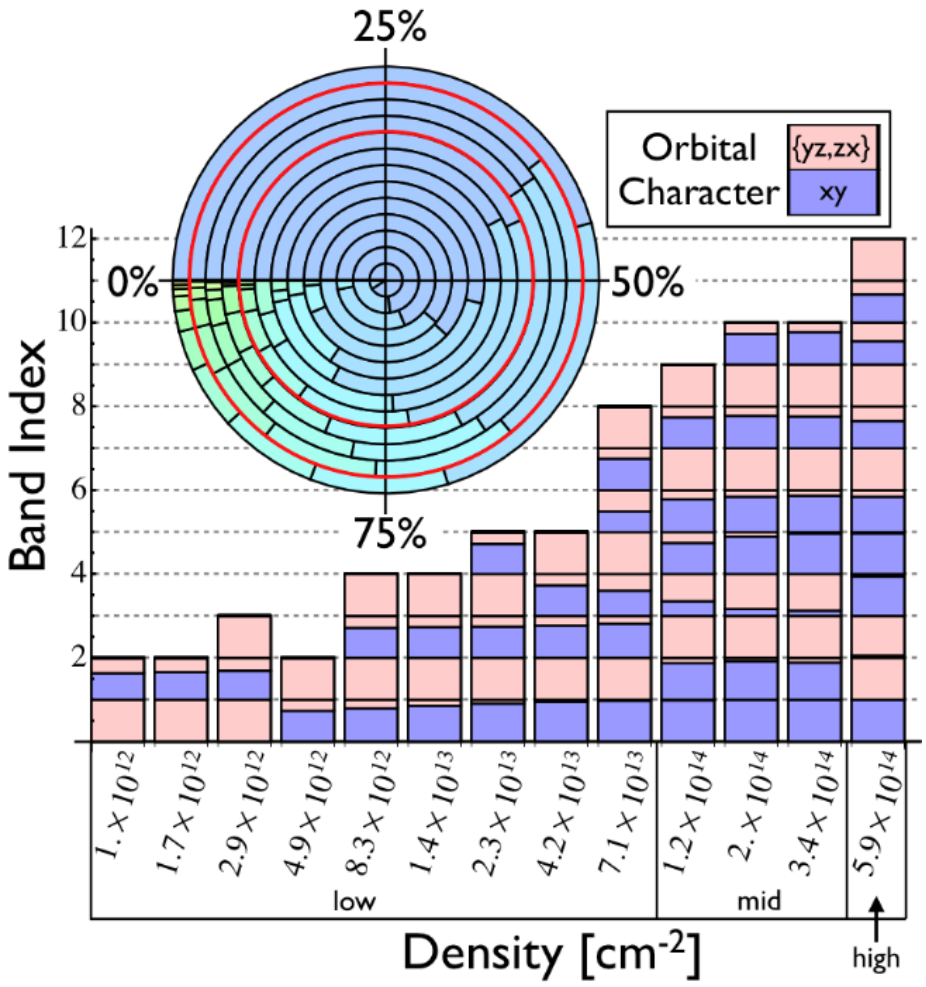

Figure 5.1: Orbital character at $k_\perp = 0$ of occupied doubly degenerate 2D subbands for a series of total areal densities. The xy and $\{yz, zx\}$ fractions in the orbital character of each band are represented by light blue and light red shading respectively and the band indices are ordered from lowest energy to highest. Both spin-orbit interactions and tetragonal splitting have been included in the band-structure model. The percentage of the total density associated with a given subband is summarized in the inset piechart, in which the rings from inside to outside correspond to the density values from lowest to highest. Individual band contributions for a particular density are ordered lowest energy to highest in a clockwise direction. The red lines in the pie chart separate the low, mid, and high density regimes identified in the text. At the highest total densities, most electrons occupy a small number of strongly confined bands.

of the 2DEG electronic structure are sensitive to the influences of spin-orbit coupling and $SrTiO_3$'s low-temperature tetragonal distortion on the host material's conduction band, even at the highest 2D carrier densities.

The extremely strong dielectric response of the $SrTiO_3$ lattice plays a key role in our model at all carrier densities. Our main results are summarized in Fig. 5.1. We find that unless vertically confined on both sides by vacuum or insulating tunnel barriers, $SrTiO_3$ 2DEGs spread across a large number of TiO_2 planes. This property is a direct consequence of the host material's very large linear dielectric constant, which weakens confinement, and occurs in spite of relatively large carrier masses which favor confinement. At high carrier densities, and hence large electric fields, dielectric screening saturates and the 2DEG is mostly confined to the first few TiO_2 planes. However a portion of the 2DEG, making a contribution to the 2D density that is approximately fixed in absolute terms, still spills over many layers. This low-density weakly confined part of the 2DEG can make an important contribution to some 2DEG properties.

This chapter is organized as follows. In the following section we provide a detailed explanation of the model that we use. We have identified three different density regimes for $SrTiO_3$ surface-bound 2DEGs. In Secs. 5.3, 5.4, and 5.5 we characterize the nature of the 2DEG electronic structure in low ($n < 1 \times 10^{14}\text{cm}^{-2}$), mid ($1 \times 10^{14}\text{cm}^{-2} < n < 5 \times 10^{14}\text{cm}^{-2}$), and high ($n > 5 \times 10^{14}\text{cm}^{-2}$) 2DEG carrier density regimes respectively. Finally in Sec. 5.6 we summarize our results and speculate on the types of electronic properties that might be achievable in $SrTiO_3$ 2DEG systems.

5.2 Model

5.2.1 t_{2g} tight-binding model

The starting point for any phenomenological description of the electronic structure of $SrTiO_3$ 2DEGs is an accurate representation of the bulk material electronic structure. Although this material has been studied for many years, its conduction band minimum was until recently not characterized with an accuracy sufficient to model low-carrier density 2DEGs. To remedy this, Allen *et al.* conducted[56] magnetotransport studies on a series of low density electron-doped MBE-grown samples of $SrTiO_3$ in fields up to 31T and fit a 6 band $\mathbf{k} \cdot \mathbf{p}$ model of the Ti t_{2g} bands to the magnetic oscillation data. The bulk band parameters used here have been taken from that study. These experiments suggest that in the absence of spin-orbit coupling the tetragonal distortion at 4 K would push the xy bands up by ~ 3.2 meV relative to yz and zx bands. (The band parameters used are the result of the six band fit from Chapter 4. The 4 band fit described in that chapter leads to only quantitative differences in the confined electronic structure.) Together the two-corrections fully lift the t_{2g} manifold degeneracy, even in the bulk. (Because of orbital mixing, the spin-orbit (SO) splitting and tetragonal splitting parameters do not directly correspond to the Γ point band energies.)

Although the $p-d$ oxygen bonding and e_g anti-bonding orbitals do not explicitly enter our model, they do appear implicitly in the form of the Hamiltonian. Consider for example hopping between a Ti xy orbital and its neighboring oxygens within a TiO_2 plane (Fig. 5.2a). Along the x-direction, the dominant bonding is π_{pd} through the O-p_y orbital and along the y-direction, π_{pd} through the O-p_x or-

bital. Overlap with other O-p orbitals is small by symmetry. This rule is preserved througout the Ti - O -Ti bonding network. For the Ti - yz orbital, π_{pd} bonding dominates along the y-direction through O-p_z orbitals. Bonding along the x-direction vanishes in a Slater-Koster two-center approximation and is weak. Temporarily ignoring the spin-orbit and tetragonal distortion effects, these observations suggests a tight binding model for a single isolated layer of the form

$$H_{\sigma}^{SL} =. \begin{pmatrix} -2t'cos(k_x) - 2tcos(k_y) & 0 & 0 \\ 0 & -2tcos(k_x) - 2t'cos(k_y) & 0 \\ 0 & 0 & -2tcos(k_x) - 2tcos(k_y) \end{pmatrix} \tag{5.1}$$

writen in the $\{yz, zx, xy\}$ basis. In the above equation, the cubic lattice constant is used as a length unit, the metal lattice site energies are used as the zero-of-energy, t quantifies the dominant π_{pd} bonding process and t' describes the weaker bonding process. Hopping terms that couple different t_{2g} orbitals are allowed[50] (See for example Eq. 2.10) from a symmetry point of view. However, Allen *et al.* were unable to distinguish this mixing parameter from zero in their recent analysis of SdH data [56]. We therefore ignore these processes in our model. For lower carrier densities it is sometimes convenient to use a simplified version of this model in which we expand Eq. 5.1 around the 2D Γ point. We find that for 2D wavevectors that are small compared to Brillouin-zone dimensions

$$H_{\sigma}^{SL} = \begin{pmatrix} \epsilon_{yz,0} + t'k_x^2 + tk_y^2 & 0 & 0 \\ 0 & \epsilon_{zx,0} + tk_x^2 + t'k_y^2 & 0 \\ 0 & 0 & \epsilon_{xy,0} + tk_x^2 + tk_y^2 \end{pmatrix} \begin{Bmatrix} yz, \sigma \\ zx, \sigma \\ xy, \sigma \end{Bmatrix}, \tag{5.2}$$

where $\epsilon_{yz,0} = \epsilon_{zx,0} = -2t - 2t'$ and $\epsilon_{xy,0} = -4t$. We use this low density form for the planar Hamiltonian for most of the calculations presented below. The more general tight-binding model must be used when 2D carrier densities are large and confinement is strong, and can be adopted when required without essential complication.

In the same representation, adjacent 2D layers are coupled by an interlayer hopping term of the form

$$H_\sigma^C = \begin{pmatrix} t & 0 & 0 \\ 0 & t & 0 \\ 0 & 0 & t' \end{pmatrix} \begin{Bmatrix} yz, \sigma \\ zx, \sigma \\ xy, \sigma \end{Bmatrix} . \tag{5.3}$$

Here the symmetry of the bonding network has again been employed to note that the xy orbital has the weaker interlayer coupling, t'. Because t' is expected to be substantially smaller than t, the xy bands in single-layer 2DEGs are pulled down by $\sim 2t$ at the Γ point relative to the yz and zx bands. In the bulk limit, on the other hand, the three bands are degenerate because each has two strong hopping and one weak hopping direction. Any amount of confinement in the $\hat{z}$ direction pushes the bottom of the $\{yz, zx\}$ bands up relative to the xy band and leads to orbital polarization.

For low-carrier densities on-site ($\boldsymbol{k}$-independent) terms due to tetragonal distortions and spin-orbit coupling must be included [50]. The tetragaonal distortion is represented by a parameter Δ_T which characterizes the difference in site energy between xy and $\{yz, zx\}$-orbitals, and spin-orbit coupling by an interaction strength parameter Δ_{SO}. The distortion Hamiltonian is

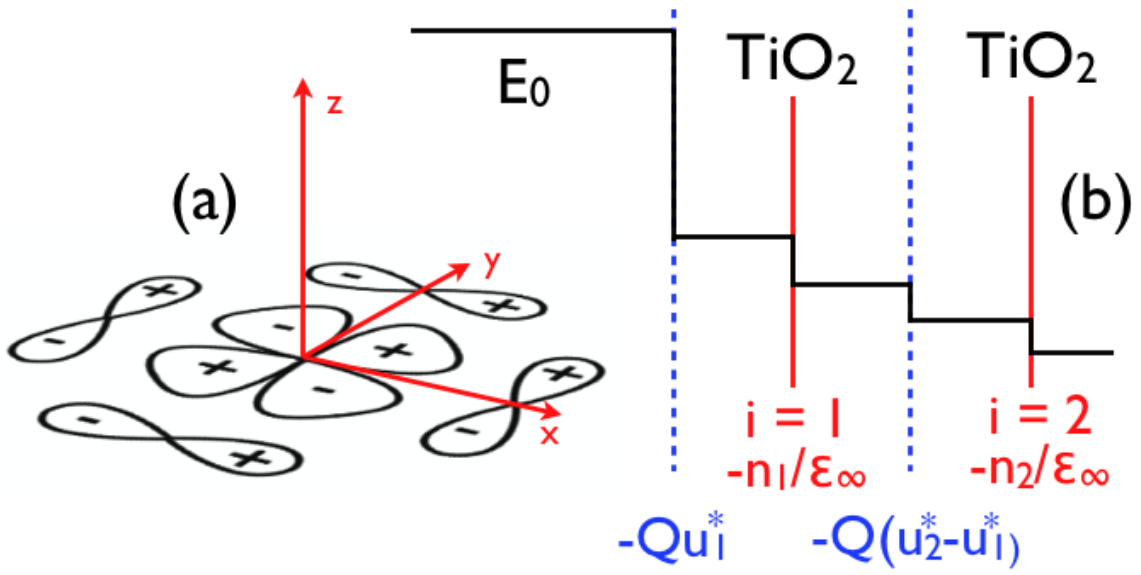

Figure 5.2: (a) $p-d$ bonding network for Ti-xy orbital. The dominant bonding is in-plane π_{pd} while the out-of-plane bonding is weak. (b) Schematic representation of the electric field drop in our model due to lattice screening (dashed blue) and electronic screening (solid red). Numerical factors have been dropped.

$$T_\sigma = \begin{pmatrix} 0 & 0 & 0 \\ 0 & 0 & 0 \\ 0 & 0 & \Delta_T \end{pmatrix} \begin{Bmatrix} yz,\sigma \\ zx,\sigma \\ xy,\sigma \end{Bmatrix}, \tag{5.4}$$

and the spin-orbit Hamiltonian, modeled in an atomic approximation, is

$$H^{SO} = \frac{\Delta_{SO}}{3} \begin{pmatrix} 0 & i & 0 & 0 & 0 & -1 \\ -i & 0 & 0 & 0 & 0 & i \\ 0 & 0 & 0 & 1 & -i & 0 \\ 0 & 0 & 1 & 0 & -i & 0 \\ 0 & 0 & i & i & 0 & 0 \\ -1 & -i & 0 & 0 & 0 & 0 \end{pmatrix} \begin{Bmatrix} yz,\uparrow \\ zx,\uparrow \\ xy,\uparrow \\ yz,\downarrow \\ zx,\downarrow \\ xy,\downarrow \end{Bmatrix}. \tag{5.5}$$

Our model for the electronic structure of $SrTiO_3$ 2DEGs combines the single-

particle model explained above with a Hartree approximation for electron-electron interactions. The external electric field which produces surface confinement is screened by carriers and by lattice relaxations of the partially ionic $SrTiO_3$ crystal. In $SrTiO_3$ lattice screening is strong and non-linear and plays a subtle and essential role in confinement.

5.2.2 Lattice relaxation model

The exceptionally strong and temperature-dependent linear dielectric response of bulk $SrTiO_3$ is associated with a soft optical phonon mode in which positively charged Sr and Ti atoms move in opposition to the negatively charged oxygen octahedra. Displacement of this mode in response to an external electric field produces screening. Because the mode is extremely soft only near the center of the Brillouin-zone [53], it responds strongly only when a large external field persists over several TiO_2 layers. In addition this screening response is very non-linear, saturating at very large electric fields. Since the reduction in electric field is proportional to the phonon mode displacement, saturation occurs because the phonon mode is anomalously soft only for small displacements [53]. In an attempt to capture this behavior qualitatively, we use a simple model of lattice relaxation which focuses on the soft-mode only. We write the lattice energy as

$$U = \frac{1}{2}\sum_{i,j} u_i K_{i,j} u_j - Q\sum_i E_i u_i + \frac{\gamma}{4}\sum_i u_i^4 \tag{5.6}$$

where u_i is the displacement of the soft-mode on the i-th lattice site, E_i is the average electric field in the i^{th} cell, Q is an effective charge defined in terms of the polarization-

density per unit soft-mode displacement, and γ is a parameter chosen to capture the non-linearity of the dielectric response as discussed further below. Here $K_{i,j} = K_{i-j}$ is the dynamical matrix at 2D wavevector $\boldsymbol{q}_\perp = 0$. We fit K_{ij} to the soft-mode phonon dispersion using a form with a local on-site contribution and a Gaussian non-local contribution. In momentum space, this takes the form,

$$K(q,G) = (2\pi)^2\mu\left[f_0^2 - f_1^2 e^{-\frac{\alpha_1^2}{2}(q+G)^2} - f_2^2 e^{-\frac{\alpha_2^2}{2}(q+G)^2}\right] \tag{5.7}$$

where q is the lattice momentum, G is a reciprocal lattice vector, and $\mu = 24amu$ is the appropriate reduced mass for the Ti atom moving opposite the oxygen octahedra. The parameters f_0, the strength of the on-site term, and f_1 and α_1 were chosen to reproduce the measured phonon dispersion. Because no low temperature phonon data exists in the literature, f_2 and α_2 have been added to capture the low temperature dielectric response of the bulk material. By minimizing Eq. 5.6 in the absence of an electric field and evaluating Eq. 5.7 at $q = 0$ we find that

$$\gamma = \left[\frac{2\pi(f_0 - f_1 - f_2)}{u_{NL}}\right]^2 \tag{5.8}$$

where u_{NL} is the mode displacement at which non-linear dielectric response is seen. (See the discussion below).

Because the relative displacements of all atoms are known, only a single displacement coordinate, u_i, is needed to describe the response of the unit cell to perturbations along the principle crystal axes. Given the electric field in each cell of the crystal, Eq. 5.6 can be minimized to find the appropriate set of displacements, $\{u_i^*\}$. We define the three-dimensional polarization density of the $SrTiO_3$ as

$$P_i = \frac{1}{a^3} Q u_i^* \left[\Theta(z_i - a/2) - \Theta(z_i + a/2)\right] \tag{5.9}$$

where z_i is the location of the TiO_2 layer of interest, a is the lattice constant of the crystal, and $\Theta(z)$ in the Heaviside function. The precise way in which the polarization density is mapped onto our lattice model is immaterial on length scales larger than a lattice constant. To find the effective charge parameter we use the standard definition of the screened electric field and linear dielectric constant,

$$E = E_0 + 4\pi P \approx \epsilon E_0. \tag{5.10}$$

After minimizing Eq. 5.6 in the linear, bulk limit and using the definition of the polarization from Eq. 5.9, we find that,

$$Q = \sqrt{\frac{\mu\omega_1^2}{4\pi}(\epsilon - 1)}. \tag{5.11}$$

To make contact with the measured properties of the bulk material in a straightforward way, we use $90K$ values for the phonon dispersion [53] and dielectric constant [52]. In terms of model parameters $\omega_1 = 2\pi(f_0 - f_1)$ and the $90K$ dielectric constant are given in Table 5.2.3. With this we find $Q = 8.33e$, a value comparable to those used in models of this type for bulk $SrTiO_3$ [53].

The electric field in Eq. 5.6 can be found by solving

$$\nabla \cdot E(z) = -\frac{4\pi e}{\epsilon_\infty} \sum_i n_i \delta(z - z_i) + 4\pi \sum_i \nabla \cdot P_i, \tag{5.12}$$

with the boundary conditions that $E(-\infty) = E_0$ and $E_\infty = 0$. The electric field boundary conditions are discussed below. In Eq. 5.12, e is the electron charge, ϵ_∞ is the high frequency dielectric constant due to electronic screening, and n_i is the number density of itinerant electrons in TiO_2 layer i. Both lattice relaxation and conduction band charge accumulation screen the external electric field. This is represented pictorially in Fig. 5.2b.

5.2.3 Electric Field Boundary Conditions

In the calculations presented below we assume that the electric field above the surface of the $SrTiO_3$ has been set experimentally either by gating or by forming an interface with a polar dielectric [121]. In the latter case E_0 is ideally set by the polarity of the material, but can also be influenced by surface reconstructions or other detailed material considerations that can be sensitive to uncontrolled aspects of growth. Because we have gated systems in mind, we consider that E_0 can be varied experimentally over a broad range. In this calculation we set the electric field below the $SrTiO_3$ 2DEG, E_{bulk}, to zero, assuming that the sample lies on a grounded metallic substrate. (If the $SrTiO_3$ sample was thin, a conducting layer under the sample could be used as a gate and E_{bulk} could be varied.) By integrating the Poisson equation (Eq. 5.12) and noting that the lattice relaxation contribution to $E(z)$ vanishes far below the surface when $E_{bulk} \to 0$, we conclude that the 2DEG density is fixed by E_0 alone: $n_T = \sum_i n_i = \epsilon_\infty E_0 / 4\pi e$. We can therefore replace this parameter by the total 2DEG density n_T and present results as a function of that parameter.

We incorporate the layer-dependent electric potential contribution to the Hamil-

tonian by integrating $E(z)$ across the 2DEG to obtain a layer-dependent potential V_i which must be determined self-consistently along with the 2DEG density-distribution and the soft-mode displacement field. With this, the Hamiltonian of the system becomes,

$$H = \sum_{<i,j>} \vec{c}_i{}^{\,\dagger} H^C \vec{c}_j + \sum_i \vec{c}_i^{\,\dagger} \left(H^{SL} + T + H^{SO} + V_i \right) \vec{c}_i \tag{5.13}$$

where the double sum in the first term is over neighboring layers. In Eq. 5.13, we work in the representation $\vec{c} = \{c_{xy,\uparrow}, c_{yz,\uparrow}, c_{zx,\uparrow}, c_{xy,\downarrow}, c_{yz,\downarrow}, c_{zx,\downarrow}\}$ so that H^{SO} has the form of Eq. 5.5.

The layer resolved density $n_i =< \vec{c}_i^{\dagger} \vec{c}_i >$ is calculated from Eqs. (5.12,5.13) and minimization of Eq. 5.6. We have carried these self-consistent field calculations to convergence over a wide range of densities for a system that is 60 unit cells wide. Because of the long tail in the density-distribution discussed at length below, it is difficult to achieve self-consistency and we were forced to mix in no more than $\sim 1\%$ of new results in the iterative update of the charge density. Although the model described in this section is crude in some respects, certainly crude compared to *ab initio* electronic structure calculations with full lattice relaxation, it is strongly motivated by the cumbersome character of the fully microscopic calculations under these circumstances. The model could be made more quantitative by being bench-marked against *ab initio* calculations or, perhaps more reliably, by comparison with experiment.

Model Parameters		
Lattice Constant	a	3.904 Å
Electronic Parameters	t	$236meV$
	t'	$35meV$
	Δ_{SO}	$18meV$
	Δ_T	$3.2meV$
Dielectric Response	ϵ_0	24408
	ϵ_1	1340
	ϵ_∞	5.5
	Q	$8.33e$
	u_{NL}	0.0034Å
Dynamical Matrix	f_0	$4 \times 10^{12} c/s$
	f_1	$2.73 \times 10^{12} c/s$
	f_2	$0.97 \times 10^{12} c/s$
	α_1	$1.15a$
	α_2	$5a$

Table 5.1: Parameters used in the current study. The electronic structure parameters have been taken from Ref. [56], while ϵ_∞, ϵ_1 and ϵ_0 were taken from Refs. [53] & [52].

5.3 Low Carrier Densities $1 \times 10^{14}\mathrm{cm}^{-2} < n_T$

For the circumstance considered here the total carrier density is proportional to the electric field just above the $SrTiO_3$ surface and the largest internal electric fields are closest to the surface. We define the low-density regime by the requirement that the largest electric fields are smaller than the scale at which non-linear screening becomes important. This field scale is set by the model parameters u_{NL} and ϵ_∞, which can be determined approximately from experiment. We have estimated u_{NL} by comparing Eq. 5.9 with the deviation from linear response seen in the polarization of bulk STO crystals [52]. This value is listed along with other model parameters in Table 5.2.3. The model parameters we have chosen reflect the estimate that non-linear screening becomes important for carrier densities larger than $\sim 1 \times 10^{14} cm^{-2}$.

For linear screening some 2DEG properties are similar to those of covalent semiconductor 2DEGs and can be estimated following the same lines as in Stern's pioneering study of Si/SiO_2 MOSFET 2DEGs [122]. In particular the confinement length scale w can be crudely estimated by equating the quantum confinement kinetic energy cost and the confinement electric potential scale. Neglecting numerical factors we therefore set

$$\frac{\hbar^2}{mw^2} \sim \frac{eE_0 w}{\epsilon} \sim \frac{4\pi e^2 n_T w}{\epsilon} \tag{5.14}$$

to obtain

$$w \sim \Big(\frac{\hbar^2 \epsilon}{4\pi m e^2 n_T}\Big)^{1/3}. \tag{5.15}$$

In the linear screening regime the confinement length scale decreases quite slowly with the total 2DEG density. The hopping parameters of Table 5.2.3 can be con-

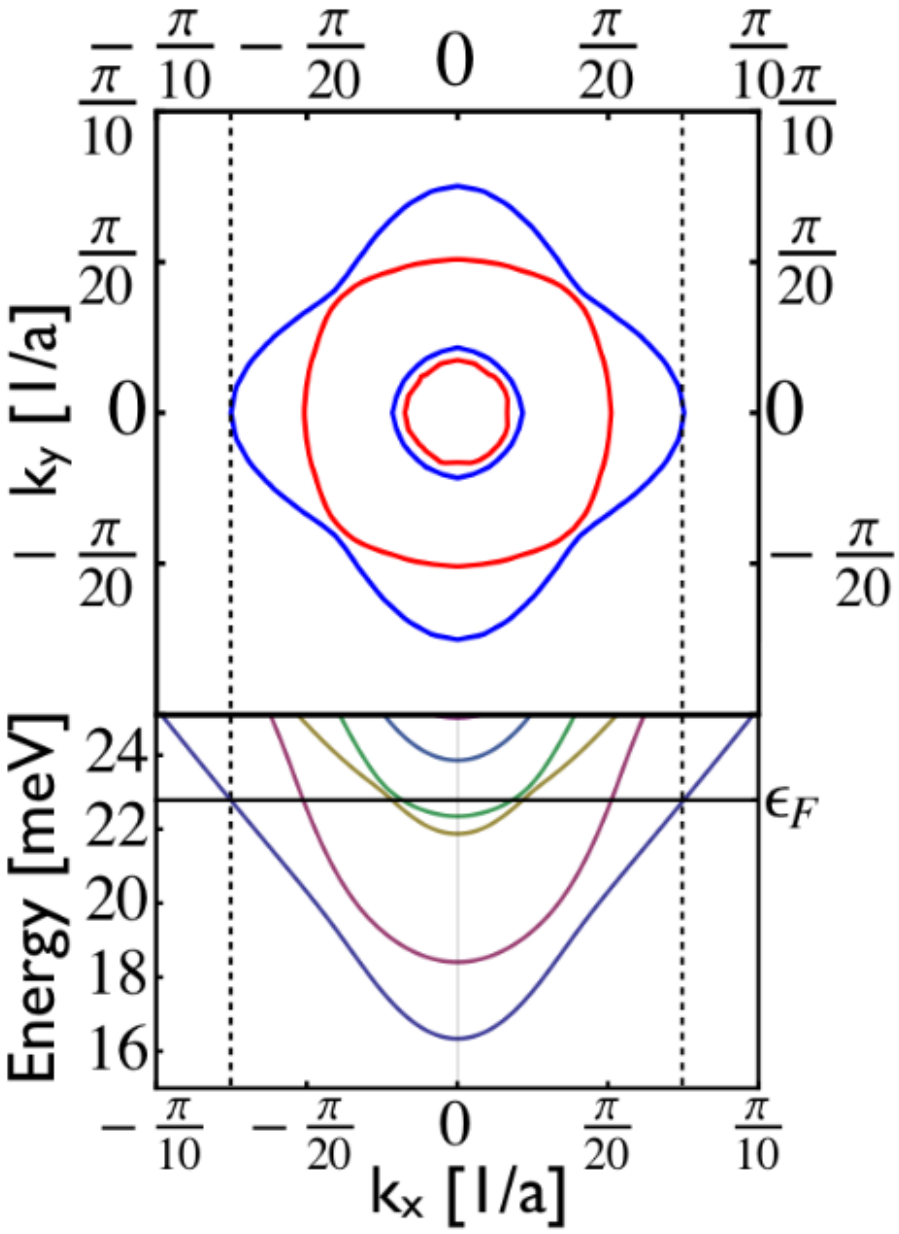

Figure 5.3: (a) Fermi surface and 2D band structure for $n_T = 8.3 \times 10^{12}$. The dominant orbital character at the 2D Γ point is represented for each band by the color of the bands and Fermi lines - blue and red for xy and $\{yz, zx\}$, respectively. The zero of energy is set to the potential minimum in the first layer. The Fermi energy is indicated by a solid (black) horizontal line.

verted to effective masses for the t_{2g} bands; the light mass that describes the vertical confinement of the most poorly confined $\{yz, zx\}$ bands is $\sim m_0$ where m_0 is the bare electron mass. When combined with the extremely large low-temperature bulk dielectric constant of $SrTiO_3$ ($\epsilon \sim 25000$), we estimate that w is close ~ 50 $SrTiO_3$ unit cells even at the top end of the low-density regime. We therefore expect that the hard wall at 60 unit cells used in our calculations influences our numerical results. The main point of these qualitative considerations is that we should expect weak surface confinement at low carrier densities because of very strong dielectric screening.

In Figs. 5.3 we illustrate a typical 2D band structure in the low density regime. Here the bottom band is beginning to reflect the increase in xy character expected from confinement, and the small size of the subband splittings is in qualitative agreement with the estimated scale of size-quantization energies:

$$\frac{\hbar^2}{mw^2} \sim 10^{-4}\,\mathrm{eV}. \tag{5.16}$$

The small subband splittings imply that the 2DEG is 3D in character unless temperatures are low and disorder extremely weak. The vertical spread of the 2DEG is expected to get smaller, and the subband splitting larger with increasing temperature as the dielectric constant value decreases [52].

Low carrier density properties are strongly influenced by spin-orbit coupling which hybridizes the t_{2g} basis states and induces a splitting at the Γ point in the bulk. One effect of spin-orbit coupling is to weaken the 2DEG surface confinement by hybridizing xy bands with yz and zx bands that have smaller masses perpendicular to the surface. Spin-orbit induced hybridization allows the xy subbands to communicate

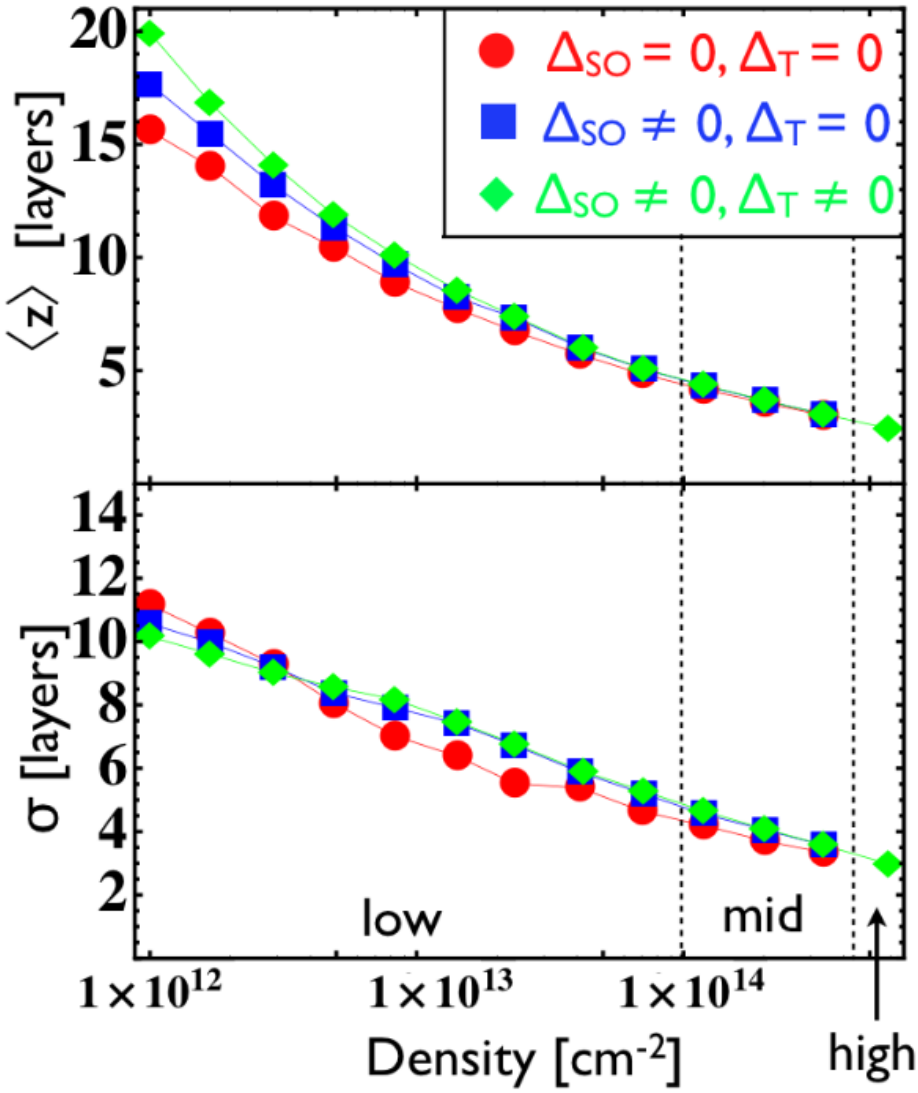

Figure 5.4: Average separation from surface, $\langle z \rangle$ and standard deviation σ of the electron distribution across layers as a function of total density, and its dependence on SO splitting and the tetragonal distortion. The tendency of SO coupling and tetragonal splitting to weaken surface confinement is suppressed when densities reach the mid range. When confinement energy scales are not strong enough to overcome the tetragonal distortion, SO and tetragonal-splitting induced hybridization decrease the spread of the $\{yz, zx\}$ bands (see text).

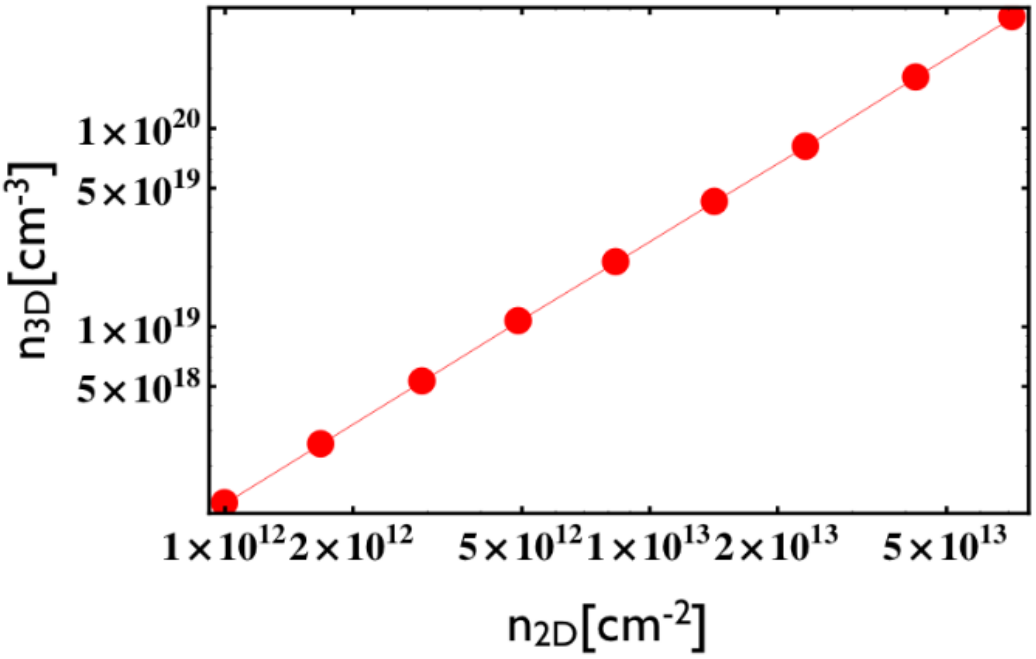

Figure 5.5: Calculated 3D density in the low density regime. The relationship between 2D density and average 3D density follows a 4/3 power law that is consistent with Eq. 5.14 is correct.

between layers through their $\{yz, zx\}$ admixtures which are less easily confined. In the low density regime, spin-orbit splitting is pronounced enough to change the dominant orbital character of the 2D subbands.

The tetragonal distortion increases the site energy of the xy band - further enhancing the role of the less confined $\{yz, zx\}$ components. (We have assumed that the tetragonal axis is parallel to the surface normal, as expected near a surface.) Initially, confinement energy scales are weak compared to the tetragonal splitting energy. As the carrier density and the energetic width of the occupied states increase, spin-orbit coupling becomes less important and the xy fraction of the lowest energy most highly occupied band increases. (See Fig. 5.1.) The influence of the spin-orbit and tetragonal splittings on the spatial distribution of electrons is summarized in Fig. 5.4. Estimating 3D densities using $n_{3D} = n_{2D}/\langle z \rangle$ where $\langle z \rangle$ is taken from Fig. 5.4 and n_{2D} is the total density in the linear screening spatial region, we find a power law of 4/3. This suggests that the qualitative estimate of Eq. 5.14 is accurate when screening is linear.

5.4 Mid-range densities: $1 \times 10^{14}\text{cm}^{-2} < n < 5 \times 10^{14}\text{cm}^2$

We define the mid-range of densities as that in which lattice screening is markedly reduced because of non-linear dielectric screening (see Fig. 5.6.) Because the electric field is larger closer to the surface, non-linear screening is more important there. The strong surface electric fields cause a large fraction of the total electron density be confined close to the surface, and size-quantization effects to increase much more rapidly with carrier density than would be suggested by Eq. 5.14. Even though

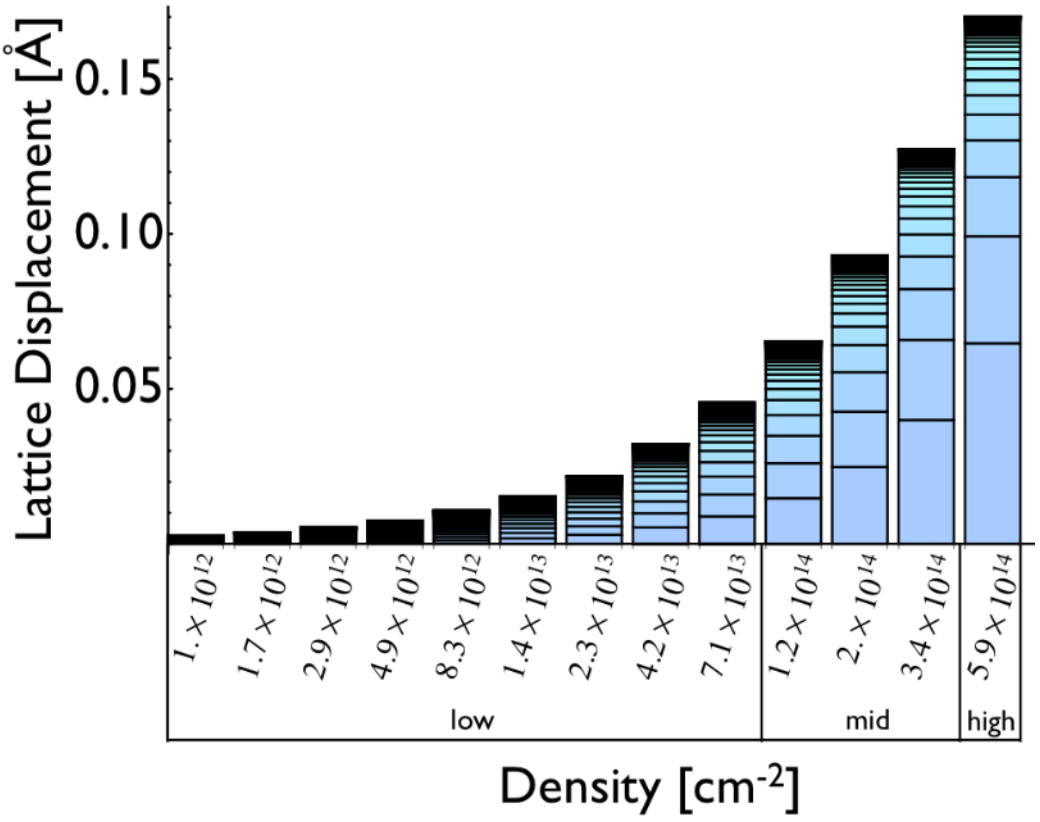

Figure 5.6: Lattice displacement as a function of total 2D density. For each density, the lattice displacement of layer i (counting from the surface) is plotted as the height of the i^{th} bar segment (counting from the bottom). For low-densities, the lattice displacements are small and in the linear regime. For mid-range densities, lattice displacements are suppressed by non-linear screening effects near the surface. Weaker lattice screening results in stronger confinement, larger 2D subband separations, and fewer occupied 2D subbands.

a substantial fraction of the total charge density starts to become confined within the top few layers, there is still a wide tail in the density distribution in the spatial region over which the external electric field has been reduced to a value less than $\sim 10^{14}\mathrm{cm}^{-2}\epsilon_\infty/(4\pi e)$ so that the screening is locally linear. In our model the non-locality of these screening properties is set by the width in momentum space of the long-wavevector limit of the soft mode. In our numerical calculations, this low-density quasi 3D regime is influenced by our hard-wall cut-off of the 2DEG beyond a width of 60 unit cells.

As was the case in the low density regime, the inclusion of SO coupling and the tetragonal distortion alters the the orbital character of the lowest energy band and decreases its surface confinement. Their influence is reduced compared to the low-density regime however. As illustrated in Fig. 5.7 we find that, at the 2D Γ point, the two lowest bands are dominantly xy in character and that the next occupied subbands are $\{yz, zx\}$ in character. Although the number of 2D subbands has increased significantly, only a few are needed to account for the most strongly confined part of the density (see the inset of Fig. 5.1).

5.5 High carrier densities - above 5×10^{14}

The 2DEG electronic structure simplifies again in the high-density limit, which we define as the limit with more than half of the total density in the first TiO_2 layer - see Fig. 5.8. For large electric fields, and therefore large carrier densities, lattice screening is irrelevant near the surface. Because of the relatively large conduction band masses, compared to typical covalent semiconductor cases, and the much

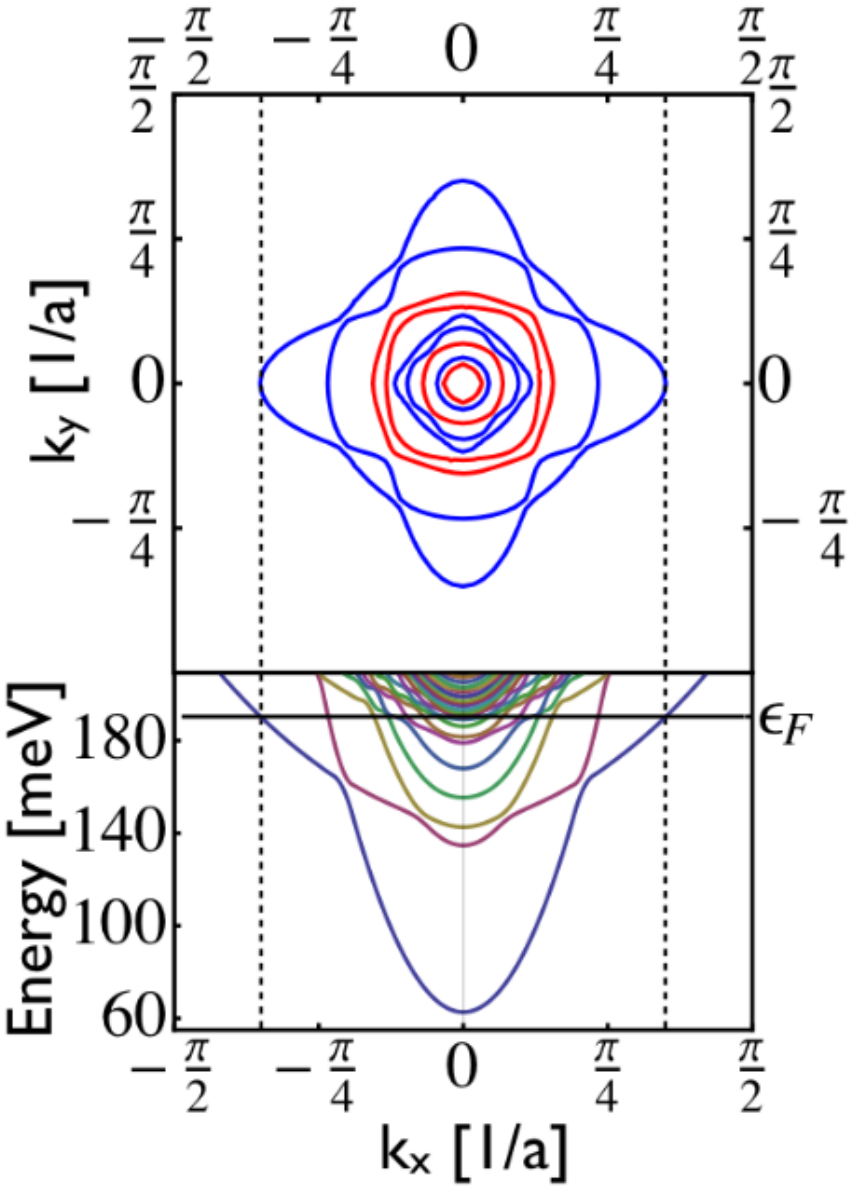

Figure 5.7: (a) Fermi surface and 2D band structure for $n_T = 2.0 \times 10^{14}$. The dominant orbital character of a band at the 2D Γ point is represented by line color with blue and red indicating xy and $\{yz, zx\}$, respectively. The zero of energy is set to the potential minimum in the first layer. The Fermi energy is represented by a solid (black) horizontal line. Although the separation between the lowest energy 2D subbands is large, many low density subbands with small energy separations are still present near the Fermi energy.

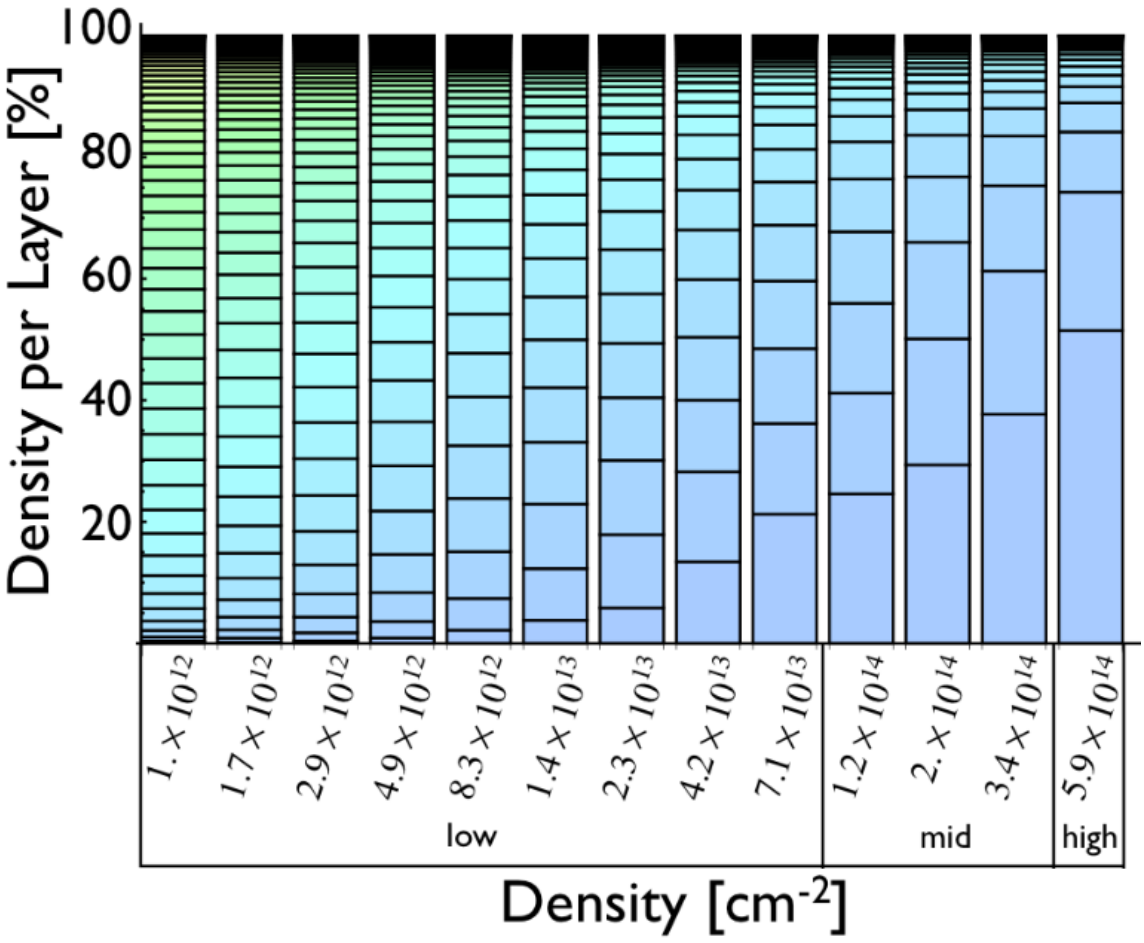

Figure 5.8: Layer resolved density (as a percent of total density) as a function of the total density. For each density each segment represents the percent of the total density in the corresponding TiO_2 layer, starting with the first layer and moving upward. For low densities the 2DEG is spread over many layers. Above $n_T \sim 10^{14} cm^{-2}$, the confinement becomes pronounced. In the high density regime, more than 50% of the total density is confined within the first layer due mainly to reduced lattice screening at large electric fields.

stronger electric fields at these carrier densities, surface confinement occurs on an atomic length scale. The Γ-point splitting becomes comparable to the single layer limit of Eq. 5.2 - see Fig. 5.9. While the SO coupling leads to hybridization and a decrease in confinement that mainly affects the quasi 3D tail of the electronic distribution, the tetragonal distortion does not have a noticeable effect. In this regime, if we neglect the quasi 3D tail region, there are only a few spin-degenerate 2D subbands contributing to the density. At the 2D Γ point, the first three bands are dominantly xy and $\{yz, zx\}$ - going from low to high energy. For the high-density regime, the tight-binding model of Eq. 5.1 must be used.

5.6 Summary and Discussion

Using a simplified tight-binding model for the t_{2g} bands, we find that non-linear screening plays an essential role in determining the electronic properties of surface confined 2DEGs in grounded $SrTiO_3$. For low-density ($n_T < 10^{14}\text{cm}^{-2}$) 2DEGs, electrons are distributed over many layers because surface confinement is weakened by the host material's extremely large linear dielectric constant. In the mid and high density regimes, a low density tail is still present over 50 or more layers but a high density region emerges over the first few atomic layers. Although many 2D subbands are always present in the mid and high density regimes, the few lowest energy subbands which contain strongly confined orbitals account for most of the total density (see Fig. 5.1). Subbands that have substantial $\{yz, zx\}$ orbital character are present at all densities in the grounded configuration investigated in this study. The presence of many subbands with different orbital character at the Fermi level

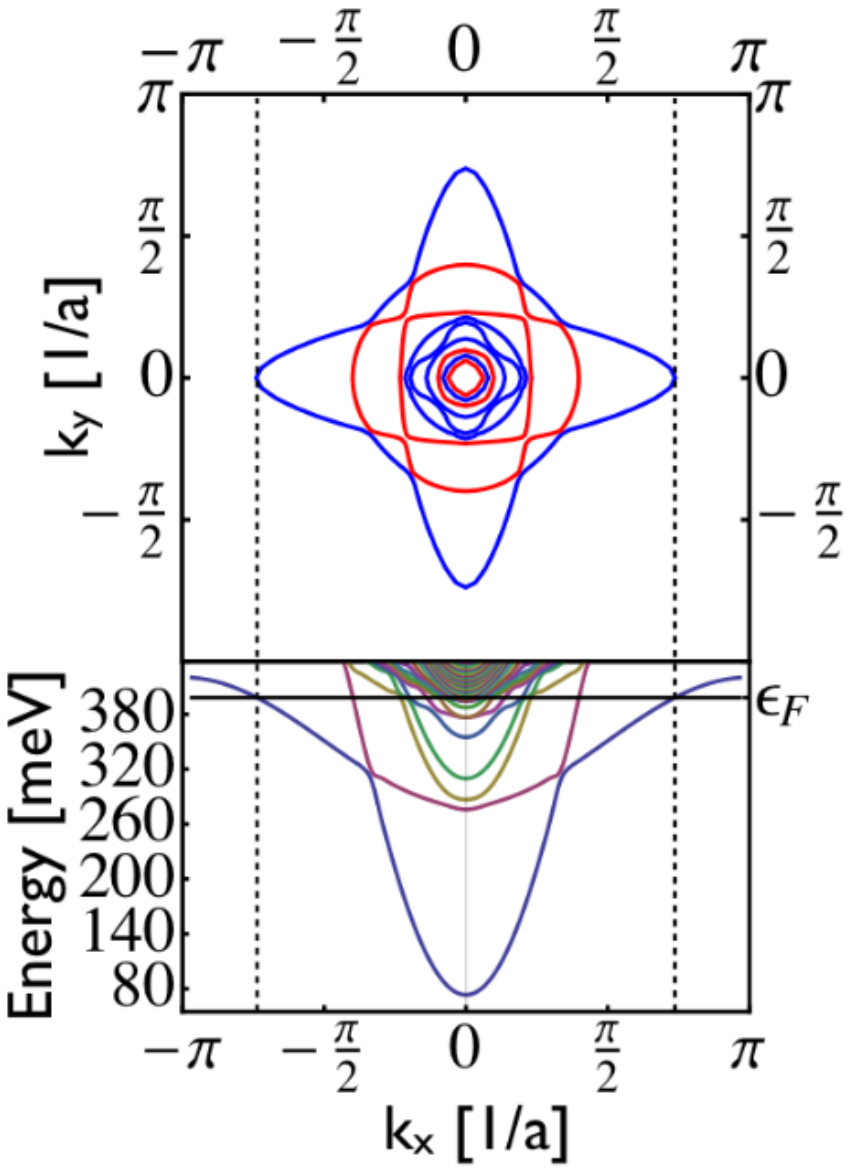

Figure 5.9: (a) Fermi surface and 2D band structure for $n_T = 5.9 \times 10^{14}$. The dominant orbital character of the band at the 2D Γ point is represented by line color with blue and red for xy and $\{yz, zx\}$, respectively. The zero of energy is set to the potential minimum in the first layer. The Fermi energy is represented by a solid (black) horizontal line. The 2D subband splitting is $\sim 200meV$ - becoming comparable to the single layer model of Eq. 5.1. Near the Fermi energy, many subbands are present with $\sim meV$ splitting, which contribute to the carrier density far from the surface.

suggests that the interpretation of transport properties in these systems is not likely to be straightforward.

$SrTiO_3$ is well known for exhibiting superconductivity in the bulk [14, 123] where it appears over a broad range of carrier densities from $\sim 10^{18}\text{cm}^{-2}$ to more than $\sim 10^{20}\text{cm}^{-2}$ and has a maximum value $\sim$ 400mK [14, 123]. In one study of gated $SrTiO_3$ 2DEG systems [26], with Hall densities in the range from $\sim 10^{13}\text{cm}^{-2}$ to $\sim 10^{14}\text{cm}^{-2}$, the superconducting transition temperature initially increased with carrier density but decreased at the higher densities. Referencing to Fig. 5.5 for 3D densities associated with the weakly confined tail, we find that the measured surface 2DEG T_c's compare well with values reported for bulk systems [14, 123]. In another study [27], superconductivity was seen only at a Hall density of $3.9 \times 10^{14}\text{cm}^{-2}$ with a transition temperature of near $\sim 400mK$. Because of experimental limitations superconductivity was not seen at other densities but could have been present at lower transition temperatures [27]. In $LaAlO_3/SrTiO_3$ systems the reported 2DEG densities are in the low density range. It is therefore not surprising that the measured T_c values are correspondingly suppressed [30–32, 34, 35]. (The carriers found in $LaAlO_3/SrTiO_3$ 2DEG systems are thought to be induced by a polarization discontinuity, although the small value of the measured 2D carrier densities is not completely understood.) We conclude that existing studies are consistent with surface 2DEG and bulk superconductivity in $SrTiO_3$ having a common origin.

The strongly confined portion of the electron distribution in the mid and high density regimes has significant $\{yz, zx\}$ character. (See Figs. 5.7 & 5.9). The increase in the density of states associated with these heavy 2D bands could account for the

observed ferromagnetism[31, 32, 34, 35, 59], if it is describable by a Stoner criterion. The spatial separation between the strongly confined and the low density tail portions of the 2DEG distribution may account for the coexistence of superconductivity and magnetism seen in some systems [31, 32, 34, 35]. This scenario should be compared with one in which superconductivity and magnetism both occur in strongly confined subbands; the two pictures should be experimentally distinguishable because of the strong influence of magnetism and spin-orbit coupling on superconducting properties[33] in the spatially coincident case.

The low density tail is a consequence of the property that the electric field vanishes far from the surface of a grounded system with a surface-bound 2DEG. The non-linear screening properties that we have discussed imply that a back-gate applied to the surface 2DEG to increase the strength of the electric field strength deep below the surface will have an exaggerated impact on the low-density tail of the distribution function and on the corresponding closely-spaced 2D subbands near the Fermi surface. A gate electric field with strength $\sim 10^{14} cm^{-2} \epsilon_\infty / 4\pi e$ should essentially eliminate the tail region. Our prediction that superconductivity is associated with the low density tail can therefore be tested by back gating which should suppress and eventually eliminate superconductivity[100] without having a large influence on magnetism. Irrespective of the reliability of these predictions, it seems clear that studies of the electronic properties in dual-gated samples could be quite informative in building up a confident understanding of 2DEG properties.

Chapter 6

Theory of t_{2g} electron-gas Rashba interactions

In this chapter, the tight-binding model of Chapter 5 is addressed in more detail to understand Rashba interaction within the t_{2g} conduction band.

6.1 Introduction

Recent experimental studies of two-dimensional electron systems (2DESs) involving $SrTiO_3$[124–129] and $KTaO_3$[119, 130] have found evidence of strong spin-orbit-interactions (SOI) which could be valuable in spintronics. These experiments have been interpreted using established ideas which apply to conventional semiconductors. In this study we present a theory that applies directly to strong SOI induced spin-splitting in 2DESs formed at t_{2g} perovskite surfaces and heterojunctions and establishes some essential differences. In particular we find that interaction spin splitting magnitudes are controlled by changes in metal-oxygen-metal bond angles and by atomic spin-orbit interaction strengths.

The spin-degeneracy of Bloch bands in a crystal can be lifted[131, 132] when SO coupling is present and inversion symmetry is absent. In a 2DES spin-degeneracy is lifted by Rashba interaction[133, 134] terms - symmetry invariant Hamiltonian contributions that are scalar products of spin and orbital axial vectors. Rashba inter-

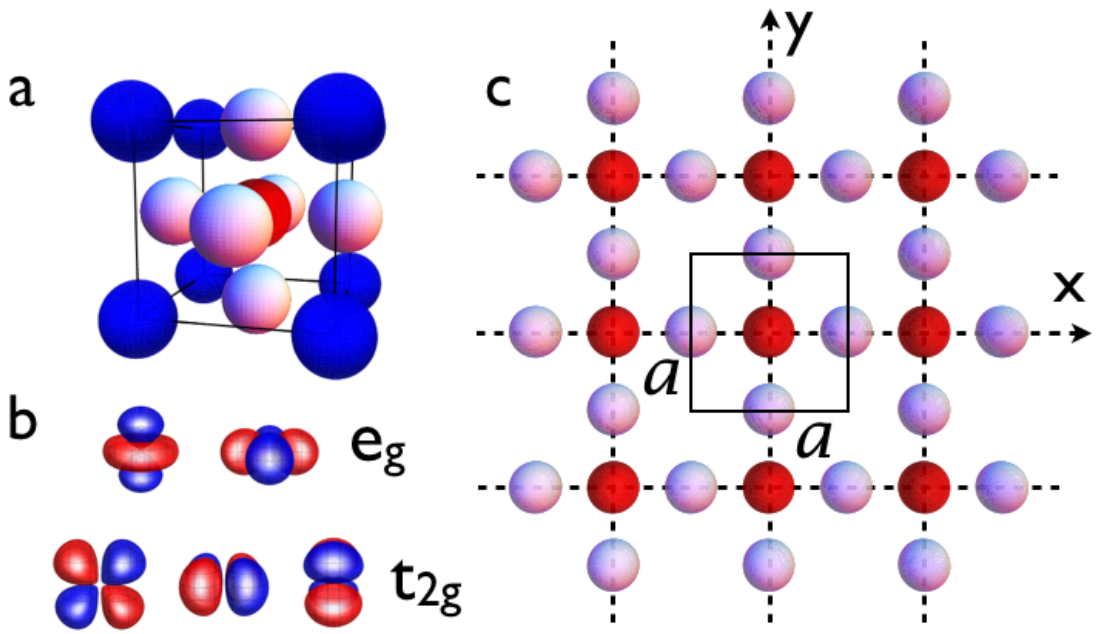

Figure 6.1: **Perovskite crystal structure.** **a**, Bulk cubic unit cell with the A atom in blue, B atom in red, and the oxygen in white. **b,** Splitting of atomic d-orbitals into e_g and t_{2g} manifolds. **c,** Single BO_2 plane with one unit cell, with area a^2, in the boxed region.

actions are symmetry allowed whenever a 2DES is not invariant under reflections through the plane it occupies. In this chapter, we use a tight-binding model informed by *ab initio* electronic structure calculations to develop a theory of Rashba splitting in the t_{2g} bands of the two-dimensional electron systems[17, 26, 29, 88, 106] formed at cubic perovskite crystal surfaces and interfaces. We find that Rashba splitting in these systems is due to atomic-like on-site SO interactions combined with processes in which t_{2g} electrons change orbital character when they hop between metal sites. These processes are absent in a cubic environment and are due primarily to polar lattice distortions which alter the metal-oxygen-metal bond angle.

As addressed in Chapter 1, bulk cubic perovskites have chemical formula ABO_3 and the crystal structure illustrated in Figure 6.1a. The 2DESs in which we are interested are formed from conduction band B-site transition metal d-orbitals. Because the B site, at the cubic cell center, has octahedral coordination[135] with neighboring oxygen atoms, located at the centers of the cubic cell faces, oxygen-metal bonding partially lifts the degeneracy of the d-orbitals, pushing the $e_g = \{x^2 - y^2, 3z^2 - r^2\}$ orbitals up in energy relative to the $t_{2g} = \{yz, zx, xy\}$ orbitals (Figure 6.1b). In the simplest model of the bulk electronic structure[39], the bonding networks of the three t_{2g} bands are decoupled; an xy-orbital on one B site, for example, can hop only along the y or x direction through an intermediate p_x or p_y orbital to an xy-orbital on the B site of a neighboring cubic cell. In perovskite 2DESs, the t_{2g} bands are reconstructed[36, 37] into 2D subbands whose detailed form depends on the bulk band parameters[50], the surface or interface confinement mechanism, and the dielectric response of the material. A polar displacement of A and B atoms relative to the

oxygen octahedra occurs in response to the confinement electric field; this is the same response that is responsible in some materials (including in particular $SrTiO_3$) for extremely large bulk dielectric constants[36, 52]. At the same time atomic-like SO splitting interactions hybridize the three t_{2g} orbitals, which are split in the 2DES by differences in their confinement energies. (For $\langle 001 \rangle$ 2DESs (assumed below) xy orbitals, which have weak bonding along the z-direction, have the lowest confinement energy.) We explain below how these two effects combine to produce a Rashba interaction.

6.2 t_{2g} Rashba interactions

The Rashba interaction couples an orbital axial vector that is odd under $z \to -z$ to spin, and must therefore arise from hopping process that are odd under inversion in the $x - y$ plane. We therefore begin by considering a single plane (see Figure 6.1c) of metal atoms and identify the relevant process by using a tight-binding model[136] for $p - d$ hybridization, assigning a hopping amplitude t_{pd} to the process discussed above. Because of the difference in parity between p and d orbitals, t_{pd} changes sign when the hopping direction changes (Figure 6.2). To leading order in t_{pd} virtual hopping via oxygen sites, the Hamiltonian is diagonal in the t_{2g}-space with eigenenergies:

$$\begin{aligned} \epsilon_{yz} &= 4t_1 - 2t_1\cos(k_y a) \\ \epsilon_{zx} &= 4t_1 - 2t_1\cos(k_x a) \\ \epsilon_{xy} &= 4t_2 - 2t_2 cos(k_x a) - 2t_2 cos(k_y a) \end{aligned} \tag{6.1}$$

Here $t_{1,2} = t_{pd}^2/\Delta_{pd}$ where Δ_{pd} is the splitting between the oxygen p and metal t_{2g} energy levels and the subscripts acknowledge a symmetry allowed difference, ignored below, between xy and $\{yz, zx\}$ hopping amplitudes in the planar environment. Note that the xy band is twice as wide as the $\{yz, zx\}$ bands, and lower in energy at the 2D Γ point. Level repulsion from apical oxygens contributes $2t_1$ to $\epsilon_{yz,zx}$. Even when combined with on-site SO terms, this effective metal-to-metal hopping does not produce a Rashba effect. This is because the metal-to-metal hopping amplitude is independent of direction. In order to explain the Rashba effect, we must look more deeply into how the bonding network is altered in an electric field.

Rashba interactions are caused by broken mirror symmetry and in particular by the associated electric field E perpendicular to the 2DES plane. For t_{2g} 2DESs, this field both polarizes the atomic orbitals and induces a polar lattice displacement. These effects open new covalency channels in the metal-oxygen network. In particular there is no hopping in the unperturbed system between a metal zx-orbital and an oxygen x-orbital separated along the y-direction. This is because the x-orbital is even and the zx-orbital is odd under reflection in the xy-plane passing through the metal-oxygen bond. When $E \neq 0$, the Hamiltonian is no longer invariant under this

reflection and the hopping process is allowed. If, for example, we think about the perturbation as arising from an additional potential $-eEz$, we can write the induced hopping amplitude approximately as $E\gamma_1$, where $\gamma_1 = \langle zx, \vec{R} = 0| - ez|x, \vec{R} = a/2\hat{y}\rangle$ (Figure 6.2a). At the same time, the electric field will produce forces of opposite sign on metal cations and oxygen anions. The induced polarization will change the metal oxygen bond angle introducing a non-zero $\hat{z}$-component direction cosine n in the bond axis direction. In a 2-center approximation, this change also gives a non-zero amplitude nt_{pd} for zx to x hopping along the y direction. Similar considerations imply an identical yz to y hopping amplitude along x. (See Figure 6.2b). Including these weak effects, which at leading order act only once in the two-step metal-oxygen-metal hopping process, we obtain an additional effective metal-to-metal hopping amplitude that changes sign with hopping direction and therefore produces a Rashba effect. The (yz, zx, xy)-representation Rashba Hamiltonian is

$$H_E^{t_{2g}} = \begin{pmatrix} 0 & 0 & -2it_R \sin(k_x a) \\ 0 & 0 & -2it_R \sin(k_y a) \\ 2it_R \sin(k_x a) & 2it_R \sin(k_y a) & 0 \end{pmatrix}, \tag{6.2}$$

where the Rashba interaction strength parameter $t_R = (\gamma_1 t_{pd} E)/\Delta_{pd} + (nt_{pd}^2)/\Delta_{pd}$. This Hamiltonian was first written down in continuum limit in the Supplementary information of the Ref. [137] by Joshua *et al.*. They reached this result by a symmetry analysis of the t_{2g} conduction band minimum. Zhong *et al.* have suggested a scheme for finding the parameter t_R using Wannier projected orbitals and VASP [138]. When combined with the an atomic-like bulk SO interaction (Eq. 5.5), $H_E^{t_{2g}}$ leads to Rashba spin-splitting in the t_{2g} bands. We remark that broken mirror plane symmetry also introduces other covalent bonding channels, but these do not contribute to the Rashba

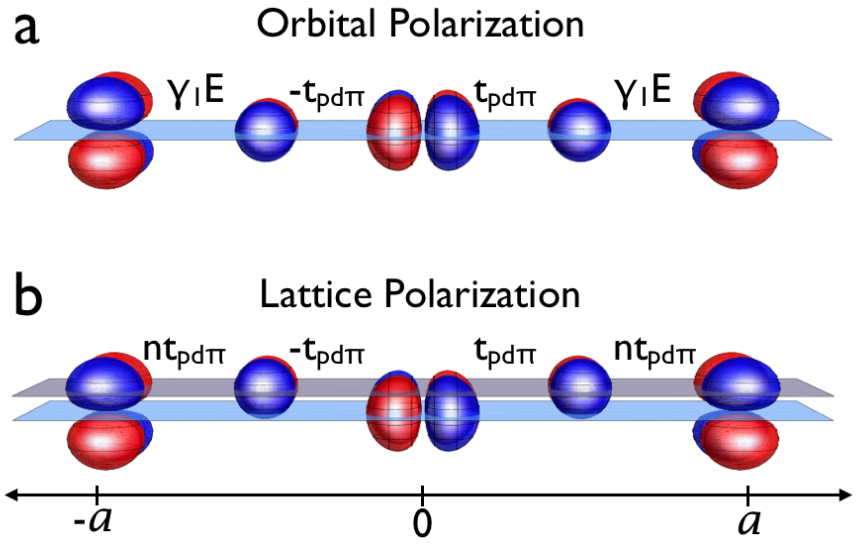

Figure 6.2: **Bonding network along the y-axis with an electric field. a,** Orbital polarization. Bonding between zx and xy on neighboring metal atoms through p_x orbitals. The positive and negative lobes of the orbital functions are represented in blue and red, respectively. **b,** Lattice Polarization. Displacement of the metal (light blue plane) and oxygen (light purple plane) sublattices in an electric field.

effect (see Appendix C). We also note that, a surface metal atom in a BO_2 terminated perovskite is not octahedrally coordinated. This absence of local inversion symmetry and the decrease in level repulsion with neighboring oxygen atoms mixes e_g and t_{2g} orbitals at the surface. When this mixing is strong, a more elaborate theory of Rashba SO coupling is required.

As discussed in Chapter 5, t_{2g} 2DESs will, in general, be spread over many coupled metal layers, and the Rashba Hamiltonian $H_E^{t_{2g}}$ will act within each layer with a layer-dependent coupling constant t_R. For the extreme case of a single-layer t_{2g} 2DES, the xy- band will be pulled below the $\{yz, zx\}$-bands by differential confine-

ment effects. In this case we can derive a simple effective Rashba Hamiltonian which acts within the xy subspace. To do so, we define δ as the energy scale which splits the xy and $\{yz, zx\}$ bands at the Γ point. Allowing virtual transitions to the $\{yz, zx\}$ manifold due to orbital/lattice polarization ($H_E^{t_{2g}}$), and bulk SO effects (H_{SO}), we find the part of the Hamiltonian linear in electric field is given at small k by,

$$H_R^{xy} = \epsilon_{xy}(\vec{k}) - \alpha\, \vec{\sigma} \cdot (\vec{k} \times \hat{z}) \tag{6.3}$$

where $\alpha = 4\Delta_{SO} t_R a/(3\delta)$. This expression, valid for small k and for the xy band only, has the conventional Rashba Hamiltonian form. In this single-orbital limit the Rashba interaction is equivalent to an effective magnetic field. Away from the 2D BZ center the direction of the Rashba field is no longer perpendicular to $\vec{k}$.

Analogies between Rashba interactions in oxide 2DEGS and Rashba interactions in conventional semiconductor 2DESs are very limited. t_{2g} 2DESs are in general composed of subbands of $\{yx, zx, xy\}$ character and as such, Eqns. 1, 2, and 3 need to be coupled and solved in the presence of a confining potential in order to achieve a minimal model of the electronic structure[36, 37].

6.3 *ab intio* results

To support our theory of the Rashba effect we have carried out an *ab initio* study of a typical t_{2g} 2DES. The first principles calculations were based on density functional theory and carried out using the Vienna *Ab Initio* Simulation Package[139]. To simplify the comparison we examined the case of a single $\langle 001 \rangle$ BO_2

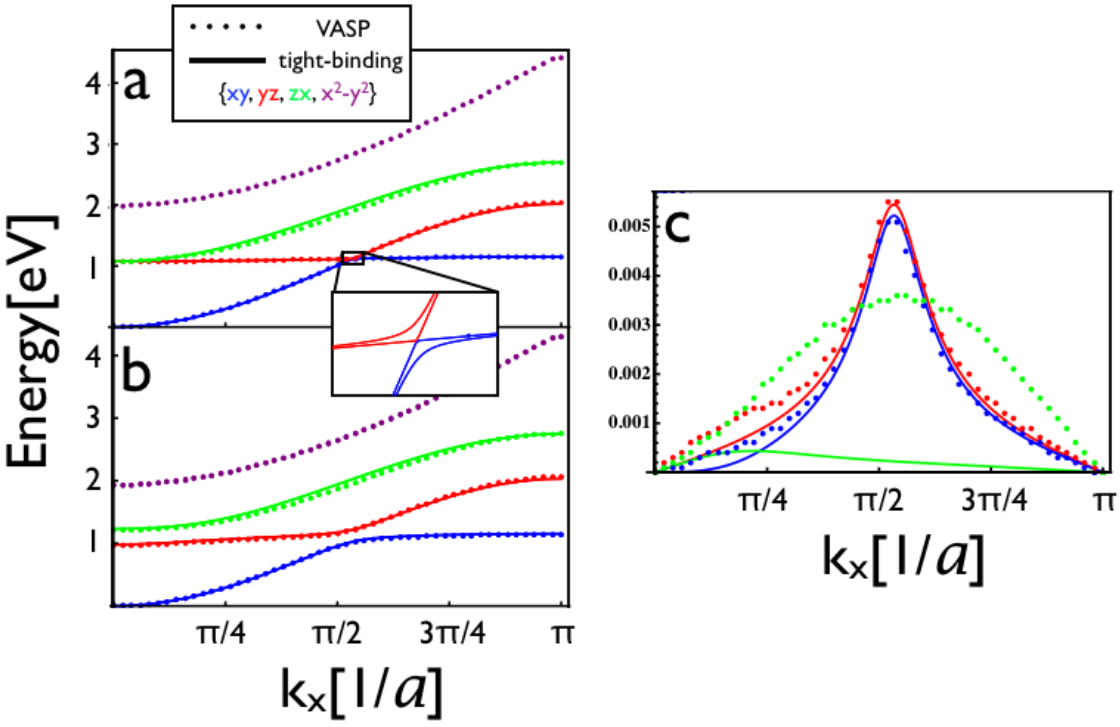

Figure 6.3: **Orbital polarization changes to t_{2g} bandstructure.** **a,** t_{2g} bandstructure in the absence of an electric field and SO coupling. The results of our model are shown as solid lines while the simulation is shown as dotted lines. The band order (at the Γ point and in the absence of SO interactions) is xy (blue), yz (red), zx (green), and $x^2 - y^2$ (purple). The inset shows the onset of an avoided crossing in the presence of an electric field. **b,** t_{2g} band structure with SO coupling and orbital polarization. **c,** Comparison of the orbital polarization part of the Rashba splitting in the t_{2g} space.

plane and studied the influences of z-direction external electric fields and oxygen-metal sublattice relative displacements separately. Because we expect Rashba splitting to be proportional to Δ_{SO} we use the $5d$ transition metal Halfnium (Hf) as the B atom. To minimize the mixing between t_{2g} and e_g bands, approximate octahedral coupling has been maintained by including apical oxygens. In our calculations we used projector-augmented wave pseudopotentials and the generalized gradient approximation exchange-correlation functional of Perdew, Burke and Ernzerhof[140]. The supercell contained a three atom HfO_2 layer with two oxygen atoms located directly above and below the Hf atom. The molecular layers with 4.054 Å lattice constant were separated by a 20 Å vacuum, the plane-wave energy cutoff was set to 500 eV, and we employed $8 \times 8 \times 2$ k-point sampling to achieve electronic convergence. Figure 6.3a shows the band structure of a Hf perovskite plane with ideal atomic positions in the absence of an applied external electric field when spin-orbit interactions are neglected. At the zone center, the xy band has lower energy than the $\{yz, zx\}$ bands as expected in t_{2g} 2DESs. The strength of the Rashba hopping processes can be read off the band structure by identifying the avoided crossing which occurs between an xz or yz band. We find that even for an extremely large electric field, $0.1eV/\text{Å}$, the level repulsion (Eqn. 6.2) at the crossing is very small. Figure 6.3b shows the band structure changes when SO coupling is included. Note the expected confinement-induced t_{2g} manifold degeneracy lifting at the Γ point. On the scale of this figure, the Rashba splitting is too small to be visible. Figure 6.3c plots the spin splitting as a function of k, which is largest near the band crossing and reaches a maximum value of $\sim 5meV$. The calculated splitting agrees well with the splitting

Tight-Binding Model Parameters		
Lattice Constant	a	4.05 Å
SO splitting	Δ_{SO}	0.340 eV
Orbital Polarization	t_1	0.41 eV
	t_2	0.51 eV
	t_R	0.0014 eV
	t'	0.02 eV
Lattice Polarization	t_1	0.30 eV
	t_2	0.48 eV
	t_R	0.045 eV
	t'	0.02 eV

Table 6.1: Tight-binding parameters used in fitting *ab initio* results for HfO_2 plane.

predicted by our model with the value of t_R fit to the *ab initio* bands calculated in the absence of spin-orbit coupling(See Table 6.3).

Figure 6.4 reports the corresponding results obtained for the case of a polar lattice displacement. Figure 6.4a shows the bandstructure for a Hf perovskite plane with a displacement of 0.2 Å. The Hf atom displacement was chosen to emulate the interface atomic configuration. According to earlier first principles calculations for $LaTiO_3/SrTiO_3$ interfaces[112], Ti atoms at the interface are displaced out of the TiO_2 plane by $\sim 4\%$ of the lattice constant. For illustrative purposes we report results for a similar Hf atom displacement of $\sim 5\%$ of a lattice constant.

The yz, xz-xy avoided crossing is now easily visible. After SO coupling is included, a clear Rashba splitting is visible (Figure 6.4b,c) that is an order of magnitude larger than for the orbital polarization case. Note that our t_{2g} only model underestimates the zx band splitting in both cases, particularly close to the band center. We ascribe this to the proximity of the lower e_g level that is visible in the band plots and

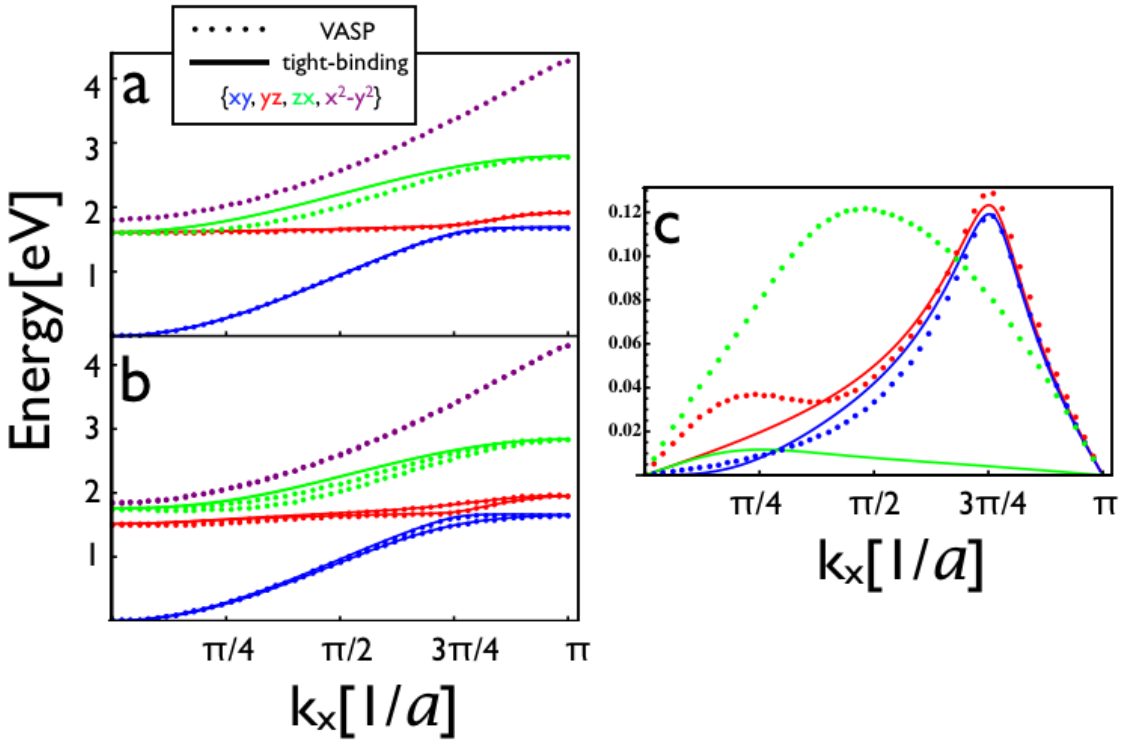

Figure 6.4: **Lattice polarization changes to t_{2g} bandstructure. a,** t_{2g} bandstructure in with lattice displacement and no SO coupling. The results of our model are shown as solid lines while the simulation is shown as dotted lines. The band order (at the Γ point and in the absence of SO interactions) is xy (blue), yz (red), zx (green), and $x^2 - y^2$ (purple). **b,** t_{2g} band structure with SO coupling and lattice displacement. **c,** Comparison of the lattice mediated Rashba splitting in the t_{2g} space.

neglected in our theory. For the xy band in the Hf case, we find $\alpha = 51.6$ meVÅ. Because $SrTiO_3$ is the most experimentally studied system we estimate α in that case. Assuming the yz, zx-xy splitting is comparable, we can scale this value by the SO splitting (18meV)[36] and lattice constant (3.904 Å) to find $\alpha_{SrTiO_3} \propto 2.6$ meV Å. The Rashba interaction strength has recently been estimated experimentally [124–126, 128] by using theory valid for conventional semiconductor two-dimensional systems to interpret weak-antilocalization effects apparent in low-temperature transport data. We emphasize that t_{2g} 2DESs differ greatly from conventional semiconductor 2DESs. This theory provides a starting point for a more quantitative interpretation of low-temperature transport data.

6.4 Summary

This theory of Rashba interactions in t_{2g} 2DESs is consistent with the qualitative experimental evidence for strong spin-orbit interactions at interfaces between polar and non-polar perovskites[124–126, 128], for example the $SrTiO_3/LaAlO_3$ interface, and in surface 2DESs induced by the very strong electric fields applied by ionic liquid gates. It also suggests that Rashba interactions will tend to be stronger in materials which are more easily polarized. In this sense $SrTiO_3$ has a potential for relatively strong spin-orbit interactions even though Ti is a light transition metal. This theory implies that magneto-transport properties in these 2DES conductors will be strongly sensitive to local lattice polarization at the surface or interface. We believe that this work can provide a starting point for the interpretation of heretofore unexplained magneto-transport phenomena[127, 129] and that it suggests new strategies

for designing two-dimensional electron systems with strong spin-orbit interactions, including systems that have superconducting or magnetic order[33].

Chapter 7

Optical conductivity of the t_{2g} 2DEG

In this chapter, the Kubo conductivity of the 2DEG formed in the t_{2g} bands of perovskite oxides is analyzed. When the electric field is polarized in the plane of the 2DEG, the optical conductivity is dominated by nearly independent Drude contributions from two-dimensional subband Fermi surfaces, whereas for perpendicular-to-plane polarization it has strong inter-subband features. This analysis suggests that perpendicular-to-plane optical conductivity studies may help advance understanding of the interplay between lattice distortions and electron-electron interactions in complex oxide 2DEG quantum confinement physics.

7.1 Introduction

Optical studies have played an important role in conventional semiconductor 2DEGs [141, 142]. Absorption of light with electric fields polarized perpendicular to the 2DEG plane has been especially valuable because it measures inter-subband optical transition energies and in this way characterizes 2DEG quantum confinement. No inter-subband optical response is observed [143] when light is polarized with its electric field polarized in the 2DEG plane. Because optical spectra can probe inter-subband transition energies, optical characterization can also has the potential to

play an important role in sorting out the quantum confinement physics in t_{2g} 2DEGs. Experimental guidance would be especially valuable because of the complicating influence in the oxide case by non-linear dielectric screening and the greater likelihood of structural distortions and defects at interfaces. In this chapter the optical conductivity of t_{2g} 2DEGs is explored theoretically, with a view toward shedding light on the information which can be garnered from future experimental studies[144]. The optical response of the t_{2g} 2DEG is dominated by electrons within the first few layers of the surface or interface. When light is polarized in the 2D plane, the conductivity is dominated by a Drude peak to which all occupied t_{2g} orbitals contribute. The integrated strength of this peak provides information on the carrier density which is complementary to that available from Hall effect measurements. Their are however weak inter band peaks which could be very revealing if they could be detected. Measurements of the peak frequencies should be very valuable in constraining confinement models. The corresponding peak strengths are sensitive to hybridization between different t_{2g} orbitals, which is weak in the ideal case, and may therefore shed light on spin-orbit coupling strengths and on structural distortions of the pseudocubic cell near the interface. For light polarized perpendicular-to-plane, the optical conductivity has large inter subband features related to hopping amplitudes perpendicular to the interface, and to the confining potential. In Section 7.2 the Kubo formula is applied to the 2DEG model of Chapter 5. The main results are presented and discussed in Section 7.3. The chapter concludes in Section 7.4 with a brief summary.

7.2 Linear response theory

We consider the response of the 2DEG current to a weak external electromagnetic field. The conductivity tensor is given by the well-known Kubo formula[145]:

$$\sigma_{\alpha\beta}(\omega) = i\hbar \sum_{m,n,\vec{k}} \left(\frac{f_n - f_m}{\epsilon_m - \epsilon_n} \right) \frac{\langle m,\vec{k}|\hat{j}_\alpha|n,\vec{k}\rangle\langle n,\vec{k}|\hat{j}_\beta|m,\vec{k}\rangle}{\hbar\omega - (\epsilon_m - \epsilon_n) + i\eta} \tag{7.1}$$

where m, n are band and α, β Cartesian direction indices, $\vec{k}$ is 2DEG crystal momentum, and $\hat{j}_\alpha$ is the paramagnetic component of the current operator for which an explicit expression is given below. The dependence of the Fermi distribution function f_n and the band energy ϵ_n on $\vec{k}$ is left implicit for notational simplicity. The ratio of Fermi factor to energy differences should be understood as a derivative in the $m = n$ limit so that the intraband contribution to the conductivity is

$$\sigma^{IB}_{\alpha\beta}(\omega) = i\hbar \sum_{n,\vec{k}} \left(-\frac{\partial f}{\partial \epsilon} \right) \frac{\langle n,\vec{k}|\hat{j}_\alpha|n,\vec{k}\rangle\langle n,\vec{k}|\hat{j}_\beta|n,\vec{k}\rangle}{\hbar\omega + i\eta} \tag{7.2}$$

We treat $\eta = \hbar\tau^{-1}$ as a phenomenological parameter which accounts for the Bloch state lifetimes, assigning it a value that is independent of band index.

In Eq. 7.1 we have taken the limit $q \to 0$ because wavelengths are long compared to lattice constants in the optical frequency regime. The paramagnetic current operator[146] is therefore given by the commutator of the Hamiltonian with the polarization operator $\hat{P}$:

$$\hat{j_\alpha} = -\frac{ie}{\hbar}[H, \hat{P}_\alpha] \tag{7.3}$$

In the tight binding approximation, electrons are considered to sit on lattice sites so position is discrete in real space. The polarization operator therefore takes the form:

$\hat{P} = \sum_i R_i \hat{n}_i$. It follows that the in-plane current operator is given by taking the derivative of the Hamiltonian with respect to crystal momentum. Therefore only the $\vec{k}$ dependent part of the Hamiltonian contributes to the in-plane conductivity. We find, from Eq. 5.1 that the x-direction current operator is spin-independent, diagonal in layer, and given in a $\{yz, zx, xy\}$ representation by,

$$j_x = \frac{e}{\hbar}\frac{\partial H}{\partial k_x} = \frac{ea}{\hbar}\begin{pmatrix} -2t'\sin(k_x a) & 0 & 0 \\ 0 & -2t\sin(k_x a) & 0 \\ 0 & 0 & -2t\sin(k_x a) \end{pmatrix}. \tag{7.4}$$

Note that the in-plane current operator couples only subbands with the same orbital character and that its action is independent of position relative to the interface. In the absence of orbital hybridization (due to SO coupling in the model considered) the bare Hamiltonian is also diagonal in orbital. It follows that in this case there are no intersubband transition contributions to the in-plane conductivity, either from transitions between subbands with the same orbital character or from transitions between subbands with different orbital character. When hybridization is neglected the in-plane orbital conductivity has only a Drude response centered on $\omega \to 0$.

Because the system is finite in the z-direction, the commutator in Eq. 7.3 is best evaluated in position space for this current component. We find that

$$j_z = -\frac{ie}{\hbar}\sum_{\vec{k},l,\gamma} a t_\gamma \left(\hat{c}^\dagger_{\vec{k},l+1,\gamma}\hat{c}_{\vec{k},l,\gamma} - \hat{c}^\dagger_{\vec{k},l-1,\gamma}\hat{c}_{\vec{k},l,\gamma}\right) \tag{7.5}$$

where $t_\gamma = \{t, t, t'\}$ for hopping the z-direction in the $\{yz, zx, xy\}$ basis (see Eq. 5.3). Because j_z is off-diagonal in layer index, optical transitions between different

subbands with the same orbital character are allowed even in the absence of inter-orbital hybridization. Although orbital hybridization can weakly allow additional optical transitions, intra-orbital contributions dominate the perpendicular-to-plane optical response, especially so when the Fermi energy is much larger than the SO splitting. For the calculations presented below this criterion is satisfied at medium and high densities.

The real part of the longitudinal conductivity tensor satisfies certain sum rules which are useful for verifying numerical results and also potentially useful in interpreting experiments. These sum rules limit conductivity contributions from intersubband transitions. By employing the commutation relation (7.3), we obtain the following sum rules for in-plane and perpendicular-to-plane conductivity tensors:

$$\begin{aligned}\int_{-\infty}^{\infty} d\omega Re[\sigma_{xx}(\omega)] &= \frac{\pi e^2}{\hbar^2}\sum_{m,\vec{k}}\langle m\vec{k}|\frac{\partial^2 H}{\partial k_x^2}|m\vec{k}\rangle f_m \\ &= \pi e^2 \sum_n \frac{n_n}{m^*_{xx,n}},\end{aligned} \tag{7.6}$$

$$\int_{-\infty}^{\infty} d\omega Re[\sigma_{zz}(\omega)] = -\frac{i\pi e}{\hbar}\sum_{m,\vec{k}}\langle m\vec{k}|[\hat{j}_z,\hat{P}_z]|m\vec{k}\rangle f_m, \tag{7.7}$$

Eq. 7.6 is the standard result that the electronic contribution to optical conductivity integrated over all frequency is proportional to the density of electrons in that band scaled by the inverse effective mass. The second form of the right hand side of Eq. 7.6 applies only in the low density limit in which the parabolic approximation for the band dispersion relations is accurate. Here n_n corresponds to the density of the n^{th} band. In the absence of SO coupling, Eq. 7.6 may be simplified further to,

$$\frac{\pi e^2}{\hbar^2}\sum_{\gamma}\frac{t_\gamma a^2}{2}n_\gamma, \tag{7.8}$$

where n_γ is the total density associated with electrons of orbital character γ. The commutator in Eq. 7.7 is:

$$-\frac{ia^2}{\hbar}\sum_{\vec{k},l,\gamma} t_\gamma(\hat{c}^\dagger_{\vec{k},l+1,\gamma}\hat{c}_{\vec{k},l,\gamma} + \hat{c}^\dagger_{\vec{k},l-1,\gamma}\hat{c}_{\vec{k},l,\gamma}) \tag{7.9}$$

Contributions to Eq. 7.7 are therefore directly proportional to the amplitude for an electron in layer l to hop to a neighboring layer.

7.3 Result and Discussion

Fig. 7.1 shows the real part of the in-plane optical conductivity for $\hbar\omega$ up to 200meV, including both the Drude conductivity and the intersubband part of the conductivity with the phenomenological scattering rate taken to be the same for both ($\eta = 10$meV). This value of η yields Drude peak heights in the range typical of recent *dc* resistivity measurements [147]. The Drude conductivity increases monotonically with the density of the 2DEG as expected from the sum rules discussed above. The in-plane optical conductivity is dominated by the Drude part for all densities. The integrated Drude weight may be used to estimate the total density, provided the effective masses in Eq. 7.8 can be estimated. From Eq. 5.1 the xy and zx bands masses along the x-direction are larger than the yz mass (by a factor ~ 10). This suggests, that in this limit, the Drude weight will typically be dominated by the

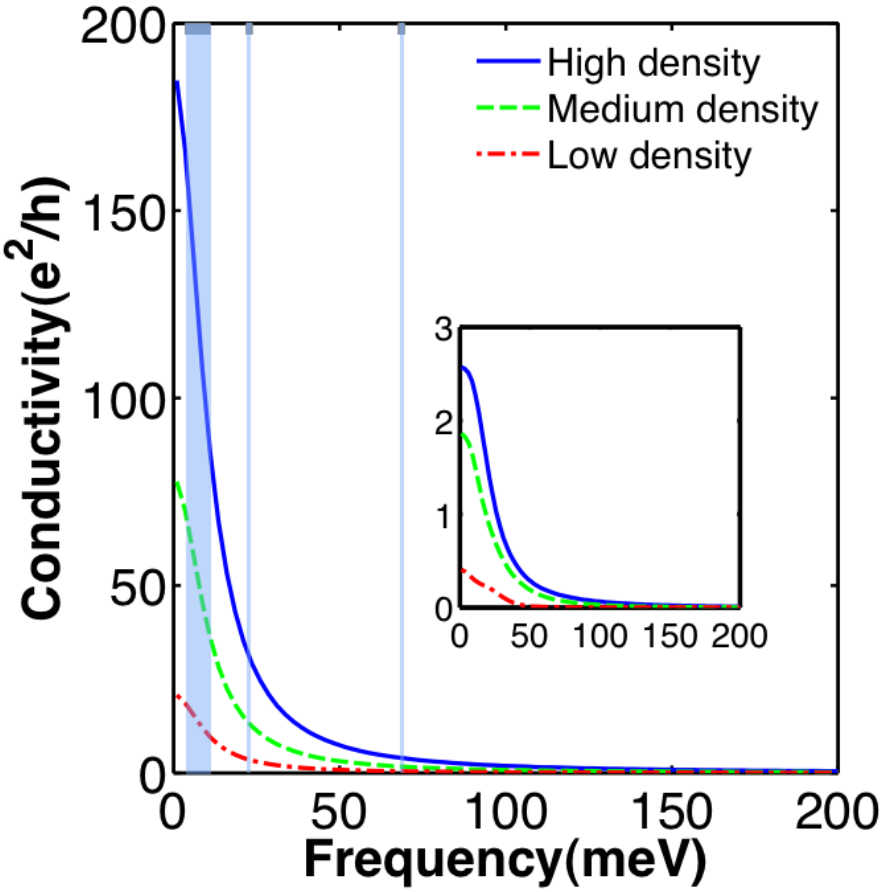

Figure 7.1: In-plane optical conductivity of a $SrTiO_3$ 2DEG in e^2/h units for light polarized in the plane of the t_{2g} 2DEG at high (5.9×10^{-14} cm^{-2}), medium (2×10^{-14} cm^{-2}), and low (2.3×10^{-13} cm^{-2}) carrier densities as defined in Ref. [36]. The shaded region in the figure highlights the frequency region in which the electronic conductivity is expected to be obscured by optical phonons. η has been set to 10 meV in order to yield $\omega \to 0$ limits that are similar to those observed experimentally. The inset shows the intersubband contribution to the conductivity which is contributed mainly by electrons in the low-density tail.

xy and zx pockets. The Hall conductivity can be used to provide a complementary estimate of the total carrier density which weights individual orbitals differently. (This analysis will be published elsewhere.) Measurements of both quantities could be very helpful in obtaining reliable experimental carrier density estimates.

As shown in the inset in Fig.7.1 there is a small interband contribution to the conductivity which originates from the low-density tail states. For these states, subband separations are comparable to spin-orbit coupling strengths ($\Delta_{SO} = 18$ meV) allowing for considerable orbital hybridization. The inter band contribution will likely be difficult to isolate experimentally because it is weak in a relative sense. Additionally because of the small band separations of tail states it will be difficult to separate spectrally from the Drude peak at typical values of η because it is also peaked close to $\omega = 0$. Interband features might be observable in systems with spin-orbit coupling strengths that are larger than those of $SrTiO_3$ ($\Delta_{SO} = 18$ meV) or in systems with substantially smaller lifetime broadening than is currently achievable (see below).

We remark that the utility of optical conductivity measurements as a probe of electronic properties is mitigated by the presence of strong optical phonon contributions. In Fig. 7.1 we have shaded the frequency ranges expected[53, 105] to be obscured by the three optical phonon modes which overlap with 2DEG energy scales. The frequency of the low energy phonon at the $\vec{q} = 0$ is strongly dependent on temperature. To represent this we have included a shaded region spanning its temperature dependence.

In t_{2g} 2DEG systems with strong spin-orbit coupling, spectral features asso-

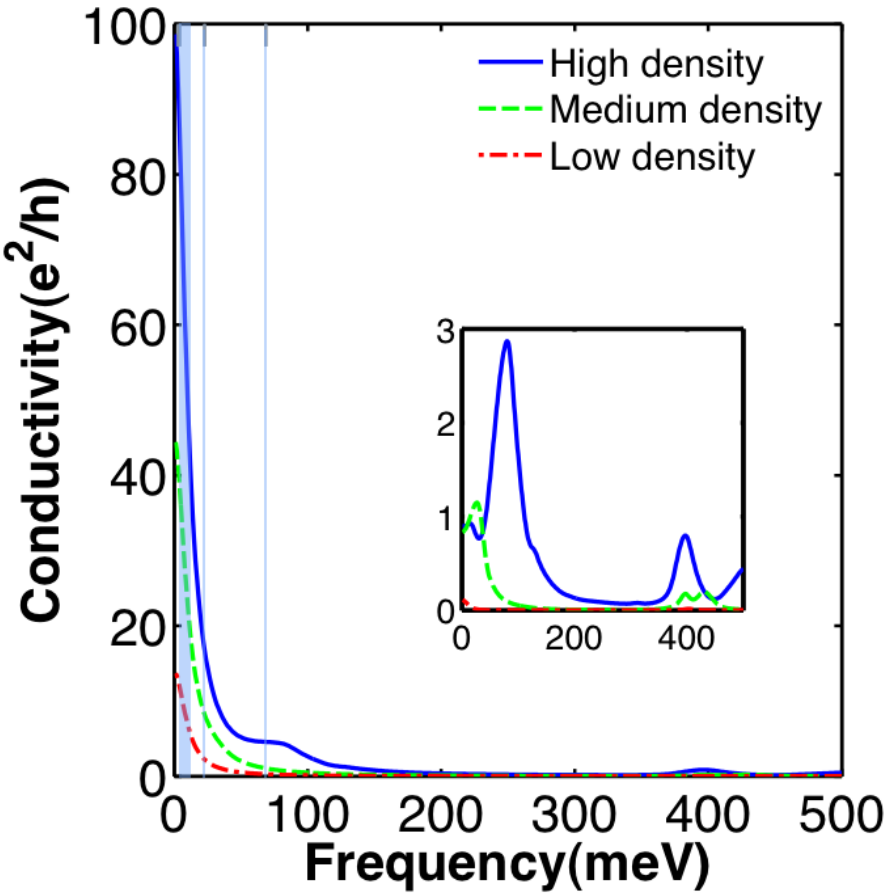

Figure 7.2: In-plane optical conductivity of a t_{2g} 2DEG with strong atomic spin-orbit coupling with strength $\Delta_{SO} = 400$ meV. The inset plots the intersubband part only. η has been set to 10 meV.

ciated with transitions between strongly confined orbitals may become visible. To illustrate this effect, we have artificially set the atomic spin-orbit coupling strength parameter $\Delta_{SO} \rightarrow 400$ meV in the $SrTiO_3$ 2DEG model and repeated the in-plane optical response calculation. In Fig. 7.2 we see that transitions within the weakly-confined subbands are again obscured because of the Bloch state lifetime. Now, however, the spin-orbit coupling strength is strong enough to induce appreciable hybridzation of the strongly-confined subbands. The inset of Fig. 7.2 again shows the inter-subband optical response features are most prominent at high carrier densities. The strongest feature is a broad peak centered at ~ 400 meV associated with transitions between spin-orbit split bands near the bottom of the conduction band. It is present at all carrier densities, but stronger at higher carrier densities. A second feature associated with the confinement energy scale is now allowed because of orbital hybridization within the t_{2g} manifold. Even in the high density case, the 400 meV SO coupling is larger than the confinement energy of the lowest subband. This suggests that all bands have strongly hybridized t_{2g} character. Since the SO coupling is local, it does not contribute to the current operator. Therefor, the matrix elements of the current operator in the optical conductivity still favor xy and zx orbitals due to their strong bonding in the x-direction. The peak at ~ 80 meV is dominated by a peak in the zx projected density of states related to the confinement energy of the most confined $\{yz, zx\}$ bands. Because the energy scales associated with structural deformations (of the parent material or induced by the interface) are not expected to be this large[41, 55], we conclude that in the absence of large SO coupling in plane conductivity measurements are unlikely to provide useful information.

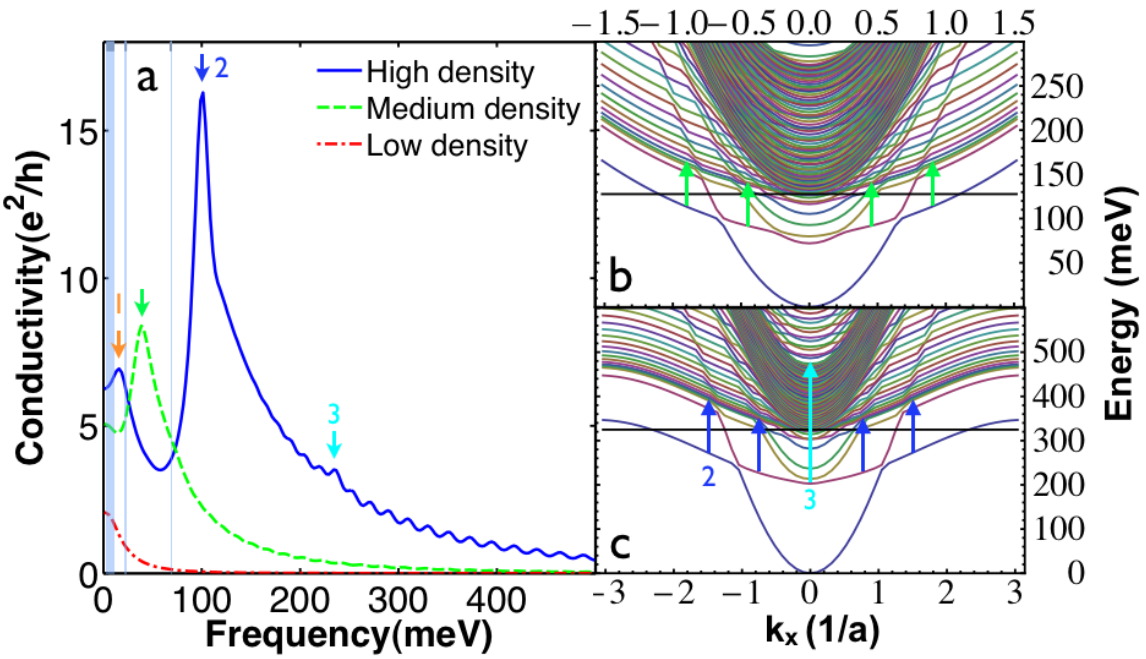

Figure 7.3: Perpendicular-to-plane optical conductivities for low medium and high densities **(a)**. **(b)** Self-consistent band structure for a density of $2 \times 10^{14}\text{cm}^{-2}$. **(c)** Self-consistent 2DEG subband structure for a density of $5.9 \times 10^{14}\text{cm}^{-2}$. The main optical transitions for perpendicular-to-plane polarization are indicated by color coordinated arrows the conductivity and bandstructure plots. Feature 1 is at too low a frequency to be evident in on the energy scale of **c**. The disorder-broadening η has been set to 10meV.

Typical perpendicular-to-plane response is illustrated in Fig. 7.3. In this case the current operator is diagonal in orbital, but not diagonal in subband. We therefore see a number of strong spectral features as summarized in Fig. 7.3a. At low carrier density, the subband splittings are not much larger than the lifetime broadening η and features associated with allowed transitions are therefore obscured in Fig. 7.3a. In practice, however, low-carrier density t_{2g} 2DEGs tend to have higher mobilities, and therefore smaller values of η so the situation depicted in Fig. 7.3a may be too

pessimistic. At our medium density, a peak emerges at ~ 40 meV that is associated with an optical transition from the lowest occupied heavy mass $\{yz, zx\}$ manifold to the many unoccupied subbands of $\{yz, zx\}$ character. In Fig 7.3b we show the electronic structure which yields these conductivities. The $\{yz, zx\}$ transitions are prominent because these bands have a large mass in one direction and therefore a larger density-of-states than xy bands, and also because they z-direction current operator is proportional to their larger inter-layer hopping amplitudes. We have highlighted the transitions responsible for the ~ 40 meV peak with green arrows in Fig. 7.3b.

For high densities, we see two features at ~ 16 and ~ 100 meV. We identify the higher energy features as originating from the $\{yz, zx\}$ transitions labelled "2" in Fig. 7.3c. (The "1" transition energy is too small to be clearly identified on the scale of Fig. 7.3c.) The calculations also reveal many small features at higher energies that we associate with transitions between the most strongly confined t_{2g} subbands and the large number of bulk-like bands due to the 60 layer simulation (see Chapter 5). These features would become sharper if we performed our calculations with a smaller phenomenological scattering rate η. We expect, however, that in typical systems they will yield a smooth tail in the optical response. In Fig. 7.3c, highly dispersive nearly 3D xy subbands can be seen with a characteristic energy width of $4t' \sim 140$ meV. These subbands are more densely spaced at the top and bottom of this manifold due to the bonding between neighboring layers. The non-zero SO coupling causes hybridization within the t_{2g} manifold that allows {yz,xz} transitions to this xy manifold. The two dominant SO mediated transitions discussed above are

at 100 meV and 240 meV. The 100 meV transition gives a small contribution to the "2" peak and is therefor obscured by $\{yz, zx\}$ to $\{yz, zx\}$ transitions. We label the "3" peak by the 240 meV transition which is not obscured by the dominant $\{yz, zx\}$ to $\{yz, zx\}$ processes.

We remark that optical spectroscopy features in conventional semiconductor 2DEGs are shifted from the subband splittings by depolarization effects [141, 148]. When electrons transition to unoccupied states, the charge distribution along the z direction is altered, which in turn alters the time-dependent electric field. Similar shifts will occur in oxide 2DEGs. The peak shift is[148] $2e^2nES/\epsilon$ where n is the density of the electrons involved in the transition, E is the subband splitting and S is an effective Coulomb interaction length[148] for the corresponding transition. In the conventional case, inter-subband transition energies are small enough that ϵ can be taken to be the static dielectric constant of the host semiconductor material. In the present case many of the transitions of interest involve strongly confined t_{2g} electrons, and have frequencies larger than many of the important optical phonons. (See Fig. 7.3 a for example). In our medium density case, the transition energy falls between optical phonon modes at around 20 and 70meV. The effective dielectric constant in bulk $SrTiO_3$ in this frequency range is $\epsilon \sim 10$. If we assume 10^{14} cm^{-2} $\{yz, zx\}$ electrons are involved in the transition and that the Coulomb interaction length is $\sim$ 1 lattice constant we estimate that the peak shift is on the order of 190 meV. This simple estimate shows that the depolarization shifts are potentially large. Because optical phonon oscillator strengths and frequencies are likely to be substantially altered close to surfaces and interfaces, a fully quantitative theory of

depolarization shifts in perovskite t_{2g} 2DEGs will be quite involved.

7.4 Summary and Conclusions

In this chapter we report on a theoretical model study of the optical conductivity of t_{2g} 2DEGs formed at perovskite oxide surfaces and interfaces. The detailed properties of these low-dimensional electron systems are difficult to predict theoretically because of the important role played in their properties by non-local and non-linear dielectric screening and by structural distortions and defects. This study is motivated by the potential value of spectral and sum rule information from optical characterization for verification and refinement of models of t_{2g} 2DEG properties.

We find that the in-plane optical conductivity is very strongly dominated by approximately independent Drude peak contributions coming from all bands, irrespective of their t_{2g}-orbital character and of the degree to which they are confined at the interface. Unlike the *dc* conductivity, the Drude weight, obtained by integrating the Drude peak over frequency, is independent of the unknown scattering times of the various bands. Our calculations show that measuring the Drude weight of t_{2g} 2DEGs will provide an estimate of the total 2D carrier density that is complementary to the one provided by Hall effect measurements. The in-plane conductivity will also have features associated with inter subband transitions, but these will be weak unless spin-orbit interactions hybridize t_{2g} electrons with different orbital character. In the model calculations we have performed the primary source of hybridization is atomic-like spin-orbit interactions which will normally have the strongest impact. Rashba[38, 124, 126, 128, 138] spin-orbit interactions, which we have not specifically

included, could provide a gate-tunable source of spin-orbit coupling which could enhance the value of in-plane current response measurements.

Unlike its in-plane counterpart, perpendicular-to-plane optical conductivity measurements should reveal a wealth of spectroscopic measurements. Their interpretation will however be complicated by depolarization shifts which mean that spectral features cannot be immediately identified with inter-subband transition energies. Based on our study we conclude that the influence of gates, particularly the influence of back gates on ellipsometry, might be helpful in assigning features to particular transitions in the t_{2g} 2DEG. When the t_{2g} carrier density is reduced by a back gate[36] it has the effect of increasing the electric field deep in the substrate, which has a particularly strong influence on the weakly-confined states which are otherwise present, sharply increasing the smallest subband splittings, decreasing the number of partially occupied subbands, and increasing spatial overlap between occupied and empty subbands. We can expect that broad tails in optical response will sharpen into discrete features which can be assigned on the basis of their spectral response to back gate voltages.

Chapter 8

Conclusion

This thesis has addressed the novel quantum confinement effects seen in d^0 perovskite heterostructures and their electrostatically gated surfaces. A general procedure has been suggested, based on confinement of bulk electronic conduction band states in an electric field screened by the lattice mediated non-linear and non-local dielectric response common in perovskites. Care has been taken in making contact with bulk experimental information. At high density, the perovskite 2DEG is composed of a few highly confined, xy and $\{yz, zx\}$ subbands due to the strong non-linear and non-local dielectric response with a bulk-like electronic tail composed of many t_{2g} subbands when the system is grounded. While the tail is expected to be responsible for the bulk like superconducting transition temperatures due to their close comparison with bulk values, the strongly confined subbands may be associated with magnetism measured experimentally in $LaAlO_3/SrTiO_3$ interfaces. The confined portion of the electronic density is sensitive to Rashba interactions induced by polar lattice distortions within the first few BO_2 layers which are intimately tied to the large dielectric response of the lattice.

Due to the versatility of the perovskite structure there are many exciting avenues to be explored to gain further understanding of these physical systems and

their potential applications. Some of the possible directions closely connected to this thesis are described below:

1. The perovskite 2DEG is particularly sensitive to back-gating. Back-gating increases the confinement and subband splitting in the tail of the electronic distribution and decreases the total 2D density simultaneously. This can be seen by generalizing the discussion of Section 5.2.3. In the presence of a back gate, the total 2D density is given by, $n_T = \epsilon_\infty \Delta E / 4\pi e$, where $\Delta E = E_0 - E_f$ is the difference in the electric field at the two boundaries. Superconducting transition temperatures in $LaAlO_3/SrTiO_3$ interfaces have been experimentally investigated with back-gates by Caviglia *et al.*, where the destruction of superconductivity along with a sharp increase in sheet resistance was associated with a quantum critical point[100] as opposed to a decrease in total density. A detailed experimental investigation in concurrence with a theoretical investigation of the electronic structure would be very informative in understanding this issue. Although technically very challenging, an out-of-plane optical conductivity study of the subband splitting due to back-gating would be most illuminating as well.

2. Because Rashba interactions in perovskites are dominated by changes in the lattice, it may be possible with advanced epitaxial growth techniques, to engineer Rashba interactions in artificial 2D systems. With this in mind, the tolerance factor defined in Eq. 1.1 can be used along with Z_B (the atomic number of the B atom) as a rule of thumb. Systems with a large tolerance factor are expected to have the most tunable soft polar mode. This suggests looking for materials with a large SO B atom and a large atomic radius A atom (as compared with the B atom). This also suggests

that ferroelectric materials may be good candidates for large Rashba interactions. With the large electric fields currently accessible with ionic liquid dielectrics[26, 29] this may be possible at surfaces of existing ferroelectric materials. Another consideration is the possibility of field induced cancelation of t_R in the Rashba Hamiltonian of Eq. 6.2 (and the discussion following it). Because γ_1 depends on the overlap of neighboring p and d wavefunction, as the B atom is changed, the size and sign of γ_1 may change. That being said, an *ab initio* study of γ_1 is well motivated to aid in the understanding of Rashba interactions in d^0 perovskites.

3. Recent experimental progress by Jeremy Levy's group shows that ~ 3.3 nm nanowires may be written with conducting AFM tips on $LaAlO_3/SrTiO_3$ heterostructures[149]. Provided this technique can be generalized, perovskites have several key advantages for supporting Majorana Fermions. Most important is the measured nanowire width suggested in Ref. [149]. This suggests that only a few subbands will be contributing due to the small confinement scale perpendicular to the wire direction. Secondly, Rashba interactions can be quite large and tunable (as discussed in Chapter 6). Finally, perovskite systems can be gated to be superconducting[29] - eliminating the need for proximity induced superconductivity[150].

Appendices

Appendix A

$\boldsymbol{k \cdot p}$ Hamiltonian for the tetragonal phase

The momentum dependent part of the effective hamiltonian h for a d^0 perovskite is given by Eq.(2.3). In this appendix we use group theory methods to express h in terms of a small number of phenomenological parameters[67].

The calculation of h involves the evaluation of matrix elements of the form $\langle\phi|\boldsymbol{k}\cdot\boldsymbol{p}|\psi_j\rangle$. Here ψ_j is a basis function of the t_{2g} manifold, $\boldsymbol{p}$ is the momentum operator, and ϕ is a state outside of the t_{2g} manifold. At the cubic to tetragonal phase transition the symmetry at the zone center reduces from O_h to D_{4h}. Correspondingly, at the phase transition the three ψ_j's change their transformation properties $\Gamma^+_{25} \rightarrow \Gamma^+_4 + \Gamma^+_5$. The three components of the momentum operator $\boldsymbol{p}$, that transform as a single irrep (Γ^-_{15}) in the cubic phase split: $p_x, p_y \in \Gamma^-_5$ whereas $p_z \in \Gamma^-_2$.

The values of the matrix elements vary smoothly across the structural transition. To emphasize the relation between the two symmetries we label the matrix elements in the tetragonal phase with a subscript that corresponds to the irrep of ϕ in the cubic phase and a superscript that corresponds to its irrep in the tetragonal phase . For example, B^5_{15} is associated with a basis function that evolved from Γ_{15} in the cubic phase to Γ_5 in the tetragonal one.

We first consider the Γ_4^+ band. The intermediate states are

$$\begin{aligned} \Gamma_5^- \otimes \Gamma_4^+ &= \Gamma_5^- \\ \Gamma_2^- \otimes \Gamma_4^+ &= \Gamma_3^- . \end{aligned} \tag{A.1}$$

Denoting

$$\begin{aligned} \langle \Gamma_{5x}^- | (p_x, p_y) | \Gamma_4^+ \rangle &= \begin{cases} B_{15}^5(0,1) \\ B_{25}^5(0,1) \end{cases} \\ \langle \Gamma_{5y}^- | (p_x, p_y) | \Gamma_4^+ \rangle &= \begin{cases} B_{15}^5(1,0) \\ -B_{25}^5(1,0) \end{cases} \\ \langle \Gamma_3^- | p_z | \Gamma_4^+ \rangle &= \begin{cases} B_2^3 \\ B_{12}^3 \end{cases} , \end{aligned} \tag{A.2}$$

we find that

$$h_{zz} = \mathcal{M}_B(k_x^2 + k_y^2) + \mathcal{L}_B k_z^2 \tag{A.3}$$

where the two real phenomenological parameters are given by

$$\mathcal{M}_B = \frac{1}{2m} + \frac{1}{m^2} \sum_{n' \in \Gamma_5^-} \frac{|B_{n'}^5|^2}{E^{\Gamma_4^+}(0) - E_{n'}^{\Gamma_5^-}(0)}, \tag{A.4}$$

and

$$\mathcal{L}_B = \frac{1}{2m} + \frac{1}{m^2} \sum_{n' \in \Gamma_3^-} \frac{|B_{n'}^3|^2}{E^{\Gamma_4^+}(0) - E_{n'}^{\Gamma_3^-}(0)}. \tag{A.5}$$

We now turn to the Γ_5^+ band. The intermediate states are

$$\begin{aligned} \Gamma_5^- \otimes \Gamma_5^+ &= \Gamma_1^- + \Gamma_2^- + \Gamma_3^- + \Gamma_4^- \\ \Gamma_2^- \otimes \Gamma_5^+ &= \Gamma_5^- . \end{aligned} \tag{A.6}$$

Following similar steps to those taken above we obtain expression (**??**). The k-dependent Hamiltonian h depends on six real parameters and a single complex parameter $\mathcal{N}_{BC}$. The $\boldsymbol{k} \cdot \boldsymbol{p}$ Hamiltonian in the cubic phase can easily be obtained from

its tetragonal counterpart by disregarding the subscripts of the phenomenological parameters; for example by associating with $\mathcal{L}_B$ and $\mathcal{L}_C$ a single parameter L.

Appendix B

Strain analysis for biaxial strain

A symmetry analysis of the average deformation of the lattice, to lowest order, for a cubic crystal lead to the standard textbook result[81] of the stress/strain relations, given in vector form, below by,

$$\tau_i = C_{im}\epsilon_m \tag{B.1}$$

$$\epsilon_m = S_{mi}\tau_i. \tag{B.2}$$

Where ϵ is the strain, τ is the stress, C is the stiffness matrix, and S is the compliance matrix. The stiffness and compliance are clearly inverse of each other and a poor choice of notation (S for stiffness and C for compliance seems more reasonable). The compliance matrix is given by,

$$S = \begin{pmatrix} S_{11} & S_{12} & S_{12} & 0 & 0 & 0 \\ S_{12} & S_{11} & S_{12} & 0 & 0 & 0 \\ S_{12} & S_{12} & S_{11} & 0 & 0 & 0 \\ 0 & 0 & 0 & S_{44} & S_{44} & S_{44} \\ 0 & 0 & 0 & S_{44} & S_{44} & S_{44} \\ 0 & 0 & 0 & S_{44} & S_{44} & S_{44} \end{pmatrix}. \tag{B.3}$$

For uniform biaxial strain within the $x-y$ plane - for example due to epitaxial mismatch - the stress, $\tau = (T, T, 0, 0, 0, 0)$. Solving Eq. B.2 leads to the following relations,

$$\epsilon_{xx} = \epsilon_{yy} = (S_{11} + S_{12})T \tag{B.4}$$

$$\epsilon_{zz} = 2S_{12}T. \tag{B.5}$$

This suggests the relation,

$$\epsilon_{zz} = \epsilon_{xx}\frac{2S_{12}}{S_{11}+S_{12}} = \epsilon_{xx}\frac{2\nu}{\nu-1} \tag{B.6}$$

where ν is again Poisson's ratio. Plugging this into the strain Hamiltonian for the t_{2g} bands (Eq. 3.2) and evaluating the induced splitting $\Delta_{biaxial}$, we find,

$$\Delta_{biaxial} = E_{yz,zx} - E_{xy} = -(l-m)\left(\frac{1+\nu}{1-\nu}\right)\epsilon. \tag{B.7}$$

In the above equation ϵ_{xx} has been relabeled as ϵ and we note that from the analysis of Chapter 3 $(l-m)$ is positive and the $\{yz, zx\}$ bands remain degenerate. Therefore, a uniform decrease in the lattice constant within the $x-y$ plane will pull the xy band down in energy, while a uniform increase in the in-plane lattice constant will push the xy band up in energy.

Using the deformation potentials of $SrTiO_3$ discussed in Chapter 3, the Poisson ratio at 120K, and a 1% change in the lattice constant as a reference we find that the

strain induced splitting is $\sim$ 65 meV. This energy scale is comparable to (or larger than) the confinement energy of the 2DEG in the low density regime (See Fig. 5.3). While this crude analysis ignores changes to the lattice mediated dielectric response in the presence of strain, it is clear that epitaxial strain can have a profound effect on the electronic structure of the 2DEG - in particular to the extended low density tail. This has been studied experimentally, before the conduction band deformation potentials were available [151] for $SrTiO_3$ on a series of substrates. The main result is that the 2DEG in LAO/STO is destroyed by compressive strain. This has been interpreted to be a result of changes in the dielectric response of the material - which will certainly be present - but the above analysis suggests that this can also be related to changes in the electronic structure due to strain - which has been underestimated using *ab initio* results[41].

Appendix C

Changes to perovskite bonding network in an electric field

Breaking the mirror symmetry of the 2DES allows additional covalent bonding terms - not present in the unperturbed cubic system. Those described in the main text are associated with the Rashba effect, but others new processes are allowed. These are summarized in the Table C.1. In the unpolarized system, the p_x orbital is not involved in the bonding along the x direction. For this reason γ_2 processes, which couples zx and p_x along the x direction, can only contribute to second order in E. The corresponding statement is also true for lattice displacements.

γ_3 increases or decreases the bonding strength with the apical oxygens. If both apical oxygen atoms are present, it can only contribute a term in the Hamiltonian that is quadratic in electric field. At the surface of a BO_2 terminated perovskite, there is a missing apical oxygen. Therefor, within the t_{2g} space and to first order in the electric field, the following term must be added to the Hamiltonian of the surface layer:

$$H_S = \begin{pmatrix} \Delta_S & 0 & 0 \\ 0 & \Delta_S & 0 \\ 0 & 0 & 0 \end{pmatrix}. \tag{C.1}$$

In the above equation, $\Delta_S = -E\gamma_3 t_{pd\pi}/\Delta_{pd}$ and may be positive or negative.

Tight-Binding Matrix Elements		
Lattice	$\langle xy, \vec{R}=0\vert\Delta U\vert\{x,y,z\}, \vec{R}=\pm\frac{a}{2}\hat{x}+n\frac{a}{2}\hat{z}\rangle$	$\{0,\pm t_{pd\pi},0\}$
Polarization	$\langle xy, \vec{R}=0\vert\Delta U\vert\{x,y,z\}, \vec{R}=\pm\frac{a}{2}\hat{y}+n\frac{a}{2}\hat{z}\rangle$	$\{\pm t_{pd\pi},0,0\}$
Effects	$\langle yz, \vec{R}=0\vert\Delta U\vert\{x,y,z\}, \vec{R}=\pm\frac{a}{2}\hat{x}+n\frac{a}{2}\hat{z}\rangle$	$\{0,nt_{pd\pi},0\}$
	$\langle yz, \vec{R}=0\vert\Delta U\vert\{x,y,z\}, \vec{R}=\pm\frac{a}{2}\hat{y}+n\frac{a}{2}\hat{z}\rangle$	$\{0,nt_{pd\pi},0\}$
Orbital	$\langle xy, \vec{R}=0\vert-ez\vert\{x,y,z\}, \vec{R}=\pm\frac{a}{2}\hat{x}\rangle$	$\{0,0,0\}$
Polarization	$\langle xy, \vec{R}=0\vert-ez\vert\{x,y,z\}, \vec{R}=\pm\frac{a}{2}\hat{y}\rangle$	$\{0,0,0\}$
Effects	$\langle yz, \vec{R}=0\vert-ez\vert\{x,y,z\}, \vec{R}=\pm\frac{a}{2}\hat{x}\rangle$	$\{0,\gamma_1,0\}$
	$\langle yz, \vec{R}=0\vert-ez\vert\{x,y,z\}, \vec{R}=\pm\frac{a}{2}\hat{y}\rangle$	$\{0,\gamma_2,0\}$
Apical Oxygen	$\langle xy, \vec{R}=0\vert-ez\vert\{x,y,z\}, \vec{R}=\pm\frac{a}{2}\hat{z}\rangle$	$\{0,0,0\}$
Atoms	$\langle yz, \vec{R}=0\vert-ez\vert\{x,y,z\}, \vec{R}=\pm\frac{a}{2}\hat{z}\rangle$	$\{0,\pm\gamma_3,0\}$

Table C.1: Tight-binding matrix elements for metal t_{2g} and oxygen p-orbitals. The matrix elements for the zx orbitals can be derived from the yz entries, by symmetry.

Because there is no periodicity in the z- direction, this term is independent of k. In addition, the lack of octahedral coordination at the surface can lead to significant t_{2g}/e_g hybridization.

In addition to the bonding changes to the cubic system mentioned above, if the structural distortions are more complicated (e.g. there is an in-plane twisting of the oxygen octahedra) some σ bonding between the oxygen p and metal t_{2g} orbitals will also be allowed. Provided the polar displacement is still present, these σ bonding channels can also contribute to the Rashba effect.

Bibliography

[1] Darrell G Schlom, Long-Qing Chen, Xiaoqing Pan, Andreas Schmehl, and Mark A Zurbuchen. A Thin Film Approach to Engineering Functionality into Oxides. *Journal of the American Ceramic Society*, 91(8):2429–2454, 2008.

[2] D G Schlom, J H Haeni, J Lettieri, and C D Theis. Oxide nano-engineering using MBE. *Materials Science and Engineering: B*, 87(3):282–291, 2001.

[3] A Ohtomo, D Muller, J Grazul, and H Hwang. Artificial charge-modulation in atomic-scale perovskite titanate superlattices. *Nature*, 2002.

[4] R McKee, F Walker, and M Chisholm. Crystalline Oxides on Silicon: The First Five Monolayers. *Physical Review Letters*, 81(14):3014–3017, 1998.

[5] C Rossel, B Mereu, C Marchiori, D Caimi, M Sousa, A Guiller, H Siegwart, R Germann, J P Locquet, J Fompeyrine, D J Webb, Ch Dieker, and Jin Won Seo. Field-effect transistors with $SrHfO_3$ as gate oxide. *Applied Physics Letters*, 89(5):053506, 2006.

[6] Pavlo Zubko, Stefano Gariglio, Marc Gabay, Philippe Ghosez, and Jean-Marc Triscone. Interface Physics in Complex Oxide Heterostructures. *Annual Review of Condensed Matter Physics*, 2(1):141–165, 2011.

[7] Victor Moritz Goldschmidt, Thomas F W Barth, G Lunde, and W Zachariasen. Geochemische Verteilungsgesetze der Elemente : 7. Die Gesetze der Krystallochemie, 1926.

[8] W Zhong and D Vanderbilt. Competing structural instabilities in cubic perovskites. *Physical Review Letters*, 1995.

[9] N A Benedek and C J Fennie. Why are there so few perovskite ferroelectrics? *J. Phys. Chem. C*, 2013. in print.

[10] I D Brown and D I Brown. *The Chemical Bond in Inorganic Chemistry: The Bond Valence Model*. Oxford University Press, 2006.

[11] C A Randall, R E Newnham, and L E Cross. History of the First Ferroelectric Oxide, BaTiO3. unpublished, 2004.

[12] SrTiO3 World of Science, June 2013. Retreived.

[13] SrTiO3 Google Patent, June 2013. Retreived.

[14] J Schooley, W Hosler, E Ambler, J Becker, Marvin Cohen, and C Koonce. Dependence of the Superconducting Transition Temperature on Carrier Concentration in Semiconducting $SrTiO_3$. *Physical Review Letters*, 14(9):305–307, 1965.

[15] J G Bednorz and K A Müller. Possible highT c superconductivity in the Ba La Cu O system. *Zeitschrift für Physik B Condensed Matter*, 1986.

[16] International Mineralogical Association. IMA List of Minerals, 2013.

[17] A Ohtomo and H Y Hwang. A high-mobility electron gas at the $LaAlO_3/SrTiO_3$ heterointerface. *Nature*, 427(6973):423–426, 2004.

[18] Pouya Moetakef, Tyler A Cain, Daniel G Ouellette, Jack Y Zhang, Dmitri O Klenov, Anderson Janotti, Chris G Van de Walle, Siddharth Rajan, S James Allen, and Susanne Stemmer. Electrostatic carrier doping of $GdTiO_3/SrTiO_3$ interfaces. *Applied Physics Letters*, 99(23):232116, 2011.

[19] Pouya Moetakef, Jack Y Zhang, Alexander Kozhanov, Bharat Jalan, Ram Seshadri, S James Allen, and Susanne Stemmer. Transport in ferromagnetic $GdTiO_3/SrTiO_3$ heterostructures. *Applied Physics Letters*, 98(11):112110, 2011.

[20] M Kim, C Bell, Y Kozuka, M Kurita, Y Hikita, and H Hwang. Fermi Surface and Superconductivity in Low-Density High-Mobility δ-Doped $SrTiO_3$. *Physical Review Letters*, 107(10), 2011.

[21] Y Kozuka, M Kim, H Ohta, Y Hikita, C Bell, and H Y Hwang. Enhancing the electron mobility via delta-doping in $SrTiO_3$. *Applied Physics Letters*, 97(22):222115, 2010.

[22] Y Kozuka, M Kim, C Bell, B Kim, Y Hikita, and H Hwang. Two-dimensional normal-state quantum oscillations in a superconducting heterostructure. *Nature*, 2009.

[23] Bharat Jalan, Susanne Stemmer, Shawn Mack, and S Allen. Two-dimensional electron gas in δ-doped $SrTiO_3$. *Physical Review B*, 82(8), 2010.

[24] A F Santander-Syro, O Copie, T Kondo, F Fortuna, S Pailhès, R Weht, X G Qiu, F Bertran, A Nicolaou, A Taleb-Ibrahimi, P Le Fèvre, G Herranz, M Bibes, N Reyren, Y Apertet, P Lecoeur, A Barthélémy, and M J Rozenberg. Two-dimensional electron gas with universal subbands at the surface of $SrTiO_3$. *Nature*, 469(7329):189–193, 2011.

[25] W Meevasana, PDC King, RH He, and SK Mo. Creation and control of a two-dimensional electron liquid at the bare $SrTiO_3$ surface. *Nature Materials*, 2011.

[26] K Ueno, S Nakamura, H Shimotani, and A Ohtomo. Electric-field-induced superconductivity in an insulator. *Nature Materials*, 2008.

[27] X Leng, S Snyder, and A Goldman. Phase Diagram of Electrostatically Doped $SrTiO_3$. *Physical Review Letters*, 2011.

[28] Menyoung Lee, J R Williams, Sipei Zhang, C Daniel Frisbie, and D Goldhaber-Gordon. Electrolyte Gate-Controlled Kondo Effect in $SrTiO_3$. *Physical Review Letters*, 107(25):256601, 2011.

[29] K Ueno, S Nakamura, and H Shimotani. Discovery of superconductivity in $KTaO_3$ by electrostatic carrier doping. *Nature*, 2011.

[30] N Reyren, S Thiel, A D Caviglia, L F Kourkoutis, G Hammerl, C Richter, C W Schneider, T Kopp, A S Ruetschi, D Jaccard, M Gabay, D A Muller, J M Triscone, and J Mannhart. Superconducting Interfaces Between Insulating Oxides. *Science*, 317(5842):1196–1199, 2007.

[31] Pouya Moetakef, James Williams, Daniel Ouellette, Adam Kajdos, David Goldhaber-Gordon, S Allen, and Susanne Stemmer. Carrier-Controlled Ferromagnetism in $SrTiO_3$. *Physical Review X*, 2(2):021014, 2012.

[32] Lu Li, C Richter, J Mannhart, and R C Ashoori. Coexistence of magnetic order and two-dimensional superconductivity at LaAlO3/SrTiO3 interfaces. *Nature Physics*, 7(10):762–766, 2011.

[33] Karen Michaeli, Andrew Potter, and Patrick Lee. Superconducting and Ferromagnetic Phases in $SrTiO_3/LaAlO_3$ Oxide Interface Structures: Possibility of Finite Momentum Pairing. *Physical Review Letters*, 108(11), 2012.

[34] Julie A Bert, Beena Kalisky, Christopher Bell, Minu Kim, Yasuyuki Hikita, Harold Y Hwang, and Kathryn A Moler. Direct imaging of the coexistence of ferromagnetism and superconductivity at the $LaAlO_3/SrTiO_3$ interface. *Nature Physics*, 7(10):767–771, 2011.

[35] D A Dikin, M Mehta, C W Bark, C M Folkman, C B Eom, and V Chandrasekhar. Coexistence of Superconductivity and Ferromagnetism in Two Dimensions. *Physical Review Letters*, 107(5):056802, 2011.

[36] Guru Khalsa and A H MacDonald. Theory of the $SrTiO_3$ surface state two-dimensional electron gas. *Physical Review B*, 86(12):125121, 2012.

[37] M Stengel. First-principles modeling of electrostatically doped perovskite systems. *Physical Review Letters*, 2011.

[38] Guru Khalsa, Byounghak Lee, and A H MacDonald. Theory of t_{2g} electron-gas Rashba interactions. *arXiv.org*, 2013.

[39] LF Mattheiss. Energy Bands for $KNiF_3$, $SrTiO_3$, $KMoO_3$, and $KTaO_3$. *Physical Review B*, 6(12):4718–4740, 1972.

[40] D van der Marel, J van Mechelen, and I Mazin. Common Fermi-liquid origin of T^2 resistivity and superconductivity in n-type $SrTiO_3$. *Physical Review B*, 84(20), 2011.

[41] A Janotti, D Steiauf, and C Van de Walle. Strain effects on the electronic structure of $SrTiO_3$: Toward high electron mobilities. *Physical Review B*, 84(20), 2011.

[42] A Leyendecker. Electronic energy bands in strontium titanate. *Phys. Rev*, 1964.

[43] H Frederikse, W Thurber, and W Hosler. Electronic Transport in Strontium Titanate. *Physical Review*, 134(2A):A442–A445, 1964.

[44] M Cardona. Optical properties and band structure of $SrTiO_3$ and $BaTiO_3$. *Phys. Rev*, 1965.

[45] H Frederikse, W Hosler, and W Thurber. Shubnikov—de Haas Effect in $SrTiO_3$. *Physical Review*, 1967.

[46] Z Sroubek. Electron Tunneling and Band Structure of $SrTiO_3$ and $KTaO_3$. *Physical Review B*, 2(8):3170–3175, 1970.

[47] B Gregory, J Arthur, and G Seidel. Measurements of the Fermi surface of $SrTiO_3$: Nb. *Physical Review B*, 19(2):1039–1048, 1979.

[48] H Uwe, R Yoshizaki, T Sakudo, and A Izumi. Conduction band structure of $SrTiO_3$. *Jpn. J. Appl. Phys*, 1985.

[49] H Uwe and T Sakudo. Interband Electronic Raman Scattering in $SrTiO_3$. *Jpn. J. Appl. Phys. Suppl*, 1985.

[50] R Bistritzer, G Khalsa, and A H MacDonald. Electronic structure of doped d^0 perovskite semiconductors. *Physical Review B*, 2011.

[51] Young Jun Chang, Aaron Bostwick, Yong Su Kim, Karsten Horn, and Eli Rotenberg. Structure and correlation effects in semiconducting $SrTiO_3$. *Physical Review B*, 81(23):235109, 2010.

[52] RC Neville, B Hoeneisen, and CA Mead. Permittivity of strontium titanate. *Journal of Applied Physics*, 43(5):2124–2131, 1972.

[53] RA Cowley. Lattice dynamics and phase transitions of strontium titanate. *Phys. Rev*, 134(4A):A981–A997, 1964.

[54] Y Yamada. Neutron scattering and nature of the soft optical phonon in $SrTiO_3$. *J Phys Soc Jap*, 1969.

[55] Young Jun Chang, Guru Khalsa, Luca Moreschini, Andrew L Walter, Aaron Bostwick, Karsten Horn, A H MacDonald, and Eli Rotenberg. Uniaxial strain

induced band splitting in semiconducting $SrTiO_3$. *Physical Review B*, 87(11):115212, 2013.

[56] S James Allen, Bharat Jalan, SungBin Lee, Daniel G Ouellette, Guru Khalsa, Jan Jaroszynski, Susanne Stemmer, and Allan H MacDonald. Conduction-band edge and Shubnikov–de Haas effect in low-electron-density SrTiO3. *Physical Review B*, 88:045114, 2013.

[57] Junwoo Son, Pouya Moetakef, Bharat , Oliver Bierwagen, Nicholas J Wright, Roman Engel-Herbert, and Susanne Stemmer. Epitaxial SrTiO3 films with electron mobilities exceeding 30,000cm2V1s1. *Nature Materials*, 9(6):482–484, 2010.

[58] H Nakamura and T Kimura. Electric field tuning of spin-orbit coupling in KTaO3 field-effect transistors. *Physical Review B*, 80(12):121308, 2009.

[59] A Brinkman, M Huijben, M Van Zalk, and J Huijben. Magnetic effects at the interface between non-magnetic oxides : Article : Nature Materials. *Nature Materials*, 2007.

[60] M Ben Shalom, C Tai, Y Lereah, M Sachs, E Levy, D Rakhmilevitch, A Palevski, and Y Dagan. Anisotropic magnetotransport at the $SrTiO_3/LaAlO_3$ interface. *Physical Review B*, 80(14), 2009.

[61] Snir Seri and Lior Klein. Antisymmetric magnetoresistance of the $SrTiO_3/LaAlO_3$ interface. *Physical Review B*, 80(18):180410, 2009.

[62] J Mannhart, DHA Blank, H Y Hwang, and A J Millis. Two-Dimensional Electron Gases at Oxide Interfaces. *MRS Bulletin*, 2008.

[63] J Heber. Materials science: Enter the oxides. *Nature*, 2009.

[64] LF Mattheiss. Effect of the 110° K Phase Transition on the $SrTiO_3$ Conduction Bands. *Physical Review B*, 6(12):4740–4753, 1972.

[65] T Neumann, G Borstel, C Scharfschwerdt, and M Neumann. Electronic structure of $KNbO_3$ and $KTaO_3$. *Physical Review B*, 46(17):10623–10628, 1992.

[66] M Q Cai, Z Yin, and M S Zhang. Optical properties of strontium titanate by ab initio calculation within density functional theory. *Chemical physics letters*, 2004.

[67] Ado Jorio M. S. Dresselhaus, Gene Dresselhaus. *Group Theory: Application to the Physics of Condensed Matter*. Springer, 2010.

[68] Peter Yu and Manuel Cardona. *Fundamentals of Semiconductors: Physics and Materials Properties*. Springer, 1996.

[69] L Cao, E Sozontov, and J Zegenhagen. Cubic to Tetragonal Phase Transition of $SrTiO_3$ under Epitaxial Stress: An X-Ray Backscattering Study. *physica status solidi (a)*, 2000.

[70] Andrea Damascelli and Zhi-Xun Shen. Angle-resolved photoemission studies of the cuprate superconductors. *Reviews of Modern Physics*, 75(2):473–541, 2003.

[71] J B Pendry. Theory of photoemission. *Surface Science*, 57(2):679–705, 1976.

[72] W Meevasana, X Zhou, and B Moritz. Strong energy–momentum dispersion of phonon-dressed carriers in the lightly doped band insulator SrTiO3. *New Journal of . . .*, 2010.

[73] N. Mermin N. W. Ashcroft. *Solid State Physics*. Thomson Learning Inc., 1976.

[74] M. P. Marder. *Condensed Matter Physics*. John Wiley & Sons, Inc., 2000.

[75] J. Kubler. *Theory of Itinerant Electron Magnetism*. Oxford University Press Inc., 2000.

[76] J. Singleton. *Band theory and electronic properties of solids*. Oxford University Press Inc., 2001.

[77] R G Chambers. Magnetic breakdown in real metals. *Proceedings of the Physical Society*, 88(3):701–715, 2002.

[78] Bharat Jalan, S James Allen, Glenn E Beltz, Pouya Moetakef, and Susanne Stemmer. Enhancing the electron mobility of $SrTiO_3$ with strain. *Applied Physics Letters*, 98(13):132102–132102–3, 2011.

[79] Daiichiro Sekiba, Kan Nakatsuji, Yoshihide Yoshimoto, and Fumio Komori. Direct Observation of Strain-Induced Change in Surface Electronic Structure. *Physical Review Letters*, 94(1):016808, 2005.

[80] Georg Neuhold and Karsten Horn. Depopulation of the Ag(111) Surface State Assigned to Strain in Epitaxial Films. *Physical Review Letters*, 78(7):1327–1330, 1997.

[81] S. E. Thompson Y. K. Sun and T. Nishida. *Strain Effect in Semicondutors*. Springer, London, 2010.

[82] Min Chu, Yongke Sun, Umamaheswari Aghoram, and Scott E Thompson. Strain: A Solution for Higher Carrier Mobility in Nanoscale MOSFETs. *Annual Review of Materials Research*, 39(1):203–229, 2009.

[83] M Abrecht, D Ariosa, D Cloetta, S Mitrovic, M Onellion, X Xi, G Margaritondo, and D Pavuna. Strain and High Temperature Superconductivity: Unexpected Results from Direct Electronic Structure Measurements in Thin Films. *Physical Review Letters*, 91(5):057002, 2003.

[84] H Wadati, A Maniwa, A Chikamatsu, I Ohkubo, H Kumigashira, M Oshima, A Fujimori, M Lippmaa, M Kawasaki, and H Koinuma. In Situ Photoemission Study of Pr1-xCaxMnO_3 Epitaxial Thin Films with Suppressed Charge Fluctuations. *Physical Review Letters*, 100(2):026402, 2008.

[85] Darrell G Schlom, Long-Qing Chen, Chang-Beom Eom, Karin M Rabe, Stephen K Streiffer, and Jean-Marc Triscone. Strain Tuning of Ferroelectric Thin Films*. *Annual Review of Materials Research*, 37(1):589–626, 2007.

[86] T Bak, J Nowotny, M Rekas, and C C Sorrell. Photo-electrochemical hydrogen

generation from water using solar energy. Materials-related aspects. *International Journal of Hydrogen Energy*, 27(10):991–1022, 2002.

[87] Hiromichi Ohta, SungWng Kim, Yoriko Mune, Teruyasu Mizoguchi, Kenji Nomura, Shingo Ohta, Takashi Nomura, Yuki Nakanishi, Yuichi Ikuhara, Masahiro Hirano, Hideo Hosono, and Kunihito Koumoto. Giant thermoelectric Seebeck coefficient of a two-dimensional electron gas in $SrTiO_3$. *Nature Materials*, 6(2):129–134, 2007.

[88] J Mannhart and D G Schlom. Oxide Interfaces–An Opportunity for Electronics. *Science*, 327(5973):1607–1611, 2010.

[89] Ariando, X Wang, G Baskaran, Z Q Liu, J Huijben, J B Yi, A Annadi, A Roy Barman, A Rusydi, S Dhar, Y P Feng, J Ding, H Hilgenkamp, and T Venkatesan. Electronic phase separation at the $LaAlO_3/SrTiO_3$ interface. *Nature Communications*, 2:188–, 2011.

[90] M Salluzzo, J Cezar, N Brookes, V Bisogni, and G De. Orbital Reconstruction and the Two-Dimensional Electron Gas at the $LaAlO_3/SrTiO_3$ Interface. *Physical Review Letters*, 2009.

[91] R Berger and C Fennie. Band Gap and Edge Engineering via Ferroic Distortion and Anisotropic Strain: The Case of $SrTiO_3$. *Physical Review Letters*, 2011.

[92] C W Bark, D A Felker, Y Wang, Y Zhang, H W Jang, C M Folkman, J W Park, S H Baek, H Zhou, D D Fong, X Q Pan, E Y Tsymbal, M S Rzchowski, and C B Eom. Tailoring a two-dimensional electron gas at the $LaAlO_3/SrTiO_3$

(001) interface by epitaxial strain. *Proceedings of the National Academy of Sciences*, 108(12):4720–4724, 2011.

[93] L. Bir and G. E. Pikus. *Symmetry and Strain Effects in Semiconductors*. Wiley, New York, 1974.

[94] G Rupprecht. Elastic constants of strontium titanate. *Physical Review*, 1963.

[95] G Binnig, A Baratoff, H Hoenig, and J Bednorz. Two-Band Superconductivity in Nb-Doped $SrTiO_3$. *Physical Review Letters*, 45(16):1352–1355, 1980.

[96] P Zubko, G Catalan, A Buckley, P Welche, and J Scott. Strain-Gradient-Induced Polarization in $SrTiO_3$ Single Crystals. *Physical Review Letters*, 99(16):167601, 2007.

[97] Young Chang, Choong Kim, S H Phark, Y Kim, J Yu, and T Noh. Fundamental Thickness Limit of Itinerant Ferromagnetic $SrRuO_3$ Thin Films. *Physical Review Letters*, 103(5), 2009.

[98] A Tebano, A Orsini, P G Medaglia, D Di Castro, G Balestrino, B Freelon, A Bostwick, Young Jun Chang, G Gaines, E Rotenberg, and N L Saini. Preferential occupation of interface bands in $La_{2/3}Sr_{1/3}MnO_3$ films as seen via angle-resolved photoemission. *Physical Review B*, 82(21):214407, 2010.

[99] M Kawasaki, B Keimer, N Nagaosa, and Y Tokura. Emergent phenomena at oxide interfaces : Nature Materials : Nature Publishing Group. *Nature materials*, 2012.

[100] A D Caviglia, S Gariglio, N Reyren, D Jaccard, T Schneider, M Gabay, S Thiel, G Hammerl, J Mannhart, and J M Triscone. Electric field control of the $LaAlO_3/SrTiO_3$ interface ground state. *Nature*, 456(7222):624–627, 2008.

[101] J Luttinger. Quantum theory of cyclotron resonance in semiconductors: General theory. *Physical Review*, 1956.

[102] B Jalan, R Engel-Herbert, and N J Wright. Growth of high-quality $SrTiO_3$ films using a hybrid molecular beam epitaxy approach. *Journal of Vacuum Science & Technology A: Vacuum, Surfaces, and Films*, 2009.

[103] L. M. Roth and P. N. Argyres. *Physics of III-V Compounds*. Academic Press, New York, 1966.

[104] Richard Prange and Leo Kadanoff. Transport Theory for Electron-Phonon Interactions in Metals. *Physical Review*, 134(3A):A566–A580, 1964.

[105] J van Mechelen, D van der Marel, C Grimaldi, A Kuzmenko, N Armitage, N Reyren, H Hagemann, and I Mazin. Electron-Phonon Interaction and Charge Carrier Mass Enhancement in $SrTiO_3$. *Physical Review Letters*, 100(22), 2008.

[106] S Thiel, S Hammerl, A Schmehl, C W Schneider, and J Mannhart. Tunable Quasi-Two-Dimensional Electron Gases in Oxide Heterostructures. *Science*, 313(5795):1942–1945, 2006.

[107] H Jeffrey Gardner, Ashwani Kumar, Liuqi Yu, Peng Xiong, Maitri P Warusawithana, Luyang Wang, Oskar Vafek, and Darrell G Schlom. Enhancement of

superconductivity by a parallel magnetic field in two-dimensional superconductors. *Nature Physics*, 7(11):895–900, 2011.

[108] P Willmott, S Pauli, R Herger, C Schlepütz, D Martoccia, B Patterson, B Delley, R Clarke, D Kumah, C Cionca, and Y Yacoby. Structural Basis for the Conducting Interface between $LaAlO_3$ and $SrTiO_3$. *Physical Review Letters*, 99(15), 2007.

[109] M Huijben, G Koster, H J A Molegraaf, M K Kruize, S Wenderich, J E Kleibeuker, A McCollam, V K Guduru, A Brinkman, H Hilgenkamp, U Zeitler, J C Maan, D H A Blank, and G Rijnders. High mobility interface electron gas by defect scavenging in a modulation doped oxide heterostructure. *arXiv.org*, 2010.

[110] Pouya Moetakef, Daniel G Ouellette, James R Williams, S James Allen, Leon Balents, David Goldhaber-Gordon, and Susanne Stemmer. Quantum oscillations from a two-dimensional electron gas at a Mott/band insulator interface. *Applied Physics Letters*, 101(15):151604, 2012.

[111] L Li, C Richter, S Paetel, T Kopp, J Mannhart, and R C Ashoori. Very Large Capacitance Enhancement in a Two-Dimensional Electron System. *Science*, 332(6031):825–828, 2011.

[112] Zoran Popović, Sashi Satpathy, and Richard Martin. Origin of the Two-Dimensional Electron Gas Carrier Density at the $LaAlO_3$ on $SrTiO_3$ Interface. *Physical Review Letters*, 101(25), 2008.

[113] S Okamoto and A Millis. Theory of Mott insulator–band insulator heterostructures. *Physical Review B*, 2004.

[114] Satoshi Okamoto and Andrew Millis. Spatial inhomogeneity and strong correlation physics: A dynamical mean-field study of a model Mott-insulator–band-insulator heterostructure. *Physical Review B*, 70(24), 2004.

[115] Z Popovic and S Satpathy. Wedge-shaped potential and Airy-function electron localization in oxide superlattices. *Physical Review Letters*, 2005.

[116] Won-joon Son, Eunae Cho, Bora Lee, Jaichan Lee, and Seungwu Han. Density and spatial distribution of charge carriers in the intrinsic n-type $LaAlO_3$-$SrTiO_3$ interface. *Physical Review B*, 79(24), 2009.

[117] Rossitza Pentcheva and Warren Pickett. Avoiding the Polarization Catastrophe in $LaAlO_3$ Overlayers on $SrTiO_3$(001) through Polar Distortion. *Physical Review Letters*, 102(10), 2009.

[118] Pietro Delugas, Alessio Filippetti, Vincenzo Fiorentini, Daniel Bilc, Denis Fontaine, and Philippe Ghosez. Spontaneous 2-Dimensional Carrier Confinement at the n-Type $SrTiO_3$/$LaAlO_3$ Interface. *Physical Review Letters*, 106(16), 2011.

[119] P King, R He, T. Eknapakul, P. Buaphet, S-K Mo, Y. Kaneko, S. Harashima, Y Hikita, M Bahramy, C Bell, Z. Hussain, Y Tokura, Z X Shen, H Hwang, F Baumberger, and W Meevasana. Subband Structure of a Two-Dimensional Electron Gas Formed at the Polar Surface of the Strong Spin-Orbit Perovskite $KTaO_3$. *Physical Review Letters*, 108(11):117602, 2012.

[120] A Demkov. Charge origin and localization at the n-type $SrTiO_3/LaAlO_3$ interface. *Physical Review B*, 2008.

[121] Naoyuki Nakagawa, Harold Y Hwang, and David A Muller. Why some interfaces cannot be sharp. *Nature Materials*, 5(3):204–209, 2006.

[122] F. Stern. Self-consistent results for n-type Si inversion layers. *Physical Review B*, 5(12):4891, 1972.

[123] CS Koonce, ML Cohen, JF Schooley, and WR Hosler. Superconducting Transition Temperatures of Semiconducting $SrTiO_3$. *Physical Review*, 1967.

[124] A D Caviglia, M Gabay, S Gariglio, and N Reyren. Tunable Rashba Spin-Orbit Interaction at Oxide Interfaces. *Physical Review*, 2010.

[125] Chenglong Jia and Jamal Berakdar. Magnetotransport and spin dynamics in an electron gas formed at oxide interfaces. *Physical Review B*, 83(4):045309, 2011.

[126] A Fête, S Gariglio, A D Caviglia, J M Triscone, and M Gabay. Rashba induced magnetoconductance oscillations in the $LaAlO_3$-$SrTiO_3$ heterostructure. *Physical Review B*, 86(20):201105, 2012.

[127] Arjun Joshua, Jonathan Ruhman, Sharon Pecker, Ehud Altman, and Shahal Ilani. Gate-tunable polarized phase of two-dimensional electrons at the $LaAlO_3/SrTiO_3$ interface. *PNAS*, 110(24):9633–9638, 2013.

[128] H Nakamura, T Koga, and T Kimura. Experimental Evidence of Cubic Rashba Effect in an Inversion-Symmetric Oxide. *Physical Review Letters*, 108(20):206601, 2012.

[129] E Flekser, M Ben Shalom, M Kim, C Bell, Y Hikita, H Hwang, and Y Dagan. Magnetotransport effects in polar versus non-polar $SrTiO_3$ based heterostructures. *Physical Review B*, 86(12):121104, 2012.

[130] H Nakamura and T Kimura. Electric field tuning of spin-orbit coupling in $KTaO_3$ field-effect transistors. *Physical Review B*, 80(12):121308, 2009.

[131] C Kittel. *Quantum Theory of Solids*. Wiley, New York, 1963.

[132] G Dresselhaus. Spin-orbit coupling effects in zinc blende structures. *Physical Review*, 100(2):580–586, 1955.

[133] Y A Bychkov and E I Rashba. Properties of a 2D electron gas with lifted spectral degeneracy. *JETP lett*, 1984.

[134] R Winkler. *Spin-Orbit Coupling Effects in Two-Dimensional Electron and Hole Systems*. Springer, Berlin, 2003.

[135] J B Goodenough. *Localized to Itinerant Electronic Transition in Perovskite Oxides*. Springer, Berlin, 1996.

[136] J C Slater and G F Koster. Simplified LCAO Method for the Periodic Potential Problem. *Physical Review*, 94(6):1498–1524, 1954.

[137] A Joshua, S Pecker, J Ruhman, and E Altman. A universal critical density underlying the physics of electrons at the $LaAlO_3/SrTiO_3$ interface. *Nature*, 2012.

[138] Zhicheng Zhong, Anna Toth, and Karsten Held. Theory of spin-orbit coupling at $LaAlO_3/SrTiO_3$ interfaces and $SrTiO_3$ surfaces. *arXiv.org*, 2012.

[139] G Kresse and J Furthmüller. Efficiency of ab-initio total energy calculations for metals and semiconductors using a plane-wave basis set. *Computational Materials Science*, 1996.

[140] John P Perdew, Kieron Burke, and Matthias Ernzerhof. Generalized Gradient Approximation Made Simple. *Physical Review Letters*, 77(18):3865–3868, 1996.

[141] Tsuneya Ando. Electronic properties of two-dimensional systems. *Reviews of Modern Physics*, 54(2):437–672, April 1982.

[142] G Harbeke. Intersubband Spectroscopy of Semiconductor Quantum Wells - Abstract - Physica Scripta. *Physica Scripta*, 1989.

[143] L C West and S J Eglash. First observation of an extremely largedipole infrared transition within the conduction band of a GaAs quantum well. *Applied Physics Letters*, 1985.

[144] Se Young Park and Andrew J Millis. Charge density distribution and optical response of the $LaAlO_3/SrTiO_3$ interface. *Physical Review B*, 87(20):205145, May 2013.

[145] Ryogo Kubo. Statistical-Mechanical Theory of Irreversible Processes. I. General Theory and Simple Applications to Magnetic and Conduction Problems. *Journal of the Physical Society of Japan*, 12(6):570–586, June 1957.

[146] G Mahan. *Many particle physics*. Springer, 2010.

[147] Z Q Liu, C J Li, W M Lü, X H Huang, Z Huang, S W Zeng, X P Qiu, L S Huang, A Annadi, J S Chen, J M D Coey, T Venkatesan, and Ariando. Origin of the two-dimensional electron gas at $LaAlO_3/SrTiO_3$ interfaces: The role of oxygen vacancies and electronic reconstruction. *arXiv.org*, May 2013.

[148] S J Allen, Jr, D C Tsui, and B Vinter. On the absorption of infrared radiation by electrons in semiconductor inversion layers. *Solid State Communications*, 1976.

[149] C Cen, S Thiel, G Hammerl, C W Schneider, K E Andersen, C S Hellberg, J Mannhart, and J Levy. Nanoscale control of an interfacial metal–insulator transition at room temperature. *Nature Materials*, 7(4):298–302, 2008.

[150] Jason Alicea. New directions in the pursuit of Majorana fermions in solid state systems. *Rep. Prog. Phys.*, 75:076501, 2012.

[151] C W Bark, D A Felker, Y Wang, Y Zhang, H W Jang, C M Folkman, J W Park, S H Baek, H Zhou, D D Fong, X Q Pan, E Y Tsymbal, M S Rzchowski, and C B Eom. Tailoring a two-dimensional electron gas at the $LaAlO_3/SrTiO_3$ (001) interface by epitaxial strain. *Proceedings of the National Academy of Sciences*, 108(12):4720–4724, 2011.

Vita

Guru was born in Loma Linda, California on February 12th, 1977, the son of Sant Subagh Singh Khalsa and Sant Khalsa. He received a Bachelor of Science in Mathematics from the University of New Mexico in May of 2005. He worked for one year studying Physics at the University of New Mexico and in August of 2006 he entered the Graduate School of the University of Texas.

Permanent address: Department of Physics
The University of Texas at Austin
1 University Station C1600
Austin, Texas 78712

This dissertation was typeset with LaTeX[†] by the author.

[†]LaTeX is a document preparation system developed by Leslie Lamport as a special version of Donald Knuth's TeX Program.